Characterizing the Influence of Amino Acids on the Oxidation/Reduction Properties of Transition Metals

by

Dong Wang

A Dissertation Presented in Partial Fulfillment
of the Requirements for the Degree
Doctor of Philosophy

Approved May 2014 by the
Graduate Supervisory Committee:

James Allen, Chair
Giovanna Ghirlanda
Kevin Redding

ARIZONA STATE UNIVERSITY

August 2014

ABSTRACT

The utilization of solar energy requires an efficient means of its storage as fuel. In bio-inspired artificial photosynthesis, light energy can be used to drive water oxidation, but catalysts that produce molecular oxygen from water are required. This dissertation demonstrates a novel complex utilizing earth-abundant Ni in combination with glycine as an efficient catalyst with a modest overpotential of 0.475 ± 0.005 V for a current density of 1 mA/cm^2 at pH 11. The production of molecular oxygen at a high potential was verified by measurement of the change in oxygen concentration, yielding a Faradaic efficiency of $60 \pm 5\%$. This Ni species can achieve a current density of 4 mA/cm^2 that persists for at least 10 hours. Based upon the observed pH dependence of the current amplitude and oxidation/reduction peaks, the catalysis is an electron-proton coupled process. In addition, to investigate the binding of divalent metals to proteins, four peptides were designed and synthesized with carboxylate and histidine ligands. The binding of the metals was characterized by monitoring the metal-induced changes in circular dichroism spectra. Cyclic voltammetry demonstrated that bound copper underwent a Cu(I)/Cu(II) oxidation/reduction change at a potential of approximately 0.32 V in a quasi-reversible process. The relative binding affinity of Mn(II), Fe(II), Co(II), Ni(II) and Cu(II) to the peptides is correlated with the stability constants of the Irving-Williams series for divalent metal ions. A potential application of these complexes of transition metals with amino acids or peptides is in the development of artificial photosynthetic cells.

DEDICATION

To my mom, dad and grandparents.

ACKNOWLEDGMENTS

I would like to thank Dr. James P. Allen for his mentoring during my graduate career. Jim demonstrated to me how to be persistent and optimistic in research and life, and he granted me more patience than I probably deserved. I owe gratitude to Dr. JoAnn Williams for her support since I joined the graduate program. I am also in debt to other Allen lab members, in particular, Dr. Tien L Olson, Dr. Chenda Seng, Dr. Aaron Tufts and Dr. Tracy Niday. Thank you for your help, assistance and guidance.

I have been lucky to work in collaborate with Dr. Giovanna Ghirlanda and her group members especially Dr. Sandip Shinde, Dr. Mathieu Walther and Dayn Sommer. They taught me peptide synthesis and purification. I also owe thanks to Dr. Marco Flores for his insight on unpaired electrons. Thanks to Chad Simmons from the group of Dr. Hao Yan for assistance with the thiol-labeled peptides.

I am thankful to Dr. Zhenquan Liu from the LeRoy Eyring Center for Solid State Science at Arizona State University for SEM-EDX measurements, and I am grateful to Paul Lee from the Laboratory for Electron Spectroscopy and Surface Analysis at University of Arizona for XPS measurements.

Thank you to the Biological Design Graduate Program for bringing me to Arizona State University and providing me a graduate research fellowship during my first year.

TABLE OF CONTENTS

Page

CHAPTER Page

LIST OF TABLES

LIST OF FIGURES

Figure Page

CHAPTER 1

INTRODUCTION

1.1 Transition metals

1.1.1 Introduction

Transition metals are essential components for many biological processes, such as respiration and photosynthesis. Transition metals also serve as catalysts in industry. For example, iron-based catalysts are used in large-scale ammonia production (Smil 2004). Therefore, transition metals are intriguing subjects for research for both expanding our knowledge and contributing to industrial practice.

By definition, transition metals are elements with unfilled *d* or *f* orbitals for the elemental ground states (Sharpe 1992). For example, the electronic configuration of Ni at the ground state is [Ar] $3d^8 4s^2$, in which the *d* orbitals are unfilled, as the 3*d* orbitals could hold as many as ten electrons. This definition could be relaxed to include common oxidation states where an element has unfilled *d* or *f* orbitals. For Cu, the elemental state has the ground electronic configuration of [Ar] $3d^{10} 4s^1$, where the 3*d* orbitals are filled, and thus copper formally does not belong with the transition metals. However, copper is considered as a transition metal because one of its significant oxidation states is Cu^{2+}, which has an electronic configuration of [Ar] $3d^9$ with the 3*d* orbitals unfilled. For Zn, its 3*d* orbitals are filled in either its elemental form ([Ar] $3d^{10} 4s^2$) or in its common oxidation state Zn^{2+} ([Ar] $3d^{10}$). For this reason Zn is not a member of the transition metals.

Transition metals are distributed in more than four rows in the periodic table. Elements from scandium to copper make up the first-row transition metals. Out of the nine first-row transition metals, vanadium, chromium, manganese, iron, cobalt, nickel

and copper are essential elements for a wide range of living organisms (Bertini 2007). Other than first-row transition metals, only a handful of transition metals such as molybdenum and tungsten have been shown to have biological function (Kletzin and Adams 1996). The first-row transition metals are the most important subjects in transition metal research.

1.1.2 Redox chemistry of first-row transition metals

First-row transition metals have unfilled *d* orbitals, and often have multiple stable oxidation states, which means they can donate or accept electrons. This property enables the transition metals to catalyze redox reactions or serve as electron transfer agents. In a redox reaction, an oxidant (A_{ox}) gets reduced into A_{red} by a reductant (B_{red}), as B_{red} gets oxidized to $B_{ox,}$ according to:

$$A_{ox} + B_{red} \rightarrow A_{red} + B_{ox} \qquad 1.1.a$$

This redox reaction can be viewed as having two half reactions as shown below:

$$A_{ox} + n\ e^- \rightarrow A_{red} \qquad 1.1.b$$

$$B_{red} - n\ e^- \rightarrow B_{ox} \qquad 1.1.c$$

where n is the number of electrons transferred. If this redox reaction happens in an electrochemical cell, where each of the half reactions takes place on an electrode, there will be a potential (E) generated by this cell. At equilibrium, E is governed by the Nernst equation as:

$$E = E^0 + \frac{RT}{nF} \ln \frac{[A_{ox}][B_{red}]}{[A_{red}][B_{ox}]} \qquad 1.1.d$$

where R is the ideal gas constant, T is the temperature in K and F is the Faraday constant. If a redox pair is used as one electrode, and a standard hydrogen electrode is used as the other electrode (hydrogen partial pressure at 1 MPa and pH = 0), then at equilibrium, the

potential of this cell is defined as the standard electrode potential (E^0) or mid-point potential ($E_{1/2}$) of this redox pair. According to this definition, the standard electrode potential for a standard hydrogen electrode is assigned 0 at any temperature. At any condition other than standard conditions, applying the Nernst equation to the half reaction 1.1.b, the potential of this redox pair *versus* standard hydrogen electrode is:

$$E_{A_{ox}/A_{red}} = E^0_{A_{ox}/A_{red}} + \frac{RT}{nF} \ln \frac{[A_{ox}]}{[A_{red}]} \qquad 1.1.e$$

The electronic configurations for first-row transition metals and their common oxidation states are provided in Table 1.1.a. Taking copper as an example, besides its elemental state, copper has four common oxidation states, Cu(I), Cu(II), Cu(III) and Cu(IV), among which Cu(I) and Cu(II) are most stable. Since copper is redox active, it is found in the active site of many redox catalysts and used for electron transfer reactions. Many of the properties associated with these two oxidation states will be further discussed in Chapter 1.1.3. In certain cases such as water oxidation, copper has also been suggested to undergo Cu(III) and Cu(IV) during catalysis (Zhang *et al.* 2013).

Table 1.1.a Oxidation states of first-row transition metals (most stable in bold) and their electronic configurations.

Sc	0	$3d^14s^2$					**3**	[Ar]								
Ti	0	$3d^24s^2$			2		**3**	$3d^1$	**4**	[Ar]						
V	0	$3d^34s^2$			2		**3**	$3d^2$	**4**	$3d^1$	**5**	[Ar]				
Cr	0	$3d^54s^1$			**2**	$3d^4$	**3**	$3d^3$	4		5		**6**	[Ar]		
Mn	0	$3d^54s^2$	1		**2**	$3d^5$	**3**	$3d^4$	4		5		6		**7**	[Ar]
Fe	0	$3d^64s^2$	1		**2**	$3d^6$	**3**	$3d^5$	4				6			
Co	0	$3d^74s^2$	1		**2**	$3d^7$	**3**	$3d^6$	4							
Ni	0	$3d^84s^2$	1		**2**	$3d^8$	3		4							
Cu	0	$3d^{10}4s^1$	**1**	$3d^{10}$	**2**	$3d^9$	3		4							

[Ar] = $1s^22s^22p^63s^23p^6$
Table information adapted from (Sharpe 1992, Cotton *et al.* 1995).

1.1.3 Protein environments fine tune the redox properties of transition metals

Redox active proteins typically contain transition metals in their active sites, and these proteins can serve as electron transfer agents or redox catalysts. Proteins containing metal ions are called metalloproteins. The blue copper proteins are a group of metalloproteins utilizing a single copper ion in the active site coordinated by two nitrogen ligands and one sulfur ligand in a planar arrangement, with or without axial ligands (Holm *et al.* 1996). The blue copper proteins typically serve as electron transfer carriers, for example plastocyanin in photosynthesis.

A number of plastocyanin proteins from different species have been crystallized and the structures have been solved, all of which display almost identical active-site structures (Gray *et al.* 2000). From a structural point of view, plastocyanin presents an overall cylinder shape surrounded by β-strands (Figure 1.1.a.I). In the active site, copper is coordinated by two nitrogen ligands from

histidines and one sulfur ligand from cysteine, with an axial ligand from the sulfur of a methionine (Figure 1.1.a.II).

In plastocyanin, the oxidation state of copper was found to cycle between Cu(II) and Cu(I) while undergoing electron transfer. Under standard conditions, the oxidation/reduction potential of aqueous copper, $E^0_{Cu(II)/Cu(I)}$, is +153 mV. The oxidation/reduction potential of plastocyanin was reported to be *ca.* +350 mV (Holm RH *et al*. 1996). This is about 200 mV higher than that of aqueous copper and is presumably due to the protein environment of two nitrogen and two sulfur ligands compared to all water ligands.

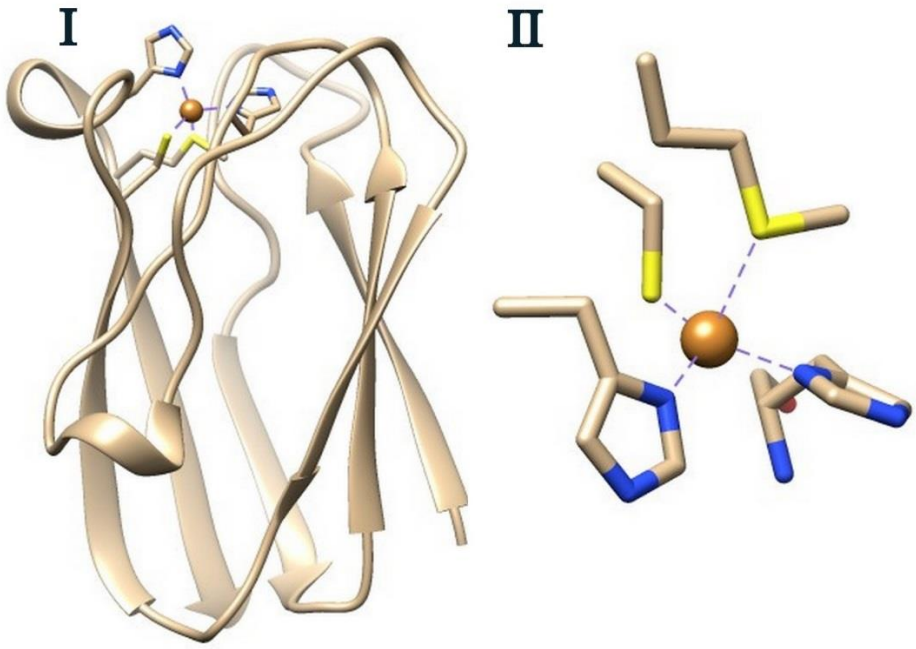

Figure 1.1.a Structure of plastocyanin from cyanobacterium *Synechococcus* sp. PCC 7942. I) Overall structure. II) Active site configuration. Carbon (grey), nitrogen (blue), oxygen (red), sulfur (yellow), copper (dark yellow ball). Purple dashed lines denote the metal-ligand bonds. PDB: 1BXU, (Inoue et al. 1999). The diagrams were generated using Chimera (Pettersen et al. 2004).

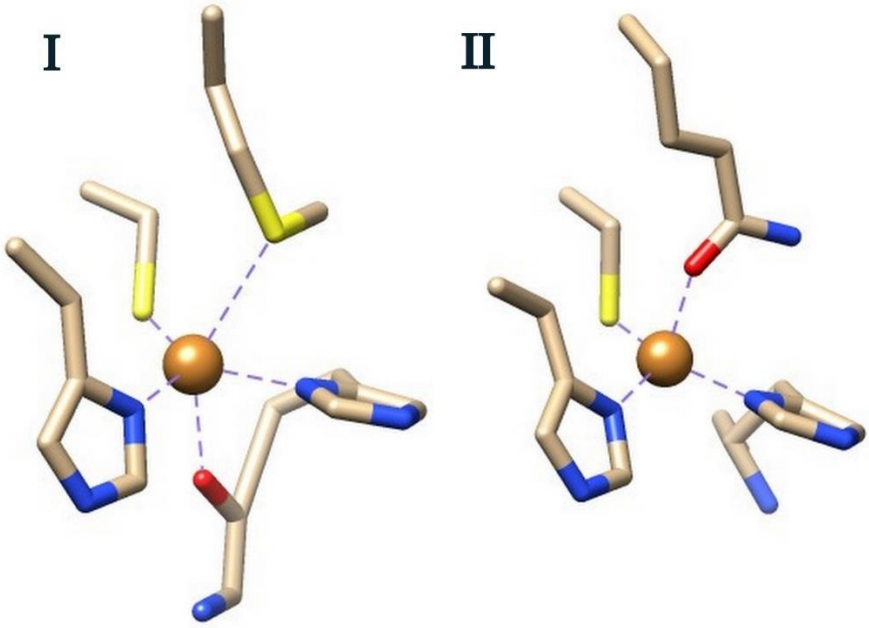

Figure 1.1.b Active site structures of azurin and stellacyanin. I) Azurin, PDB: 1AZU, (Adman and Jensen 1981). II) Stellacyanin, PDB: 1JER, (Hart *et al.* 1996). Carbon (grey), nitrogen (blue), oxygen (red), sulfur (yellow), copper (dark yellow ball). Purple dashed lines denote the metal-ligand bonds. The diagrams were generated using Chimera (Pettersen *et al.* 2004).

Protein environments can change the redox properties of the active-site metal by changing the coordinating ligands. For example, azurin is another member of the blue copper proteins and has a similar active-site configuration to that of plastocyanin except that copper in azurin has a fifth ligand that is a backbone carbonyl oxygen from a Gly residue (Figure 1.1.b.I). The electron-donating effect of this carbonyl oxygen increases the electron density around the copper, making it easier to be oxidized, and therefore reduces its reduction potential. The reduction potential of azurin was generally reported to be *ca.* +250 mV at near neutral pH (Holm *et al.* 1996), approximately 100 mV lower than that of plastocyanin. Stellacyanin, another member of the blue copper family, displays an even lower mid-point potential of *ca.* + 150 mV. Structural analysis

demonstrated that in the active site of stellacyanin, copper has the identical planar ligands of plastocyanin but the axial Met-sulfur ligand in plastocyanin is replaced by a carbonyl oxygen from Gln in stellacyanin (Figure 1.1.b.II). The carbonyl oxygen has a stronger electron donor interaction with copper compared to the sulfur from Met, and consequently lowers the redox potential of copper (Holm *et al.* 1996). The example of the blue copper proteins demonstrates that by changing the type and number of ligands to the metal, the protein environment can fine tune the redox potential of the metal center.

Superoxide dismutases (SODs) are a family of metalloproteins that catalyze the disproportionation of superoxide into oxygen and hydrogen peroxide.

$$2O_2^- + 2H^+ \rightarrow O_2 + H_2O_2 \qquad 1.1.f$$

SODs are vital for organisms utilizing oxygen for metabolism because superoxide generated during oxygen metabolism can be harmful or even lethal to the organism (Bertini 2007). SODs with different metal ions have been discovered. Copper, iron, manganese and nickel have all been reported to serve in the catalytic center of various SODs. The active sites of CuSOD, FeSOD, MnSOD and NiSOD are shown in Figure 1.1.c.

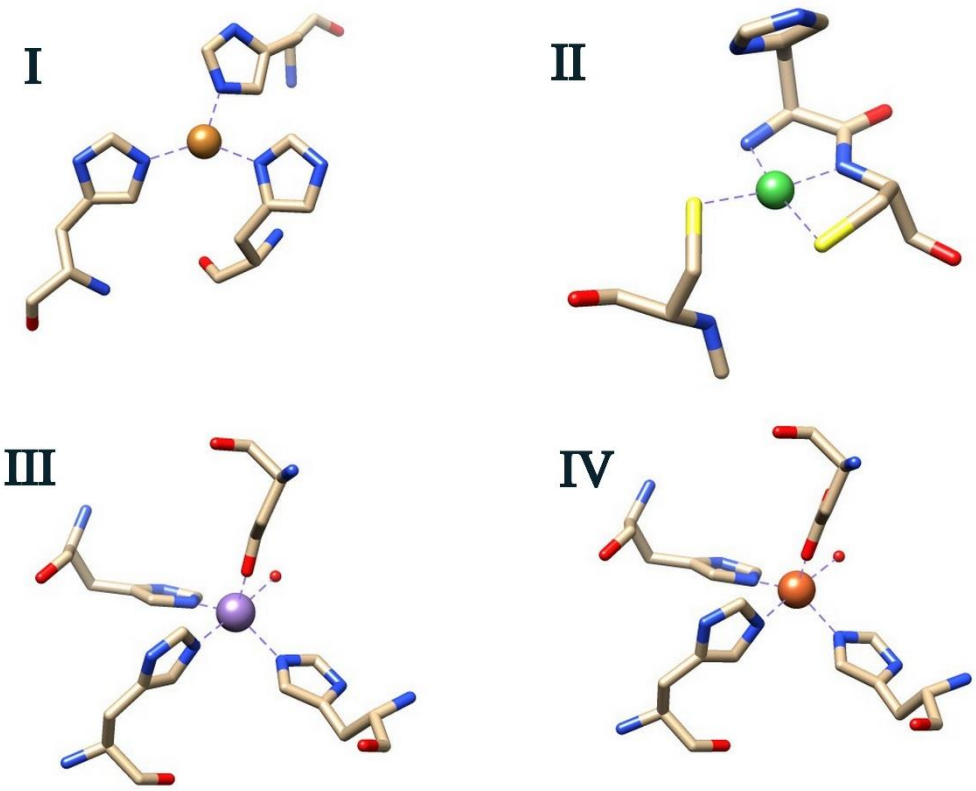

Figure 1.1.c Active site structures of reduced form of four SODs. I) CuSOD, PDB: 2JCW, (Hart *et al.* 1999). II) NiSOD, PDB: 1Q0K, (Wuerges *et al.* 2004). III) MnSOD, PDB: 1VEW, (Edwards *et al.* 1998). IV) FeSOD, PDB 4L2D, (Merlino *et al.* 2014). Carbon (grey), nitrogen (blue), oxygen (red), sulfur (yellow), copper (dark yellow ball), nickel (green ball), manganese (purple ball), iron (orange ball). Purple dashed lines denote the metal-ligand bonds. The diagrams were generated using Chimera (Pettersen *et al.* 2004).

The disproportionation of superoxide can be divided into two half reactions:

$$O_2^- - e^- \rightarrow O_2 \qquad E^0 = -180 \text{ mV} \qquad 1.1.g$$

$$O_2^- + 2H^+ + e^- \rightarrow H_2O_2 \qquad E^0 = +910 \text{ m V} \qquad 1.1.h$$

A simplified mechanism of SOD can be written as:

$$O_2^- + SOD_{ox} \rightarrow O_2 + SOD_{red} \qquad 1.1.i$$

$$O_2^- + 2H^+ + SOD_{red} \rightarrow H_2O_2 + SOD_{ox} \qquad 1.1.j$$

In principle, any redox pair whose mid-point potential lies between -180 mV and +910 mV under standard conditions could have SOD activity, and ideally the optimal potential would be 360 mV, midway between -180 and +910 mV, to give both the half reactions enough driving force. The redox potential was determined as +400 mV for CuSOD (Fee and DiCorleto 1973), +260 mV for FeSOD (Barrette *et al.* 1983), +310 mV for MnSOD (Lawrence and Sawyer 1979) and +290 mV for NiSOD (Herbst *et al.* 2009). All of these potentials lie between the required -180 to +910 mV region, therefore, they can serve as SODs.

As shown in Figure 1.1.c III and IV, the active sites of MnSOD and FeSOD closely resemble each other. In the native proteins, Fe and Mn cycle between the +2 and +3 oxidation states during the SOD catalytic cycle. For aqueous ions, $E^{0'}$ of $[Fe(H_2O)_6]^{2+}/[Fe(H_2O)_6]^{3+}$ and $[Mn(H_2O)_6]^{2+}/[Mn(H_2O)_6]^{3+}$ are 770 mV and 1510 mV, respectively (Speight and Lange 2005). Both FeSOD and MnSOD possess $E^{0'}$ around 300 mV, indicating that the native protein environment of FeSOD and MnSOD is able to lower the mid-point potential of their respective metal ions. Surprisingly, many Fe-substituted-MnSODs (Fe-sub-MnSOD) or Mn-substituted-FeSODs (Mn-sub-FeSOD) are inactive in the standard catalytic assay (Yamakura 1978, Ose and Fridovich 1979). It turns out that the mid-point potential of neither Fe-sub-MnSOD nor Mn-sub-FeSOD falls between the values of -180 to +910 mV, thus they are unable to mediate both half reactions effectively (Vance and Miller 1998). Substituting the Mn with Fe in MnSOD results in a very low potential of -240 mV, and substituting the Fe with Mn in FeSOD results in a very high potential of

+960 mV, and therefore neither of the substituted SODs can catalyze the two reactions (Vance and Miller 1998).

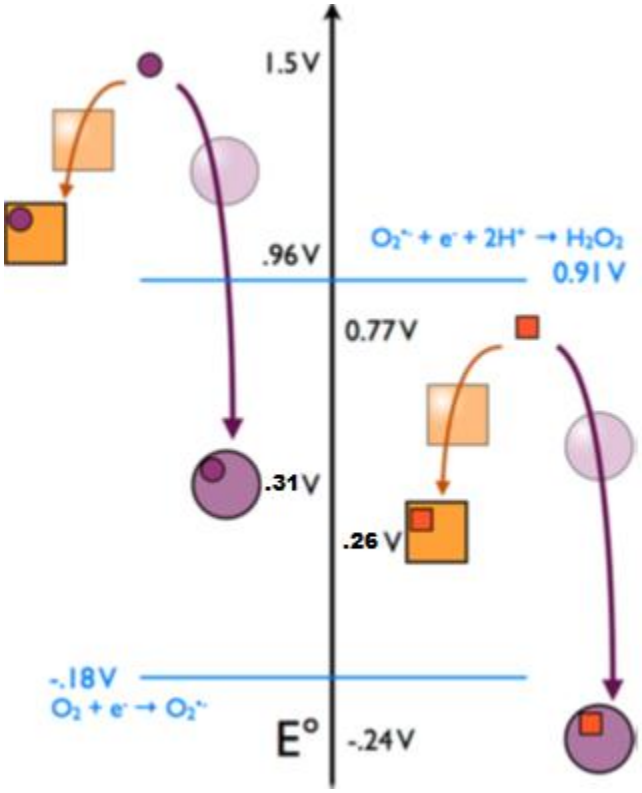

Figure 1.1.d Cartoon of the different redox tuning by the FeSOD and MnSOD proteins. Orange squares depict the FeSOD protein and violet circles represent the MnSOD protein; the corresponding metal ions are shown as red squares or purple circles. Apo-proteins lack the symbol for the metal ion. Reduction potentials vs NHE are marked on the vertical axis, and the protein-metal ion complexes or hexa aquo complexes are positioned vertically in accordance with this scale. Figure modified from (Sheng *et al.* 2014).

1.2 *De novo* design of metalloproteins

Many biochemical approaches towards studying natural proteins involve the loss of functions. In contrast, *de novo* metalloprotein design takes another direction by building a structure and creating a function from scratch (DeGrado *et al.* 1999). *De novo* design aims to design peptide sequences that have no direct homology with any naturally

occurring sequences, and possess certain structures or functions that may or may not exist in nature (Lu *et al.* 2009).

1.2.1 Stable secondary structure of peptides induced by metal ion

For some *de novo* designed metallopeptides, the apopeptides do not possess any specific secondary structure other than random coil, while in the presence of metal ions, the peptides are directed into folding and assembling into a more stable secondary structure to accommodate the metal ion. Suzuki and coworkers reported a *de novo* designed peptide that in apoform had a random coil structure in aqueous solution, while in the presence of first-row transition metals such as Ni(II), Cu(II) or Co(II) at pH 7, the peptide folded into a three-stranded coiled coil structure shown in Figure 1.2.a (Suzuki *et al.* 1998). Besides first-row transition metals, second-row transition metals such as Cd(II) (Li *et al.* 2000, Kharenko and Ogawa 2004), and third-row transition metals such as Hg(II) (Li *et al.* 2000, Farrer and Pecoraro 2003) also have been shown to induce changes of the secondary structure of *de novo* designed peptides.

Figure 1.2.a Tertiary model of a Ni(II) complex. A side view (right) and a bottom view from the C-termini (left) of the peptide-metal complex are shown. The six His side chains (sticks) are shown with the three helix backbones. The Ni(II) is indicated by a sphere. Figure adapted from (Suzuki *et al.* 1998).

In 2006, Rockcliffe and coworkers reported a *de novo* designed dinucleating Cu(II) binding peptide which they named HGP (Rockcliffe *et al.* 2006). The peptide has the sequence as Ac-WGHGHGHGPGHGHGH-NH_2. The authors designed two copper binding domains each composed of three histidines. A proline was positioned in the middle of the sequence to form a β turn and result in the two metal-binding regions being close together. The Trp was used as an optical tag to facilitate concentration determination of the peptide. An energy-minimized model of this Cu^{2+}/HGP complex is shown in Figure 1.2.b.

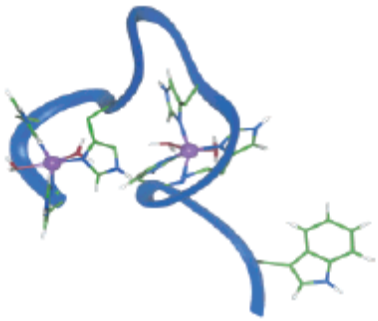

Figure 1.2.b Energy-minimized model of the Cu/HGP complex showing the copper binding region and the turn conformation. Figure adapted from (Rockcliffe *et al.* 2006).

In the absence of Cu(II), HGP was in a random coil structure in solution. However, the circular dichroism (CD) spectra showed a negative band between 220 and 230 nm upon addition of Cu(II), indicating that the peptide undergoes a Cu(II) induced structural change for pH values at 9.0 and above (Figure 1.2.c). The binding of Cu(II) was monitored using CD and yielded a stoichiometry of 2:1 for Cu(II):HGP (Figure 1.2.d), which was confirmed by mass spectroscopy (Rockcliffe *et al.* 2006).

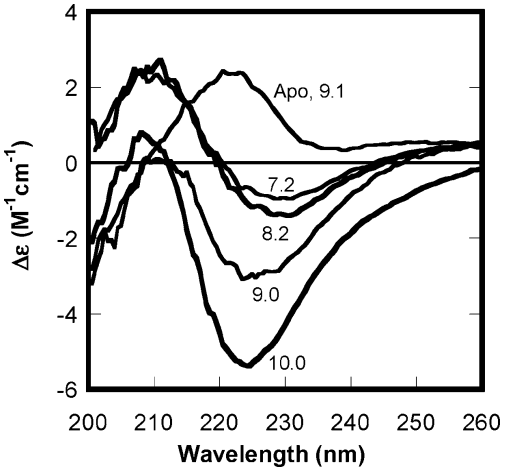

Figure 1.2.c CD spectra of 2:1 Cu^{2+}/HGP solutions of Cu-HGP (20 μM) within the pH range 7-10 compared with the apopeptide at pH 9.1. The pH values are indicated on the curves. Figure adapted from (Rockcliffe *et al.* 2006).

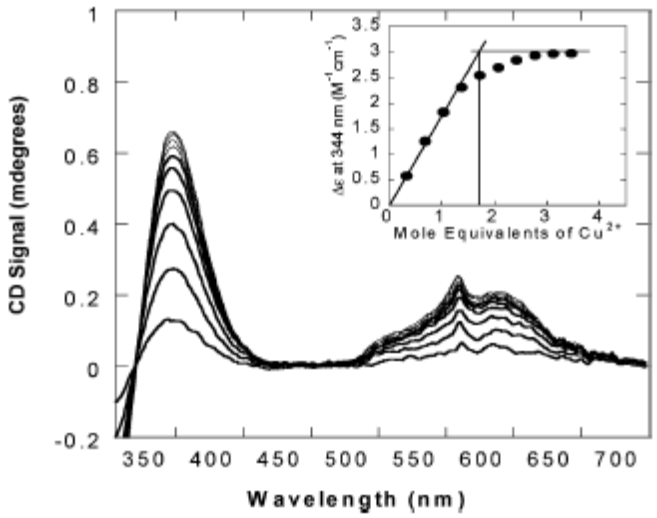

Figure 1.2.d Cu^{2+} addition to a solution of HGP (200 μM) at pH 9.2 followed by CD. Inset: Binding curve showing the dependence of Δε at 344 nm on the mole equivalents of added Cu^{2+}. The Cu^{2+} saturation point is at 1.8 mol equiv. Figure adapted from (Rockcliffe *et al.* 2006).

CD spectra of Cu/HGP were recorded at pH values ranging from 4 to 9, and the CD signal at 344 nm was plotted against pH as shown in Figure 1.2.e. The data were fitted using Equation 1.2.a (Rockcliffe *et al,* 2006)

$$\Delta\varepsilon = \{\Delta\varepsilon_{acid}[H^+]^n + \Delta\varepsilon_{base}K_a^n\}/\{[H^+]^n + K_a^n\} \qquad 1.2.a$$

where n is the Hill coefficient and K_a is the acid dissociation constant. The fitting yielded a Hill coefficient number of 1.6, indicating that the two copper-binding sites showed a moderate positive cooperativity (Rockcliffe *et al,* 2006).

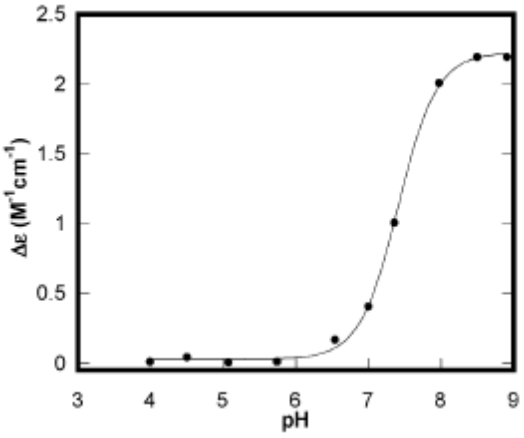

Figure 1.2.e Cu/HGP pH dependence of Δε at 344 nm. Figure adapted from (Rockcliffe *et al.* 2006).

1.2.2 Metalloprotein design using *de novo* scaffolds

In addition to metal-induced formation of secondary structures, peptides with stable secondary structures can be used as scaffolds to bind metal ions. Most of the work involving *de novo* designed metallopeptides has employed *de novo* designed α-helix bundles as scaffolds to host metal-binding sites (Lu *et al.* 2009). In 2000, DeGrado and coworkers reported a *de novo* designed model peptide for a di-iron protein, which they named DF1 (Figure 1.2.f) (Lombardi *et al.* 2000). DF1 self-assembles into a dimer to form a four-helix bundle, which is able to accommodate metal ions such as Zn(II), Fe(II), Co(II) and Mn(II) (Lombardi *et al.* 2000). This is the first example of a *de novo* designed dinuclear metallopeptide based on a rigid protein scaffold. Later, the same group reported DF_{tet}, a derivative of DF1, which served as an enzyme to catalyze the two-electron oxidation of 4-aminophenol by oxygen (Kaplan and DeGrado 2004). In 2005, DeGrado and coworkers achieved a redox active rubredoxin mimic based on a *de novo* designed β-structure that was able to bind a Fe(II)/Fe(III) center (Figure 1.2.g) (Nanda *et al.* 2005).

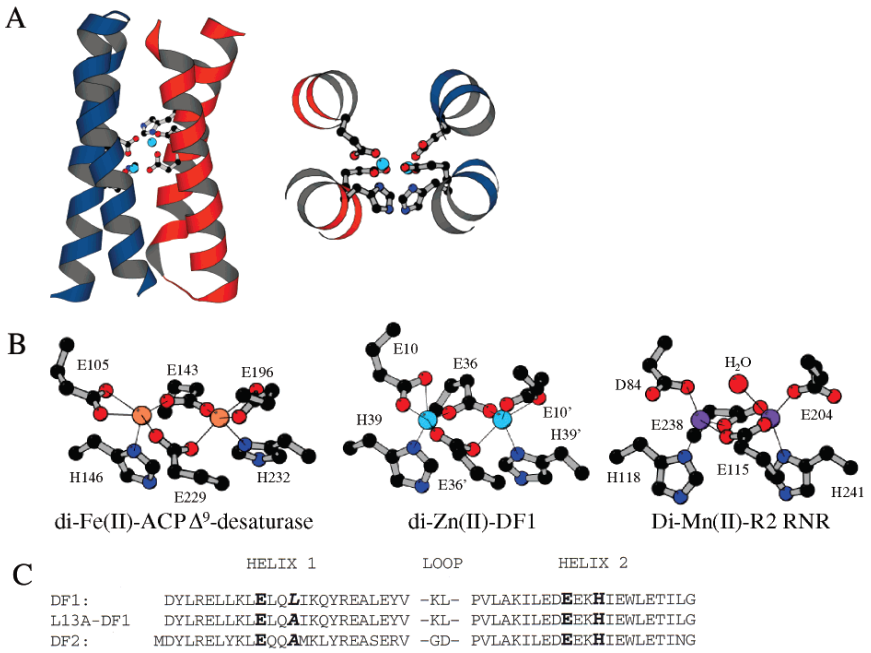

Figure 1.2.f Crystal structure of di-Zn(II)-DF1. (A) Side view and top view of the helix-turn-helix homodimer (monomers are colored orange and blue) shown with the liganding residues and the active site Zn^{2+} metal ions (light blue). (B) Dinuclear metal centers of two natural proteins, ACP Δ^9-desaturase (left) and the manganese-substituted R2 subunit of the *E. coli* ribonucleotide reductase (right), along with the di-Zn(II)-DF1 (middle). (C) Amino acid sequences of DF1, L13A-DF1 and DF2. The active site ligands are highlighted in bold, and the Leu to Ala change is shown in italic. Figure adapted from (Di Costanzo *et al.* 2001).

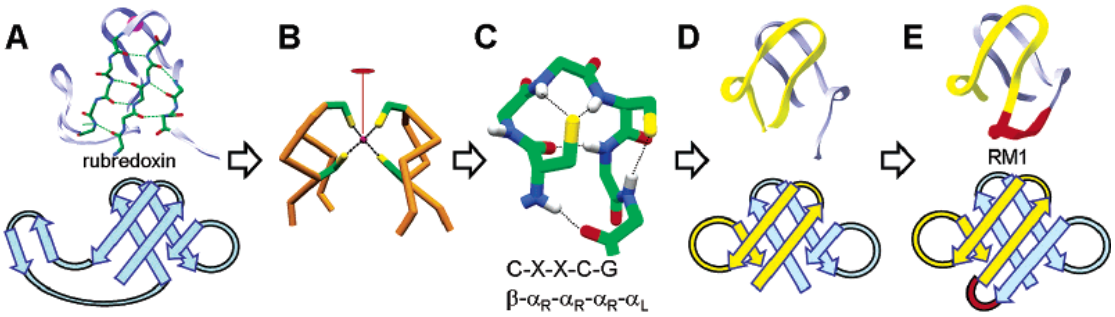

Figure 1.2.g RM1 design cycle: (A) three-stranded sheet topology of natural rubredoxin, (B) C2 symmetry, (C) active-site geometry, (D) miniRM dimer and (E) RM1 with Trpzip linker shown in red. Figure adapted from (Nanda *et al.* 2005).

1.3 Photosynthesis

1.3.1 Introduction

Photosynthetic organisms capture energy from sunlight and store the energy in the form of chemical bonds (Blankenship 2014). Photosynthesis can be divided into two subtypes as oxygenic photosynthesis and anoxygenic photosynthesis (Blankenship 2014). Oxygenic photosynthesis is the predominant process compared to anoxygenic photosynthesis in terms of the amount of solar energy converted. Briefly, in oxygenic photosynthesis, the energy from photons is used to oxidize water and reduce carbon dioxide into organic compounds (Equation 1.3.a).

$$CO_2 + H_2O \xrightarrow{h\nu} O_2 + CH_2O \qquad 1.3.a$$

In oxygenic photosynthesis, water oxidation occurs in photosystem II (Figure 1.3.a) where molecular oxygen is produced in a four-electron and four-proton process:

$$2\ H_2O \rightarrow O_2 + 4\ H^+ + 4\ e^- \qquad 1.3.b$$

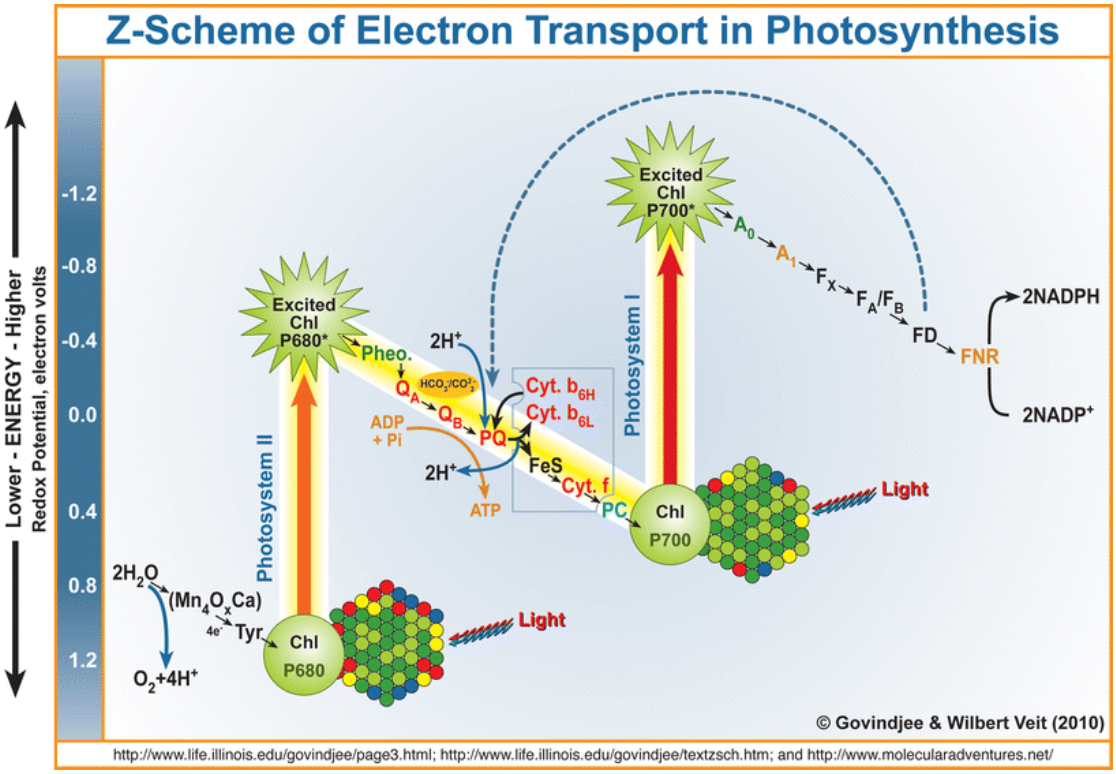

Figure 1.3.a. The Z-scheme diagram of oxygenic photosynthesis. The electron transport from H_2O to nicotinamide adenine dinucleotide ($NADP^+$) is traced from left to right on the diagram that uses two Photosystems (I and II). This process is initiated by the simultaneous absorption of light by two antenna complexes, represented by clusters of colored balls. The absorbed energy is then transferred to the reaction center chlorophylls (Chl) P680 and P700 and this powers the entire process. (Mn_4O_x Ca) is the manganese center, a complex containing four manganese atoms, which participates in the splitting of two water molecules into four protons ($4H^+$), four electrons ($4e^-$), and one oxygen molecule (O_2). Tyr is a redox active tyrosine molecule, also sometimes referred to as Y_z or simply as Z, which acts as an intermediate between the manganese center and "reaction center" of Photosystem II, PSII (P680), a chlorophyll (Chl) complex. Excited P680* has the energy of the photon that was captured by and transferred to it from its light-gathering antenna complex (cluster of colored balls). Pheo is pheophytin, a chlorophyll with its central magnesium ion (Mg^{2+}) replaced by two protons; it is the primary electron acceptor of PSII, whereas P680* is the primary electron donor. Q_A is a plastoquinone, which is tightly bound and immovable. It is also known as the primary stable electron acceptor of PSII, and it accepts and transfers one electron at a time. Q_B is a loosely bound plastoquinone molecule which accepts two electrons and two protons; HCO_3^- (bicarbonate) and CO_3^{2-} (carbonate) play an essential role here. Q_BH_2, reduced Q_B, then detaches, and becomes mobile, shuttling the two electrons and two protons within the hydrophobic core of the thylakoid membrane to the cytochrome b_6/f complex (the rectangle in the center of the diagram). FeS is the Rieske iron–sulfur protein. Cyt f is cytochrome f. Cyt.b_6L and Cyt.b_6H are two cytochrome b_6 molecules (of lower and higher potentials) which participate in the Q cycle. PC is plastocyanin, a highly mobile copper protein. P700 and Excited P700* are Chls in the reaction center of Photosystem I

in the ground and excited energy state, respectively. A_O is a special chlorophyll a molecule that is the primary electron acceptor of PSI, whereas P700* is the primary electron donor of PSI. A_1 is a phylloquinone (vitamin K) molecule. F_X, F_A, and F_B are three separate immobile iron sulfur protein centers. FD is ferredoxin, a mobile iron sulfur protein, which can participate, along with other iron sulfur centers, in cyclic transport (dashed blue line). FNR is the enzyme ferredoxin-NADP oxidoreductase, which enables $NADP^+$ to accept two electrons and a proton and become NADPH, the reduced form of $NADP^+$. The overall process concentrates protons into the thylakoid lumen, producing an energy gradient that is used in the production of ATP from ADP and inorganic phosphate (Pi) via ATP synthase. Figure adapted from (Orr and Govindjee 2010).

1.3.2 Oxygen Evolving Complex (OEC) in Photosystem II (PSII)

Water oxidation (Equation 1.3.b) is a difficult reaction from both a thermodynamic point and a kinetic view. Water oxidation occurs with a thermodynamic potential of 1.23 V – 0.059 * (pH) against the normal hydrogen electrode (NHE). Thus, it requires a significant amount of energy input to drive this reaction, which is provided by photons in oxygenic photosynthesis. Due to its intriguing function of oxidizing water, oxygenic photosynthesis has long been extensively studied. Cheniae and Martin have demonstrated that oxygenic photosynthesis is dependent on Mn (Cheniae and Martin 1969, Cheniae and Martin 1970). In 1981, electron paramagnetic resonance experiments on spinach chloroplasts indicated that a Mn tetramer might be involved in photosynthetic oxidation of water (Dismukes and Siderer, 1981). Recent structural progress has shown the water oxidation site to have a Mn_4CaO_5 core structure stabilized by mostly carboxylate and nitrogen ligands as shown in Figure 1.3.b (Umena *et al.* 2011).

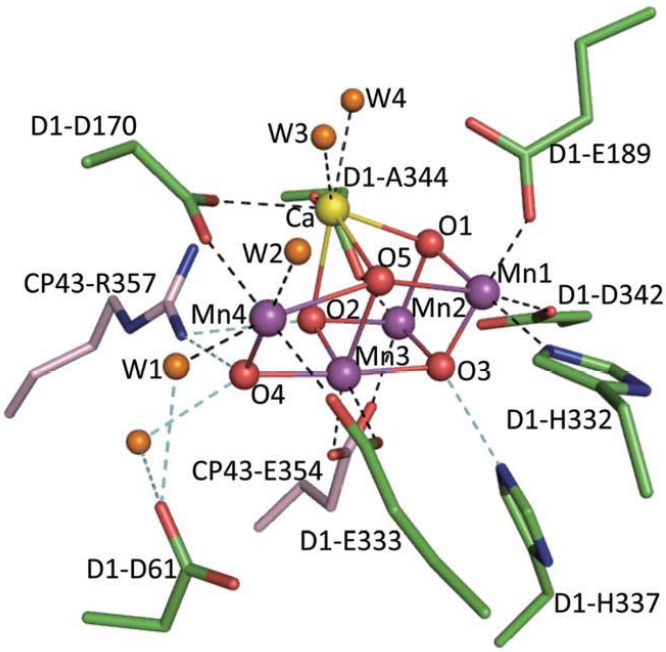

Figure 1.3.b. Structure of the Mn_4CaO_5 cluster and its protein environment. Manganese, purple; calcium, yellow; oxygen, red; nitrogen, blue; D1 subunit, green; CP43 subunit, pink. Figure adapted from (Umena *et al.* 2011).

1.3.3 Elucidating the water oxidation mechanism

In 1969, Joliot and coworkers reported that the oxygen formation yield of the green alga *Chlorella*, upon exposure to a series of saturating flashes of visible light, showed a period-of-four oscillation (Figure 1.3.c) (Joliot *et al.* 1969). Kok and coworkers proposed the now famous S-state model (also named Kok cycle) to explain the period-of-four oscillation (Kok *et al*, 1970). In their model (Figure 1.3.d), the active species sequentially goes through S_1, S_2, S_3, S_4 and S_0 oxidation states upon each flash, and the S_4 state is very unstable and relaxes to S_0 upon formation meanwhile releasing molecular oxygen (Kok *et al*, 1970).

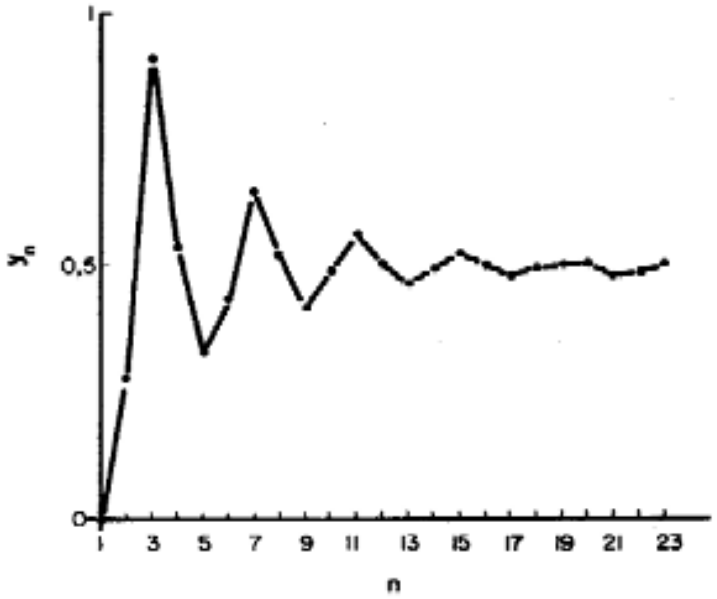

Figure 1.3.c Period-of-four oscillation of oxygen yield. Oxygen evolved (y_n) by a series of saturating flashes (n) given 300 ms apart to a dark-adapted suspension of the green alga *Chlorella*. Figure adapted from (Joliot *et al.* 1969, Joliot 2005).

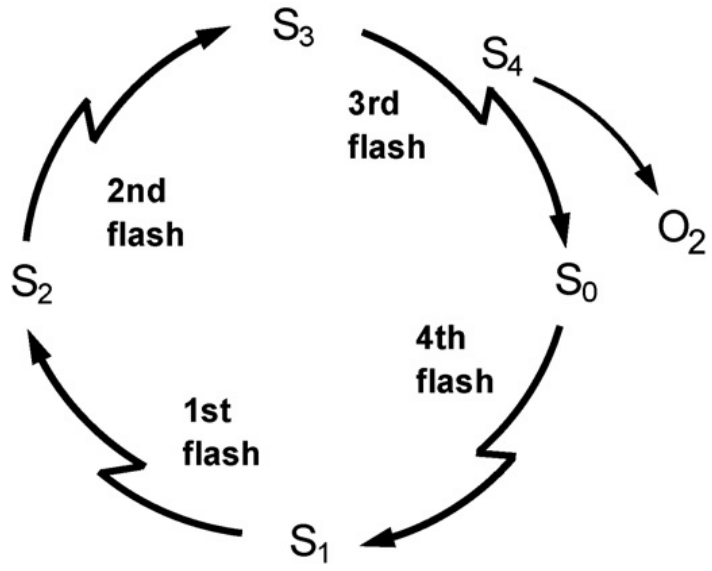

Figure 1.3.d. S-state cycle as originally proposed by Kok and coworkers. Figure adapted from (Dau and Haumann 2008).

The Kok cycle has since served as a foundation to elucidate the water oxidation mechanism of photosynthesis. However, even with the availability of high resolution of PSII crystal structure, the detailed molecular mechanism of water oxidation is still unknown and in debate (McEvoy and Brudvig 2006, Grundmeier and Dau 2012, Najafpour *et al.* 2012, Vinyard *et al.* 2013). Challenges in elucidating the water oxidation mechanism by PSII are summarized below according to (Dau and Haumann 2008, Dau *et al.* 2012):

a. A high-resolution crystal structure of PSII is available only in a dark state, with the Mn_4Ca cluster being highly reduced due to radiation damage.

b. How the substrate water molecules interact with the Mn_4Ca cluster is not known.

c. The oxidation states of the Mn_4Ca cluster during different S states are debated.

d. The protonation states and dynamics of key groups during water oxidation need to be elucidated.

1.4 Artificial photosynthesis

1.4.1 Introduction

The average worldwide human energy consumption rate was 16.2 TW in 2007, and by conservative estimation, this rate is going to double by 2050 (Cook *et al.* 2010), which requires human society to provide approximately another 16 TW of energy output in half a century. Fossil fuels cannot be a long-term solution for human energy needs since they are not renewable and have unwanted environmental impacts such as global warming (Vitousek 1994). Replacing fossil fuels with inexpensive renewable clean energy remains a challenge for human society. Sunlight seems an attractive energy source

to fulfill the requirements. On average, the sun delivers energy at the rate of about 120,000 TW to the earth's surface (Gust *et al.* 2009). Capturing 0.027% of the sunlight energy reaching the earth would provide enough energy for the projected 2050 demand. However, the energy of sunlight is diffused and intermittent, and therefore requires new ways to store it. Artificial photosynthesis aims to apply the principles learned from nature to capture the solar energy as chemical bonds such as hydrogen shown in Equation 1.4.a (Gust *et al.* 2009).

$$2\ H_2O \xrightarrow{h\nu} O_2 + 2\ H_2 \qquad 1.4.a$$

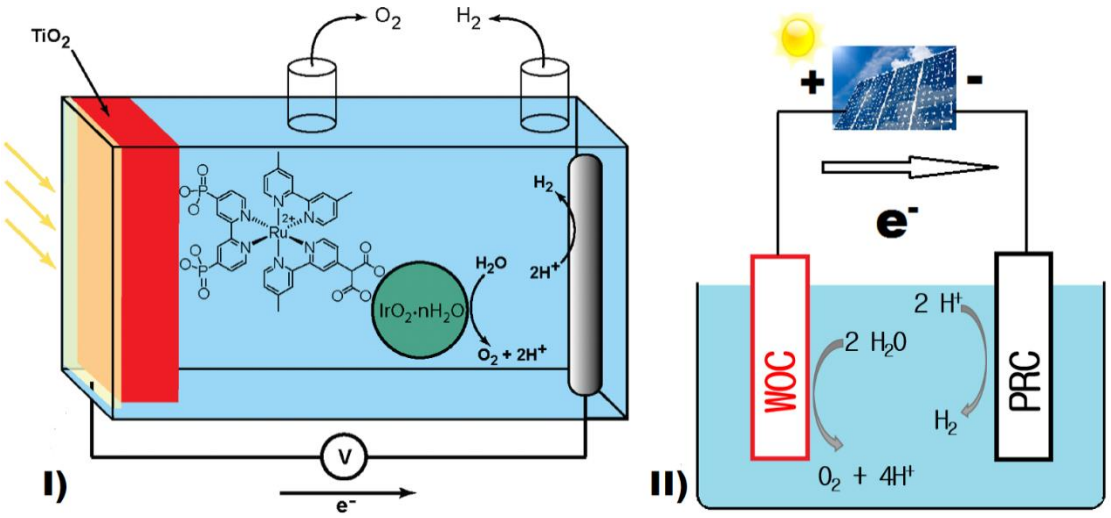

Figure 1.4.a. Schematic diagram of direct type and indirect type artificial photosynthetic water splitting cells. I) A direct type artificial photosynthetic water splitting cell. The nanoparticulate TiO_2 photoanode is sensitized with a ruthenium complex that also binds an iridium oxide nanoparticle. The excited ruthenium complex injects electrons into the TiO_2, from where they travel to the cathode and reduce hydrogen ions to hydrogen gas when a small bias voltage is applied. The oxidized ruthenium complex in turn oxidizes an iridium oxide nanoparticle that serves as a water oxidation catalyst. Figure 1.4.a.I adapted from (Gust *et al.* 2009, Gust *et al.* 2012). II) An indirect type artificial photosynthetic water splitting cell. A solar panel turns light energy into electricity. The solar panel generated potential is used as the driving force. Water is oxidized at the anode in the presence of a water oxidation catalyst (WOC), and protons are reduced at the cathode in the presence of a proton reduction catalyst (PRC).

In general, artificial photosynthetic water splitting cells can be grouped into two types (Cook *et al.* 2010). In the direct solar cell, the catalysts are coupled to a semiconductor, and the catalysts capture the photogenerated electron-hole pairs directly. An indirect solar cell relies on a photovoltaic cell to provide the driving force to split water. Both types have been achieved in the lab (Figure 1.4.a). In a direct type cell shown in Figure 1.4.a.I, upon illumination, a photosensitizer Ru complex is oxidized and donates an electron to TiO_2 semiconductor conduction band, with the electron transferred to the cathode for proton reduction. The oxidized Ru complex is reduced by IrO_2, which later oxidizes water into protons and molecular oxygen (Youngblood *et al.* 2009).

1.4.2 Water Oxidation Catalysts (WOCs) are required in sustainable solar water splitting

For an artificial photosynthetic water splitting cell to proceed with good efficiency, catalysts are required. Between water oxidation catalysts and proton reduction catalysts, WOCs are more demanding due to the fact that they catalyze a reaction involving the removal of four electrons from two water molecules and the formation of two oxygen-oxygen bonds. More details about the progress on artificial WOCs are introduced in Chapters 1.5 and 1.6.

1.4.3 Criteria for a good catalyst

For any chemical reaction to happen, certain energy is needed for the reactant to overcome the energy barrier existing between the reactant and the reaction intermediate, and this energy is termed the activation energy. The activation energy in electrochemistry is represented by an overpotential (η). In practice, voltage in excess of the thermodynamic value (reversible potential) must be applied to drive the desired reaction.

In general, the operation voltage V_{op} could be describe as (Cook *et al.* 2010):

$$V_{op} = E_{rev} + \eta_a + |\eta_c| + \eta_\Omega \qquad 1.4.d$$

Where η_Ω denotes the voltage loss due to the resistance in the cell, η_a and η_c represent the overpotential required to overcome the kinetic energy barriers on the anode and cathode respectively, and E_{rev} represents the thermodynamic potential of the reaction.

The η_a or η_c is an intrinsic property of the catalyst on the electrode, and it also depends on the current density (j) as demonstrated by Julius Tafel (Tafel 1905):

$$\eta = a + b \log(j) \qquad 1.4.e$$

Where b is the Tafel slope, and a is a constant.

Given the logarithmic relationship between overpotential and current density, it is vital to report the overpotential of a catalyst at a defined current density.

The criteria for a good water oxidation catalyst in practical use are summarized below according to (Cook *et al.* 2010):

a. A low Tafel slope is desired.

b. The catalyst must be composed exclusively of earth-abundant elements.

c. Construction should be low cost.

d. The catalyst should be stable on a time scale of years and beyond.

e. The catalyst should sustain high current density at a modest overpotential over a wide pH range and electrolyte composition.

So far, no water oxidation catalyst has met all the criteria listed above. Therefore, developing new water oxidation catalysts with diverse properties remains an important and challenging task for the research community (Cook *et al.* 2010).

1.5 Artificial water oxidation catalysts

Catalysts can be divided into two general categories as homogenous catalysts and heterogeneous catalysts. Homogeneous catalysts are soluble and the catalysis happens homogeneously throughout the solution, while heterogeneous catalysts often are insoluble or have limited solubility and the catalysis usually happens on the surface or more precisely the phase boundary between the catalyst and the solution. Homogeneous WOCs can be readily studied by most spectroscopic techniques, thus making it easier to elucidate the detailed catalytic mechanism including detecting and isolating the reaction intermediates. Homogeneous WOCs are also called molecular WOCs, because every molecule of the catalyst could catalyze the reaction. Later in the text, homogeneous WOCs and molecular WOCs will be used interchangeably. Heterogeneous WOCs prevail in practical use thanks to their robustness and ease of separation (Fukuzumi and Hong 2014). However, hindered by the heterogeneity within the catalyst, it is extremely difficult to isolate and characterize the reaction intermediates for heterogeneous WOCs. Understanding of the mechanism of heterogeneous WOCs is often limited.

1.5.1 Homogeneous WOCs

The molecular WOC, cis,cis-$[(bpy)_2(H_2O)Ru^{III}ORu^{III}(H_2O)(bpy)_2]^{4+}$ (Figure 1.5.a) reported in 1982 by Meyer and coworkers (Gersten *et al.* 1982) has since been referred to as a blue dimer. The blue dimer has a dinuclear Ru center bridged by one oxygen. It catalyzes the oxidation of water by the chemical oxidant Ce(IV) in strongly acidic conditions as shown in Equation 1.5.a.

$$4\ Ce(IV) + 2\ H_2O \rightarrow 4\ Ce(III) + O_2 + 4H^+ \qquad 1.5.a$$

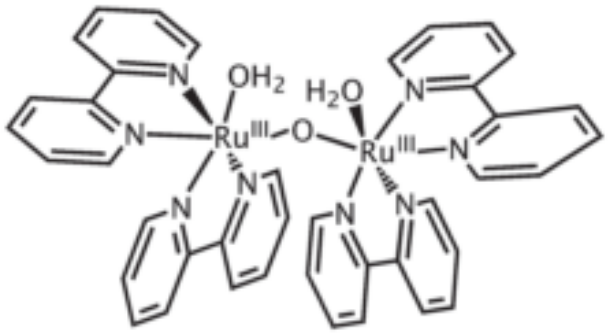

Figure 1.5.a Fisher projection of the blue dimer. Figure adapted from (Zong and Thummel 2005).

The blue dimer and its derivatives have been serving as a model system to elucidate the molecular mechanism of water oxidation, which will be elaborated in Chapter 1.6. Up until quite recently, it was generally believed that two or more coupled metal centers are necessary to catalyze the water oxidation process. This assumption was challenged by Meyer and coworkers reporting two single-site Ru molecular WOCs as $[Ru(tpy)(bpm)(OH_2)]^{2+}$ and $[Ru(tpy)(bpz)(OH_2)]^{2+}$ (tpy is 2,2':6',2'-terpyridine; bpm is 2,2'-bipyrimidine; bpz is 2,2'-bipyrazine) (Concepcion *et al.* 2008).

By changing the organic ligands around the metal center, more and more WOCs have been developed. Molecular WOCs employing Ir, Co, Ni, Fe, Mn, Cu have also been reported (McDaniel *et al.* 2008, Cady *et al.* 2010, Ellis *et al.* 2010, Yin *et al.* 2010, Barnett *et al.* 2012, Shaw *et al.* 2013). However, the harsh oxidizing environment required by water oxidation tends to oxidize the organic ligands to the metal center in the catalyst, leading to decomposition of the catalyst and subsequent loss of function. Hill and coworkers reported a homogeneous WOC with a Co_4O_{16} core stabilized by all

inorganic ligands, which was reported to show improved stability against oxidative stress (Yin *et al.* 2010). This catalyst has the formula as $[Co_4(H_2O)_2(PW_9O_{34})_2]^{10-}$ (Figure 1.5.b), and recorded, at the time, the highest turnover frequency (TOF) among artificial WOCs as about 5 s^{-1} (Yin *et al.* 2010), which since has been broken. A TOF of 300 s^{-1} was achieved by a mononuclear ruthenium complex $[Ru(bda)(isoq)_2]$ (H_2bda = 2,2'-bipyridine-6,6'-dicarboxylic acid; isoq = isoquinoline; Figure. 1.5.c) as reported by Duan and coworkers (Duan *et al.* 2012).

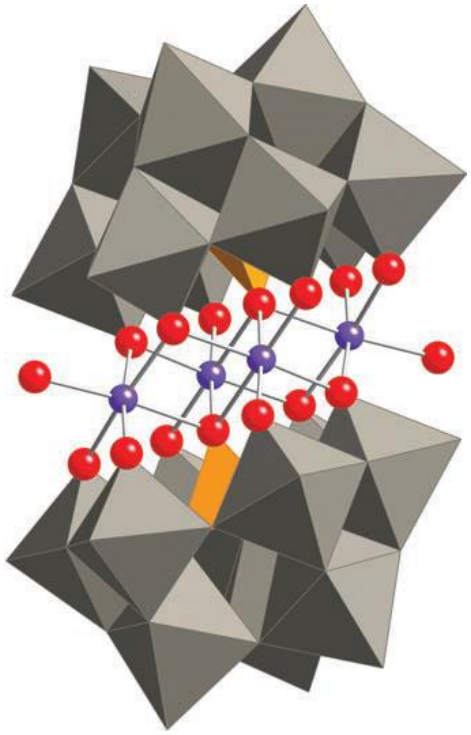

Figure 1.5.b X-ray structure of $Na_{10}[Co_4(H_2O)_2(PW_9O_{34})_2]$ in combined polyhedral ($[PW_9O_{34}]$ ligands) and ball-and-stick (Co_4O_{16} core) notation. Co atoms are purple; O/OH_2(terminal), red; PO_4, orange tetrahedra; and WO_6, gray octahedra. Hydrogen atoms, water molecules, and sodium cations are omitted for clarity. Figure adapted from (Yin *et al.* 2010).

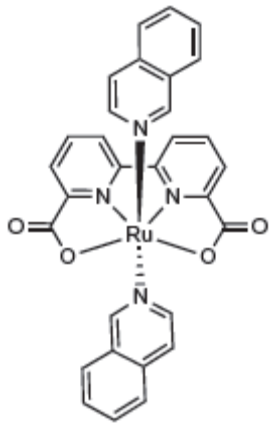

Figure 1.5.c Fisher projection of complex [Ru(bda)(isoq)$_2$]. Figure adapted from (Duan *et al*, 2012)

1.5.2 Heterogeneous WOCs

1.5.2.1 Precious metal oxides

The precious metal Pt has long been used as an electrode material due to its inertness under most conditions, although Pt electrodes can form oxides or hydroxides under extreme pH values, which can act as WOC (Bockris and Huq 1956, Birss *et al.* 1986, Conway and Liu 1990). Besides Pt, Ir oxides and Ru oxides were also reported to be efficient heterogeneous water oxidation catalysts (Nakagawa *et al.* 2009, Tsuji *et al.* 2011).

1.5.2.2 First-row transition metal oxides

In 2008, Kanan and Nocera reported a Co-based water oxidation catalyst that worked under neutral pH in phosphate buffer (Kanan and Nocera 2008). This discovery was profound in that Co-phosphate (CoPi) formed easily upon applying a potential, and served as a catalyst at neutral pH with a variety of proton-accepting buffers (Kanan and Nocera 2008, Surendranath *et al.* 2009). Contributions from both the Nocera group and others led to more understanding of the molecular mechanism of heterogeneous WOCs.

In 2010, Nocera and coworkers reported a Ni-based heterogeneous WOC in borate buffer at pH 9.2 (Dinca *et al.* 2010).

1.5.3 Molecular precursors to heterogeneous WOCs

Ru and Ir have both been reported to form homogeneous or heterogeneous WOCs. Homogeneous WOCs can decompose under harsh oxidizing environments (Fukuzumi and Hong 2014). Also, the same molecule may undertake different mechanisms under different conditions. For example, $Na_{10}[Co_4(H_2O)_2(PW_9O_{34})_2]$ was reported to be a homogeneous catalyst while using Ce(IV) as the oxidant (Yin *et al.* 2010) but was later shown to be a precursor to generate heterogeneous CoPi WOC under electrochemical conditions (Stracke and Finke 2011).

1.6 Mechanisms of artificial water oxidation catalysts

1.6.1 Ru molecular WOC

The blue dimer (Figure 1.5.a) has been serving as a model compound in studying the mechanism of homogenous WOC. Proton-coupled electron transfer (PCET) takes place during the blue dimer turnover to avoid high-energy intermediates, and a mechanism of water oxidation by the blue dimer was proposed (Figure 1.6.a) (Liu *et al.* 2008).

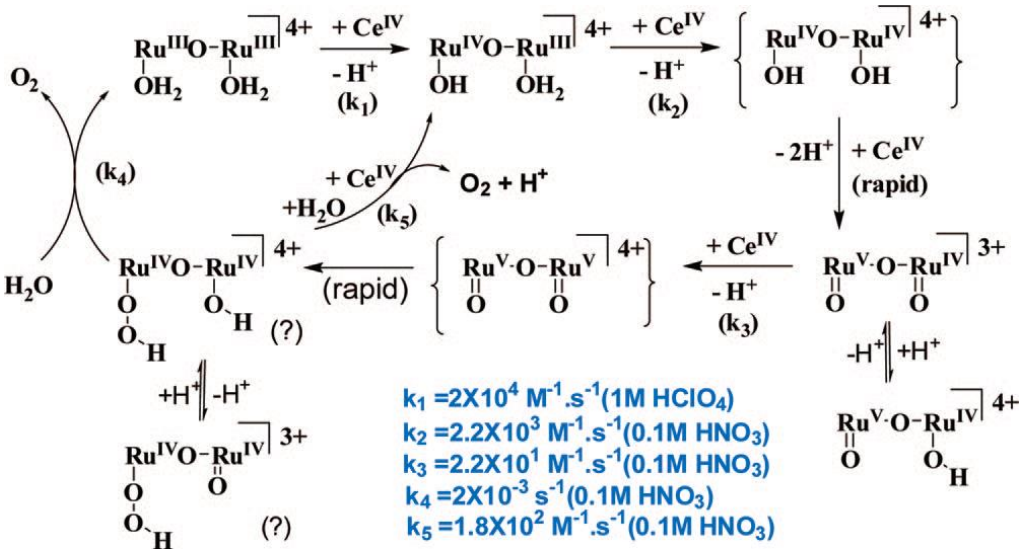

Figure 1.6.a. Proposed Mechanism for Oxidative Activation and Water Oxidation by the Blue Dimer. Figure adapted from (Liu *et al.* 2008).

In 2008, Meyer and coworkers reported the first single-site Ru monomeric complex as molecular WOC and detailed all the key steps in catalytic turnover (Concepcion *et al.* 2008). The proposed mechanism of this Ru single-site complex is shown in Figure 1.6.b. This challenged the long-held thought that a dimer or even higher order structures like the case found in PSII were necessary to catalyze the four-electron oxidation of water. This research opened the door to more single-site metal WOC, as since then Ir, Co or Fe containing single-site molecular WOCs have also been reported (Wasylenko *et al.* 2013).

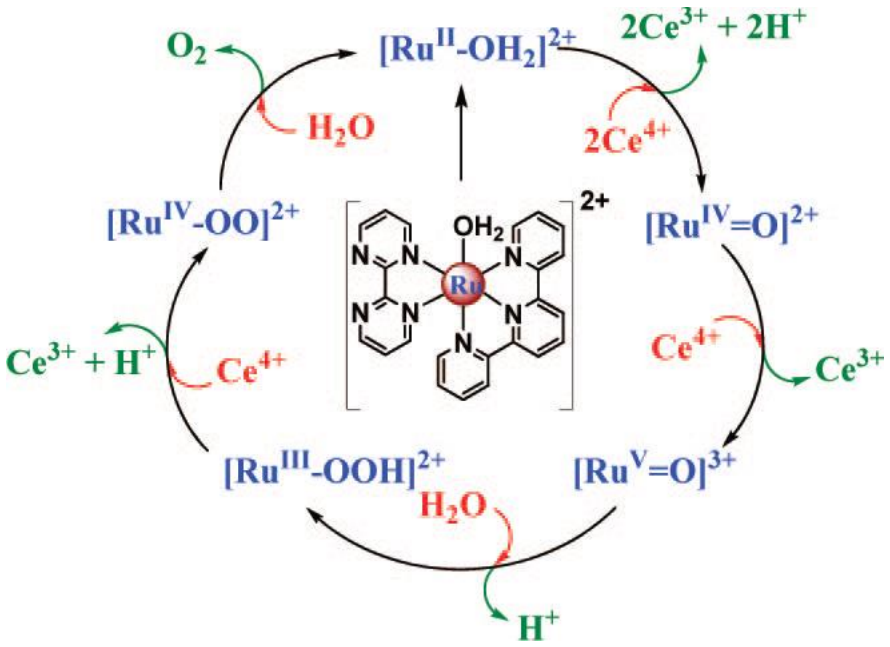

Figure 1.6.b. Proposed mechanism for water oxidation by the Ru monomer. Figure adapted from (Concepcion *et al.* 2008).

1.6.2 Copper-containing molecular WOCs

The first reported copper-containing molecular WOC was a self-assembled Cu-bipyridine complex (Barnett *et al.* 2012). No mechanism has been reported for this case. In 2013, Meyer and coworkers reported that Cu-tetraglycine (Cu-TGG) acted as a molecular catalyst in phosphate buffer at pH 11 (Zhang *et al.* 2013). Copper is coordinated by four nitrogen atoms in a plane, with water and a terminal carboxylate group completing the coordination (Figure 1.6.c).

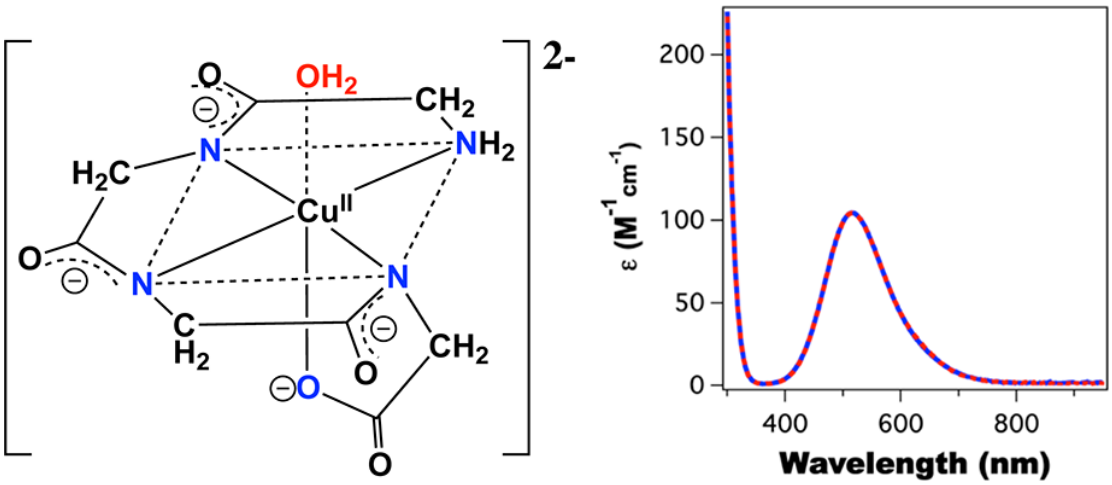

Figure 1.6.c (Left) Structure of the catalyst, $[(TGG^{4-})Cu^{II}–OH_2]^{2-}$. (Right) Its absorption spectrum in 0.25 M phosphate buffer at pH 11. Figure adapted from (Zhang *et al.* 2013).

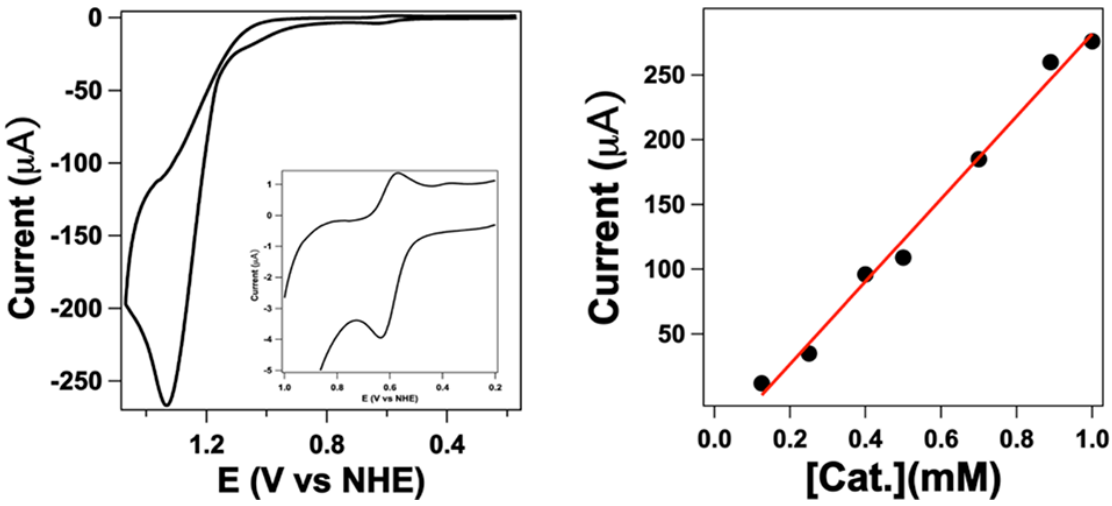

Figure 1.6.d (Left) CV in 0.25 M phosphate buffer (pH 11) at a GC electrode, 0.89 mM $[(TGG^{4-})Cu^{II}–OH_2]^{2-}$, scan rate = 10 mV/s. The inset shows a magnified view of the CuIII/II couple at $E_{1/2}$ = 0.58 V. (Right) Plot of catalytic peak current at $E_{p,a}$ = 1.32 V vs the concentration of catalyst. Figure adapted from (Zhang *et al.* 2013).

The cyclic voltammogram (CV) of 0.89 mM Cu-TGG in 0.25 M Na-Pi electrolyte at pH 11 using a glassy carbon electrode at 10 mV/s scan rate, shows an irreversible anodic catalytic wave peaking at 1.32 V vs NHE (Figure 1.6.d). Reversible CV peaks were centered at 0.58 V with 70 mV peak separation, and this feature was assigned to a

$Cu^{III/II}$ couple (Zhang *et al.* 2013). The CV current at 1.32 V exhibited a linear dependence of the Cu-TGG concentration from 0 to 1 mM (Figure 1.6.d). Cu-TGG was reported as a homogenous molecular WOC, and the authors proposed a mechanism (Figure 1.6.e).

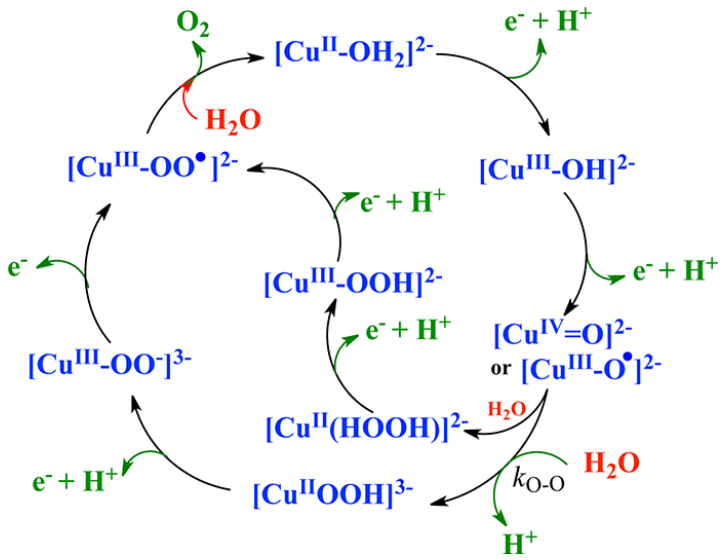

Figure 1.6.e. Proposed mechanism for water oxidation by Cu-TGG in phosphate buffer solutions at pH 11. Figure adapted from (Zhang *et al.* 2013).

1.6.3 Ir oxides

Relatively little is known about the mechanism employed by IrOx in catalyzing water oxidation. Sivasankar and coworkers used Fourier transform infrared spectroscopy to examine a hydroperoxide surface intermediate and proposed the formation of an Ir oxide nanocluster (Sivasankar *et al.* 2011) as shown in Figure 1.6.f.

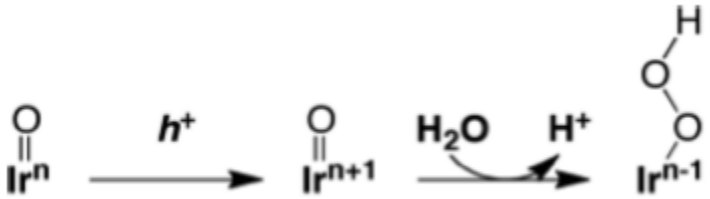

Figure 1.6.f. Proposed partial mechanism for water oxidation at the Ir oxide nanoparticle surface. Figure adapted from (Sivasankar *et al.* 2011).

1.6.4 CoPi WOC

Kanan and Nocera reported a cobalt-based water oxidation catalyst (CoPi) that worked under neutral pH conditions (Kanan and Nocera 2008). This catalyst was easily deposited onto the working electrode by electrolyzing a Co^{2+}-containing phosphate buffer at pH 7, and this derived catalyst film could catalyze water oxidation in Co^{2+}-free phosphate buffer. The authors reported an overpotential of 410 mV to sustain a current density of 1 mA/cm^2 (Kanan and Nocera, 2008). This was a breakthrough in WOC research. Unlike the previously mentioned Ir or Pt-containing heterogeneous catalysts that required precious metal and functioned in extreme pH conditions, the CoPi has a first-row transition metal, and works at near neutral pH. Still, the formation of the CoPi catalyst is much easier compared to most of the molecular WOCs, which often require tedious and complex synthesis. Since this initial report, research had been reported to expand our knowledge of this CoPi WOC. Surendranath and coworkers reported that besides the originally reported phosphate, methylphosphate and borate could also support the cobalt-based WOC (Surendranath *et al.* 2009). Meanwhile, the electrodeposition of the catalyst in a nonbuffered solution was negligible pointing to the vital role of a good

proton acceptor in catalyst formation and activity (Surendranath *et al.* 2009). Through elemental analysis and X-ray photoelectron spectroscopic data, Kanan and Nocera (2008) implied the nature of the catalyst as either cobalt oxide or hydroxide "incorporating a substantial amount of phosphate anion" (Kanan and Nocera 2008). It was not until the application of *in situ* X-ray spectroscopy during the CoPi turnover condition that one was able to approach the structure of the CoPi WOC. Based on extended X-ray absorption fine structure spectra, Kanan and coworkers proposed a structure model that the Co-Pi was composed of edge-sharing CoO_6 octahedra (Kanan *et al.* 2010) (Figure 1.6.g).

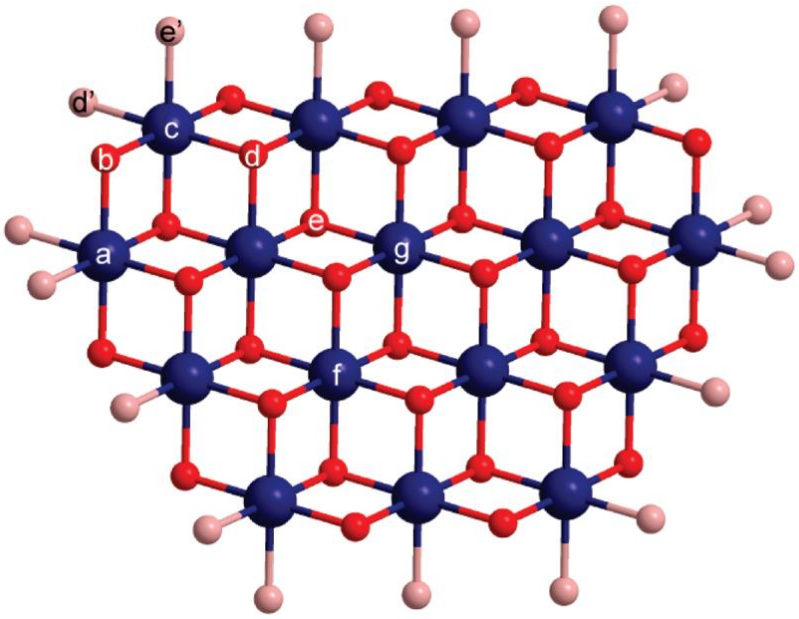

Figure 1.6.g Edge-sharing molecular cobaltate cluster model for bulk CoPi. Bridging oxo/hydroxo ligands are shown in red, nonbridging oxygen ligands (including water, hydroxide, and phosphate) complete the octahedral coordination geometry of each peripheral Co ion (blue) and are shown in light red. Figure adapted from (Kanan *et al.* 2010), the labeled alphabets are for the analysis of the atom-atom distance, and is not important to this text.

In the voltammogram of Co^{2+} in phosphate buffer, the prefeature before the anodic onset peak was assigned to a $Co^{II/III}$ redox couple (Surendranath *et al.* 2009,

Surendranath *et al.* 2010), leading one to believe the cobalt oxidation state to be III or higher during turnover. This speculation was confirmed by electron paramagnetic resonance detection of a Co(IV) signal in frozen CoPi film (McAlpin *et al.* 2010) and by *in situ* X-ray absorption near edge structure spectroscopy during turnover condition (Kanan *et al.* 2010). Surendranath and coworkers proposed that a swift, proton-coupled electron-transfer equilibrium between Co^{III}-OH and Co^{IV}-O was followed by a rate-limiting chemical process involving oxygen-oxygen bond formation (Figure 1.6.h) (Surendranath *et al.* 2010).

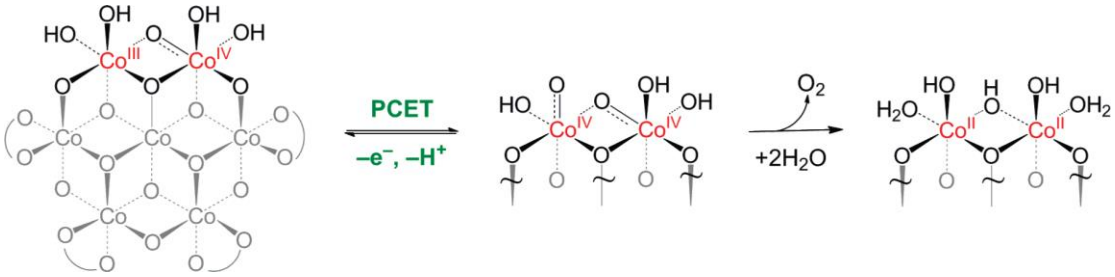

Figure 1.6.h. Proposed pathway for oxygen evolving by CoPi. A PCET equilibrium proceeded by a turnover-limiting O-O bond forming step is consistent with current dependencies on proton and electron equivalencies. Curved lines denote phosphate, or OH_x terminal or bridging ligands. Figure adapted from (Surendranath *et al.* 2010).

1.6.5 NiBi WOC

Nocera and coworkers reported a nickel-borate based water oxidation catalyst (NiBi) that functions in borate buffer at pH 9.2 (Dinca *et al.* 2010). In this report, when a glassy carbon electrode is immersed in a 0.1 M borate electrolyte solution containing 1 mM of Ni^{2+}, cyclic voltammograms (Figure 1.6.i) show the onset of a catalytic wave at 1.2 V vs normal hydrogen electrode (NHE). The production of O_2 during bulk electrolysis was confirmed by a fluorescence-based O_2 sensor.

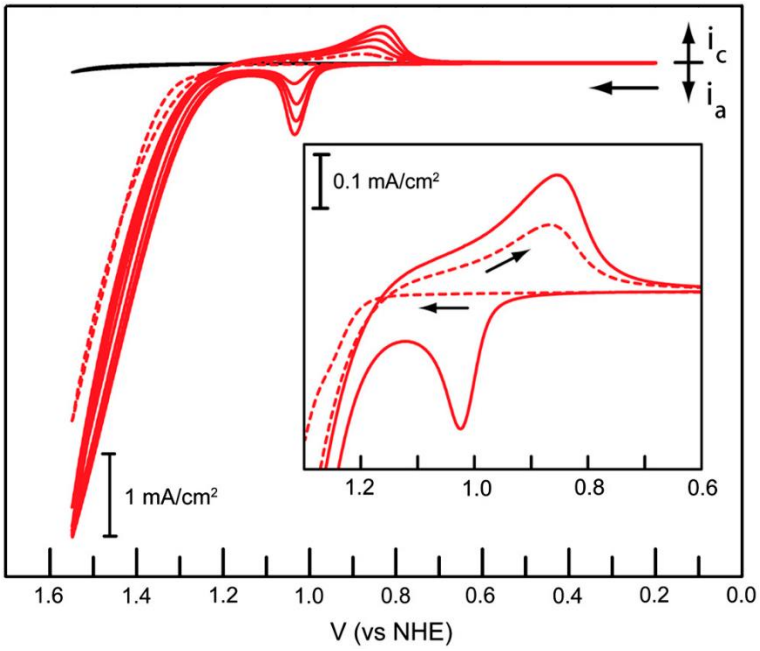

Figure 1.6.i CV of NiBi. CVs using a glassy carbon working electrode, 50 mV/s scan rate, of aqueous 1 mM Ni^{2+} in 0.1 M Bi electrolyte, pH 9.2. Successive scans show an increase of the anodic peak current for the redox event centered at ~1.0 e. (Inset) First (- - -) and second (—) CV scans using a glassy carbon working electrode, 50 mV/s scan rate, of aqueous 1 mM Ni^{2+} solutions in 0.1 M Bi electrolyte, pH 9.2. CV trace in the absence of Ni^{2+} is shown as a black trace. Figure adapted from (Dinca *et al.* 2010).

CVs shown in Figure 1.6.i display a broad cathodic feature centered around 0.8 to 0.9 V, and starting from the second scan, an anodic feature emerges at 1.02 V (Figure 1.6.i insert). The increasing amplitude of the anodic and cathodic prefeatures indicates the growth of a surface-deposited species. Indeed, this surface-bound material is the active catalyst for water oxidation (Dinca *et al.* 2010). CV offers a means of generating this catalyst with the ability to control its thickness. However, it is worth mentioning that, in borate-free electrolyte at pH 9.2, neither film formation nor catalysis was observed. Actually, a CV of 1 mM Ni^{2+} solution in 0.1 M $NaNO_3$ at pH 9.2 is indistinguishable from the CV of electrolyte only without Ni^{2+} (Figure 1.6.j). Therefore, borate plays a key role in the formation of this nickel-containing WOC.

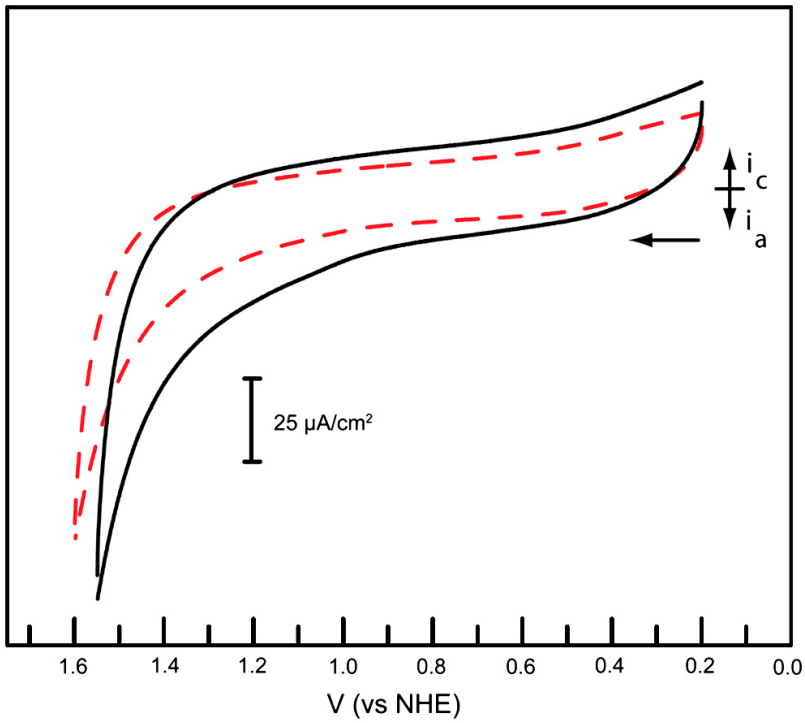

Figure 1.6.j CV of Ni(II) in solution contains no borate. CV taken with a glassy carbon electrode in a 0.1 M $NaNO_3$ solution (pH 9.2 adjusted with KOH) (—), and of a 1 mM Ni^{2+}/0.1 M$NaNO_3$ solution (pH 9.2) (red dashed line). No catalytic wave is observed in the absence of Bi. Figure and captions adapted from (Dinca *et al.* 2010).

Anodic activation of the low-potential electrodeposited film of Ni-Bi increased the catalytic activity by more than two orders of magnitude (Bediako *et al.* 2012). It was found that the current density of these anodized catalyst films decreases with increasing Bi concentration while [Bi] > 40 mM (Figure 1.6.k). The apparent antagonistic roles of borate in OEC was interpreted by the authors as that borate serves as "a promulgator of catalyst activity by enabling proton-coupled electron transfer (PCET) and as an inhibitor in its role as an adsorbate of active sites" (Bediako *et al.* 2013).

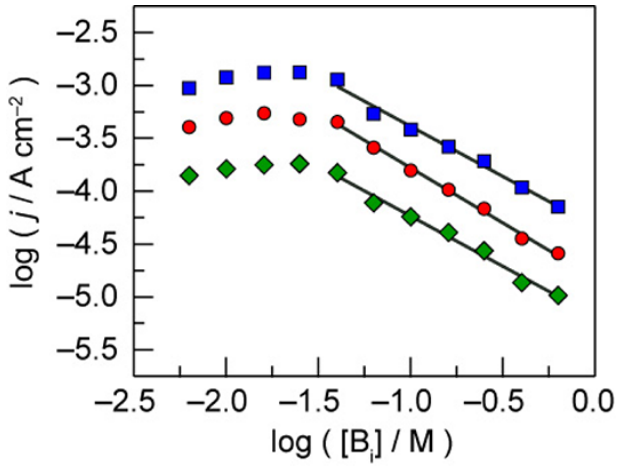

Figure 1.6.k Bi concentration dependence of steady state catalytic current density at constant potential (E = 1.04 V (green ◆), 1.05 V (red ●), 1.06 V (blue ■)) for an anodized catalyst film deposited onto a Pt RDE by passage of 1.0 mC cm−2 and operated in Bi electrolyte, pH 9.2. Sufficient KNO_3 was added to maintain a constant total ionic strength of 2 M in all electrolytes. Koutecký−Levich analysis was used to extract activation-controlled current densities in weakly buffered electrolyte, where the measured current was dependent on rotation rate. The experimental reaction orders (slopes of the red linear fits) in Bi are (from top to bottom) −0.95, −1.04, and −0.95. Figure and captions adapted from (Bediako *et al.* 2013).

The anodized NiBi catalyst films display Tafel slopes within the range of 28 and 32 mV/decade (Figure 1.6.l.a) at pH 8.5 to 12. Meanwhile, interpolation of Tafel plots at a fixed current density (Figure 1.6.l.b) shows that the potential required to sustain a current density decreases by 90 mV for every pH unit increased within the range of pH 8.5 and 12. Bediako and coworkers used the equation shown as 1.6.a:

$$\left(\frac{\partial E}{\partial \mathrm{pH}}\right)_j = -\left(\frac{\partial \log j}{\partial \mathrm{pH}}\right)_E \left(\frac{\partial E}{\partial \log j}\right)_{\mathrm{pH}} \qquad 1.6.a$$

Subsitituting the Tafel slope $\left(\frac{\partial E}{\partial \log j}\right)_{\mathrm{pH}}$ = 30 mV/decade (Figure 1.6.l.a) and $\left(\frac{\partial E}{\partial \mathrm{pH}}\right)_j$ = -90 mV/pH (Figure 1.6.l.b) into Equation 1.6.a yields $\left(\frac{\partial \log j}{\partial \mathrm{pH}}\right)_E$ = +3.

In other words, the catalytic rate is dependent on an inverse third order of the proton activity (Bediako *et al.* 2013).

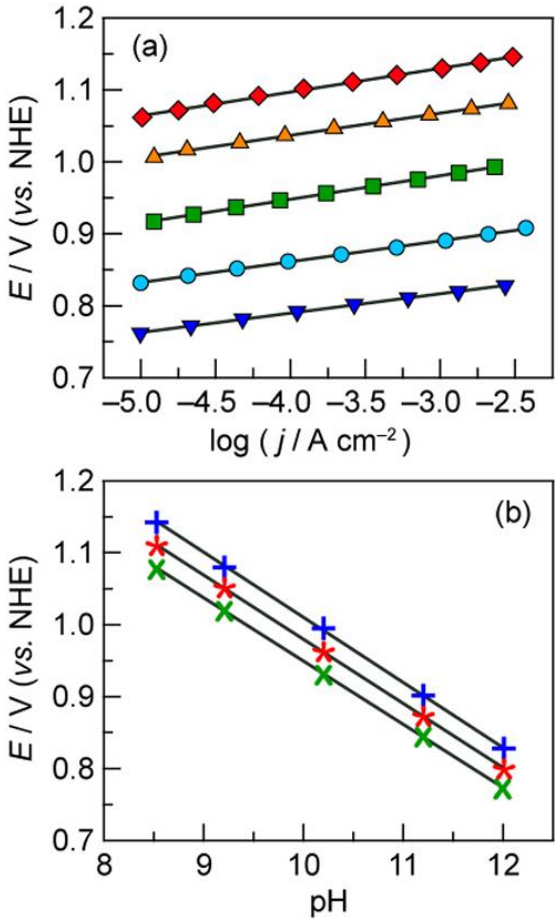

Figure 1.6.1 (a) Tafel plots, E = (E_{appl} − iR), for anodized NiBi catalyst films deposited on a Pt rotating disk electrode by passing 1.0 mC cm^{-2}, and operated in 0.60 M Bi pH 8.5 (red ◆), 0.20 M Bi pH 9.2 (orange ▲), 0.11 M Bi pH 10.2 (green ■), 0.10 M Bi pH 11.2 (light blue ●), and 0.10 M Bi pH 12.0 (dark blue ▼). Each electrolyte contained an additional 0.9 M KNO_3 as supporting electrolyte to maintain an ionic strength of about 1 M. Koutecký−Levich plots were constructed to extract activation-controlled current densities where necessary. (b) Interpolation of Tafel plots at 2.5 mA cm^{-2} (blue +), 0.25 mA cm^{-2} (red ∗), and 0.025 mA cm^{-2} (green ×). Slopes are −90, −89, and −88 mV/pH unit, respectively. Figure adapted from (Bediako *et al.* 2013).

At extremely high pH, the overpotential required for the anodized NiBi film to sustain a 10 μA/cm^2 current density was found to show an inflection point at pH 12.2

(Figure 1.6.m). This led the authors to conclude that one of the three kinetically relevant protons in the NiBi catalyst active sites possesses a pK_a of 12.2.

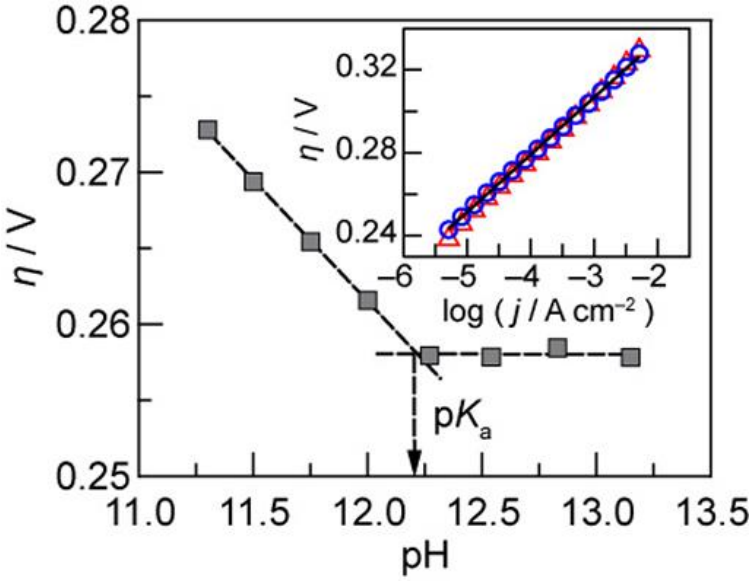

Figure 1.6.m Plot of the pH dependence of steady state electrode overpotential (gray ■), at constant current density (j_{anodic} = 10 > μA cm^{-2}) for an anodized 1.0 mC cm^{-2} catalyst film deposited onto FTO and operated in 0.1 M Bi 2 M KNO_3 electrolyte. The change in slope at pH 12.2 is consistent with the elevation of the bulk pH above the pK_a of an active site moiety. The inset shows Tafel plots, = (E – iR − E°), for anodized catalyst films deposited onto a Pt RDE by passage of 1.0 mC cm^{-2} and operated at 2000 rpm in 0.1 M KOH 1.9 M KNO_3 pH 12.9 (blue ○) and 1.0 M KOH 1.0 M KNO_3 pH 13.8 (red△) electrolyte. Tafel slopes are 28 and 30 mV/decade, respectively. Figure adapted from (Bediako *et al.* 2013).

Based on afore mentioned information, Bediako and coworkers proposed a mechanism for this NiBi WOC. At pH 8.5 to 14, with total [Bi] > 20 mM, the active sites bind with borate anion reversibly, and the borate-free active sites go on with an overall three-proton two-electron equilibrium followed by a rate-limiting chemical process summarized in Figure 1.6.n

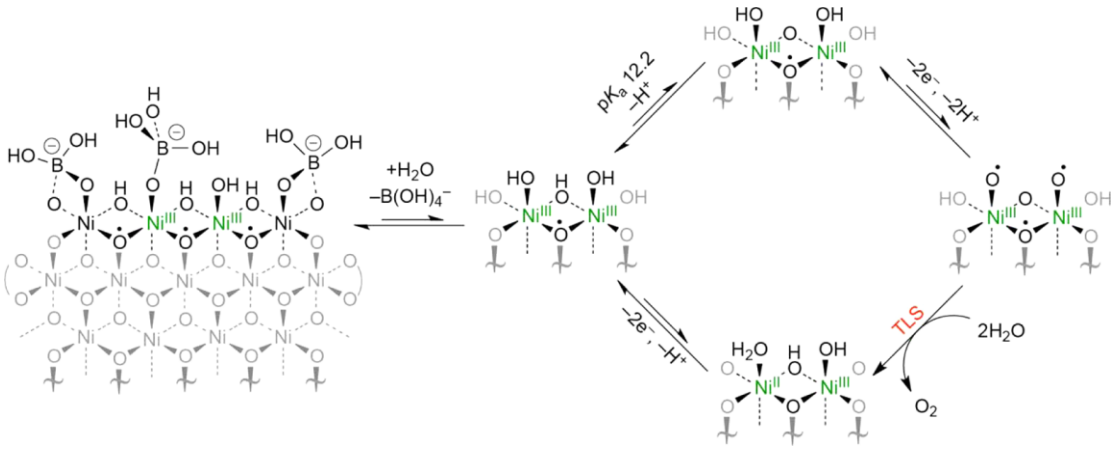

Figure 1.6.n. Proposed pathway for O_2 evolution by NiBi in Bi ($[B(OH)_4^-] > 20$ mM) electrolyte, pH 8.5−14. The reversible dissociation of borate anion and an overall two-electron, three-proton equilibrium followed by a rate limiting chemical step is consistent with the experimental electrochemical rate law. A μ-OH site possessing a pKa of 12.2 is fully deprotonated in the resting state under highly alkaline conditions. Oxidation state assignments are approximate; oxidizing equivalents are likely extracted from orbitals with predominantly O 2p character, particularly for the pre-TLS (turnover limiting step) intermediate. Figure adapted from (Bediako *et al.* 2013).

1.7 Techniques

1.7.1 Solid Phase Peptide Synthesis (SPPS)

1.7.1.1 Overview

A peptide is a sequence of amino acids and its chemical synthesis involves a series of repeated steps. Initially, the synthesis took place in solution phase, which was hindered by the solubility of intermediates and the product (Amblard *et al.* 2006). In general, solution-phase peptide synthesis is labor intensive especially for long sequences.

The most powerful peptide synthesis strategy was developed by Bruce Merrifield (Merrifield 1963) and is known as solid phase peptide synthesis (SPPS). Demonstrated in Figure 1.7.a, in SPPS, the first amino acid from the C-terminus of the intended sequence, protected on the N-terminus and side chain if necessary, is covalently linked to a solid resin, which is realized through an ester bond for peptide acids or an amide bond for

peptide amides. After the loading of the first amino acid to the resin, subsequent building of amino acids can be realized by a series of deprotections of the N-terminus and amino acid coupling reactions. Once the desired sequence has been synthesized, the peptide can be cleaved from the resin usually through acidolysis presenting the crude peptide, which could be purified by chromatographic methods.

In SPPS, a large excess of reagents at high concentration can be used to drive coupling reactions to completion. Unreacted reagents and soluble side products can be separated from the intermediate or product simply by filtration (Amblard *et al.* 2006). More importantly, SPPS enables the peptide synthesis to be fully automated.

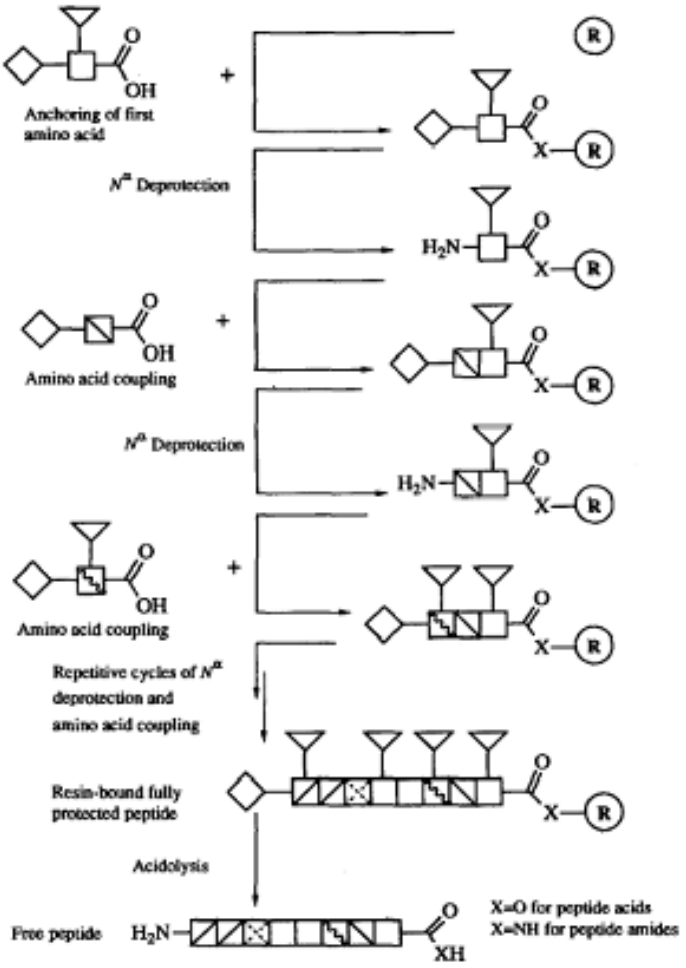

Figure 1.7.a Schematic representation of SPPS. Amino acids are represented by squares, the protected α-amino group by a diamond and the protected side-chain functional groups by triangles. The C-terminal of the peptide is bound to an insoluble solid support designated R for resin. Figure adapted from (Lloyd-Williams *et al.* 1993).

1.7.1.2 Microwave-assisted SPPS

Using microwaves to heat a reaction mixture to reduce the overall reaction time in SPPS was first reported in 1992 by Yu and coworkers (Yu *et al.* 1992) and has been integrated into commercially available automated peptide synthesizers (Ferguson 2003). Microwaves have been shown to shorten the reaction time and increase the synthesis quality but may induce some side reactions. Racemization of histidine and cysteine under

microwave-assisted SPPS is more severe but is overcome by relying on conventional synthesis during deprotection or coupling of His or Cys (Palasek *et al.* 2007). For sequences containing an Asp-AA moiety, where AA = Gly, Asn, Ser or Ala, aspartimide formation is a common side reaction (Martinez and Bodanszky 1978, Nicolás *et al.* 1989). Under microwave-assisted SPPS, replacing piperidine with piperazine as the deprotection reagent showed reduced levels of aspartimide formation (Palasek *et al.* 2007).

1.7.2 Circular Dichroism (CD) Spectroscopy

1.7.2.1 Introduction

A chiral molecule and its mirror image are not superimposable and they are known as enantiomers. A pair of enantiomers share identical physical and chemical properties but for two exceptions: the way they interact with polarized light and the way they interact with other chiral molecules (Brown *et al.* 2013). A chiral molecule absorbs left-handed polarized light (LCPL) and right-handed polarized light (RCPL) differently (Equation 1.7.a), and this phenomena is denoted as circular dichroism (CD).

$$\Delta A(\lambda) = A(\lambda)_{LCPL} - A(\lambda)_{RCPL} \qquad 1.7.a$$

where λ is the wavelength of the light.

1.7.2.2 Protein secondary structure probed by CD

Amino acids are the building blocks of proteins and peptides. Since 19 naturally-occuring amino acids have a chiral center, it is not surprising that proteins show CD spectra. The protein CD spectra in the region of 180-250 nm are dependent on protein secondary structure, with characteristic spectra for α-helix, β-sheet, β-turn and poly-L-proline II (P2) (Figure 1.7.b) (Greenfield 1996).

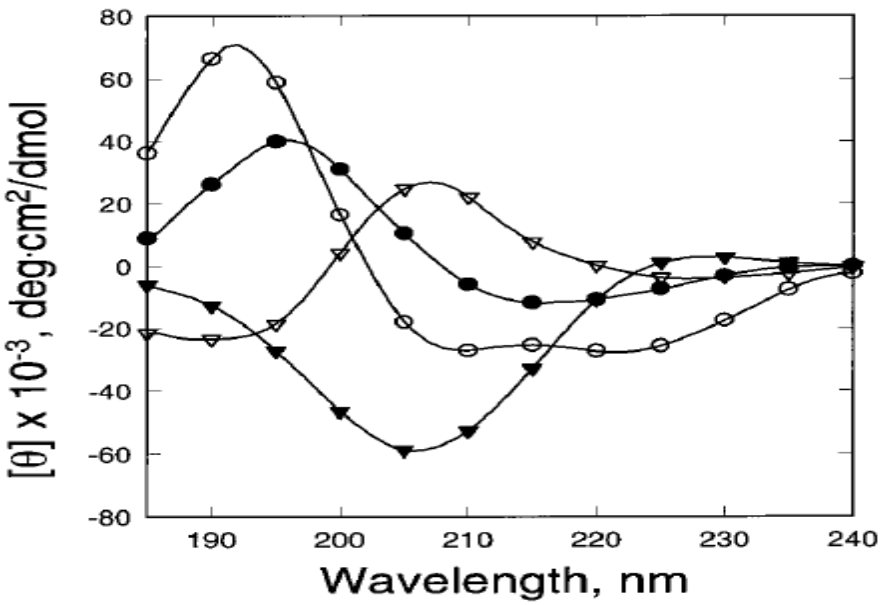

Figure 1.7.b. CD spectra of typical protein secondary structures. Shown are polypeptides in the α-helical, β-sheet, β-turn, and P2 conformations. (empty circle) α-Helix, (filled circle) β- sheet, and (empty triangle) β-turn, and (filled triangle) P2 (poly-L-proline in 0.1 M acetic acid). Figure and captions adapted from (Greenfield 1996).

Indeed, one can predict the secondary structure composition of a protein based on its CD spectra (Yang *et al.* 1986). Considering the nondestructive nature of the CD measurement and the low requirement for the amount of protein needed, typically in the μg range (Greenfield 2006), CD is a convenient tool to probe protein structure. Changes in protein CD spectra are a hint of structural change of the protein. CD is a powerful tool to follow dynamic changes in protein structure. For example, structure changes induced by changing of pH, ligands, temperature or denaturing reagent could be followed using CD. Particularly, if the interaction between a protein and metal ion could induce a secondary change of the protein or binding to metal stabilized the protein secondary structure, this interaction could be probed using CD. Furthermore, metal ions while free in solution do not display any CD signal. However, once they bind to a protein, a chiral

molecule, a CD signal could emerge in the wavelength region where the metal ions have an electronic transition.

1.7.3 Electrochemistry

1.7.3.2 Cyclic Voltammetry (CV)

Cyclic Voltammetry (CV) is a commonly-used electrochemical measurement to probe the properties of the redox active species in solution or immobilized on an electrode surface. In a CV experiment, the potential of the working electrode is ramped from a defined starting potential in a linear fashion until a predefined final potential, then the potential is reversed at the same speed to the initial potential (potential profile shown in Figure 1.7.c), and meanwhile the current passing through the working electrode is recorded. The plot of the current *versus* potential is called a cyclic voltammogram.

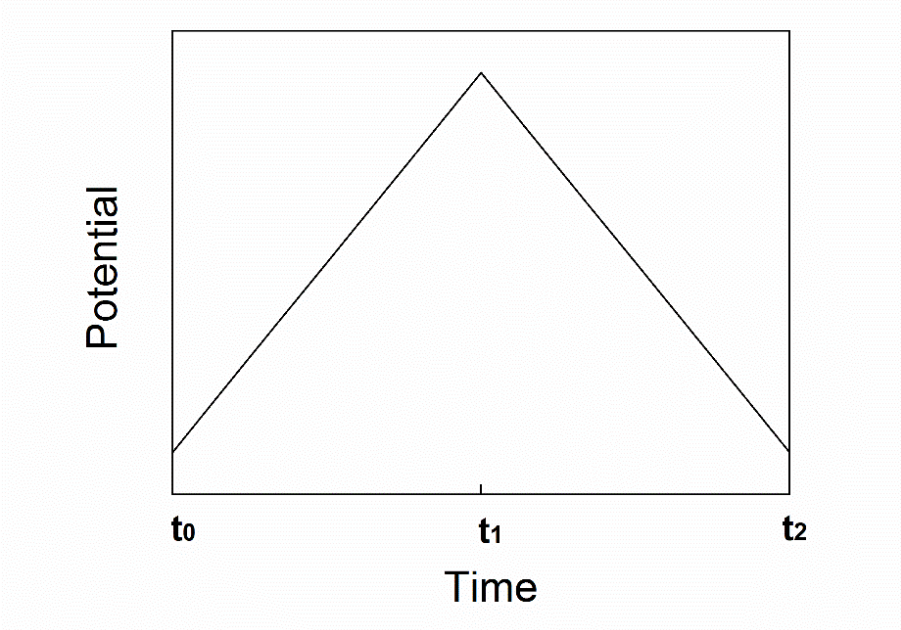

Figure 1.7.c. Potential waveform in cyclic voltammetry.

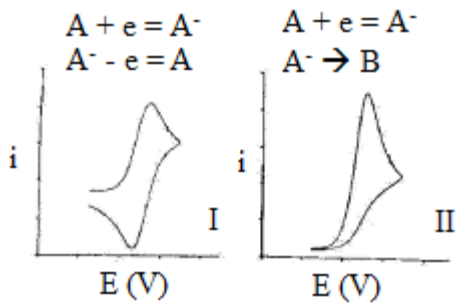

Figure 1.7.d CV of I) a reversible redox couple, II) an electron transfer followed by an irreversible chemical reaction leading to overall irreversible redox couple. Figure adapted from (Heinze 1984).

By analyzing the voltammogram, one can tell whether there are redox active species, and if yes, more information on whether the redox couple is reversible. If reversible, the mid-point potential of this pair could be determined through the relative CV peaks. If the CV (Figure 1.7.d.II) is not reversible, one possibility could be a chemical reaction following the redox reaction (Heinze 1984). By analyzing CV spectra, knowledge about the chemical reaction including catalysis could be gathered.

1.7.3.3 Controlled Potential Electrolysis (CPE)

Controlled Potential Electrolysis (CPE), also named bulk electrolysis, is an electrochemical method where a constant potential is applied on the working electrode to drive an electrochemical reaction to happen. CPE is commonly used in electrochemically synthesizing products or testing catalyst ability (Fry 1989, Nalwa 2001). Due to the intrinsic activation energy barrier, the potential used during the CPE is different from the thermodynamic potential, and the difference is termed the overpotential. More information on overpotentials is described in Chapter 1.4.3.

1.8 Challenges in transition metal - amino acid research

Much progress has been made in understanding the redox mechanisms of metalloproteins by studying both natural enzymes and *de novo* designed metalloproteins. Elucidating molecular mechanisms such as water oxidation in photosystem II (PSII) remains a challenge. To achieve full understanding of the water oxidation mechanism in PSII and potentially applying the principles learned to design an artificial system with even better performance, a more thorough understanding between transition metals and amino acids ligands must be developed.

Research in artificial water oxidation has been centered on catalysts involving precious metals such as Ru and Ir. The operating conditions are often harsh, for example requiring strongly acidic solutions, and the use of these materials is costly and not sustainable. In Chapter 2, the discovery and characterization of a water oxidation catalyst using the earth-abundant metal Ni will be presented. This Ni-catalyst forms while amino acids such as glycine are present, and works under benign conditions. It achieves a 1 mA/cm^2 current density with a modest overpotential at 475 mV at pH 11. In this chapter, I contributed to the experiment design and performed the experiments. Dr. Giovanna Ghirlanda contributed to the experiment design. Dr. James Allen designed and supervised the project.

Various *de novo* designed metalloproteins have been reported, however achieving *de novo* designed redox active metalloproteins has proven to be difficult. In Chapter 3, *de novo* designed copper binding peptides with active redox centers will be introduced. These peptides, whose sequences have been systematically designed, showed metal binding that is correlated with the stability constants of the Irving-Williams series for

divalent metal ions. In this chapter, I contributed to the design of the peptide sequences and designed and performed the experiments. Dr. Sandip Shinda trained me in synthesizing the peptides using microwave-assisted solid phase peptide synthesis. Dr. Marco Flores performed the electron paramagnetic resonance spectroscopy and fitted the data. Dr. Giovanna Ghirlanda contributed to the design of the experiments. Dr. James Allen designed and supervised the project. I used peptides synthesized and purified by myself, in the later part, I also used peptides ordered from GeneScript (New Jersey, USA).

CHAPTER 2

WATER OXIDATION BY A NICKEL-GLYCINE CATALYST

2.1 Introduction

While solar energy is an attractive option as a sustainable resource, the efficient conversion of solar energy into chemical fuels remains a challenge, with the natural diurnal cycle requiring a cost-effective, long-term storage mechanism (Lewis and Nocera 2006, Youngblood *et al.* 2009, Cook *et al.* 2010, Walter *et al.* 2010, Gust *et al.* 2012). One means for storage is using solar energy to generate hydrogen gas and molecular oxygen. However, current technologies are energetically inefficient due to the large overpotential associated with the electrolysis process. Consequently electrolytic water oxidation has a high energetic cost. Therefore, the development of efficient catalysts for the oxidation of water would greatly enhance the commercial viability of solar energy. In photosynthesis, water oxidation is performed by the Mn_4Ca cluster of the pigment-protein complex, photosystem II (Wydrzynski and Satoh 2005). The efficiency and reproducibility of the catalytic mechanism is achieved by the accumulation of four charge equivalents at the Mn_4Ca cluster in a mechanism that is coupled with the transfer of four protons until the oxidation of water can occur. Progress in synthesizing water-oxidation catalysts has been made through the use of transition metals that can undergo multiple oxidation/reduction states. Research has been centered largely on metals such as ruthenium or iridium, but the operating conditions are often harsh, for example requiring acidic solutions, and the use of such precious metals is costly and not sustainable (Lewis and Nocera 2006, Cao *et al.* 2012, Gust *et al.* 2012, Hong *et al.* 2012, Fukuzumi and Hong 2014).

However, the use of a tetraGly peptide with copper was shown to enhance the catalytic properties of copper under benign conditions (Zhang *et al.* 2013).

2.2 Results

To develop a low-cost, sustainable water oxidation catalyst, we have focused on the use of the earth-abundant metal nickel in the presence of amino acids. The electrochemical properties of Ni in the presence of glycine (Gly) were characterized by cyclic voltammetry (CV). In a 1 mM Ni(II) solution in the absence of Gly, the measured current was relatively featureless and remained below 20 μA as the applied potential was increased from 0.2 to 1.45 V (Figure 2.1a). However, the addition of Gly resulted in a significant increase in the current to a measured value of 300 μA at 1.33 V for 4 mM Gly, corresponding to a current density of 4.2 mA/cm^2 (Figure 2.1a, Figure 2.1b). With a fixed Ni:Gly molar ratio of 1:4, the amplitude of the current was directly proportional to the concentration of the catalyst up to 1 mM Ni(II) after which the current was independent of the concentration, showing that the CV response is due to the Ni-4Gly system (Figure 2.1c). The stoichiometry was also tested by addition of a tetraGly peptide to Ni, which yielded a maximum current of 100 μA at 1.33 V for a Ni:tetraGly molar ratio of 1:1 (Figure 2.1a). Thus, these data are consistent with a stoichiometry of four Gly for every Ni yielding the maximum response.

The well-defined 1:4 ratio of Ni to Gly suggests that substituents of Gly serve as metal ligands. When amino acids other than Gly were added, such as alanine and glutamine, the CV response had an enhanced current at 1.33 V, showing that the side chain does not play a critical role (Figure 2.1d). However, only small currents of less

than 40 μA were observed for other additives such as acetate, pyridine, and N-acetylglycine, which has an amide rather than the amine of Gly. Together, these results demonstrate the involvement of the amine of glycine as playing a crucial role in the catalysis.

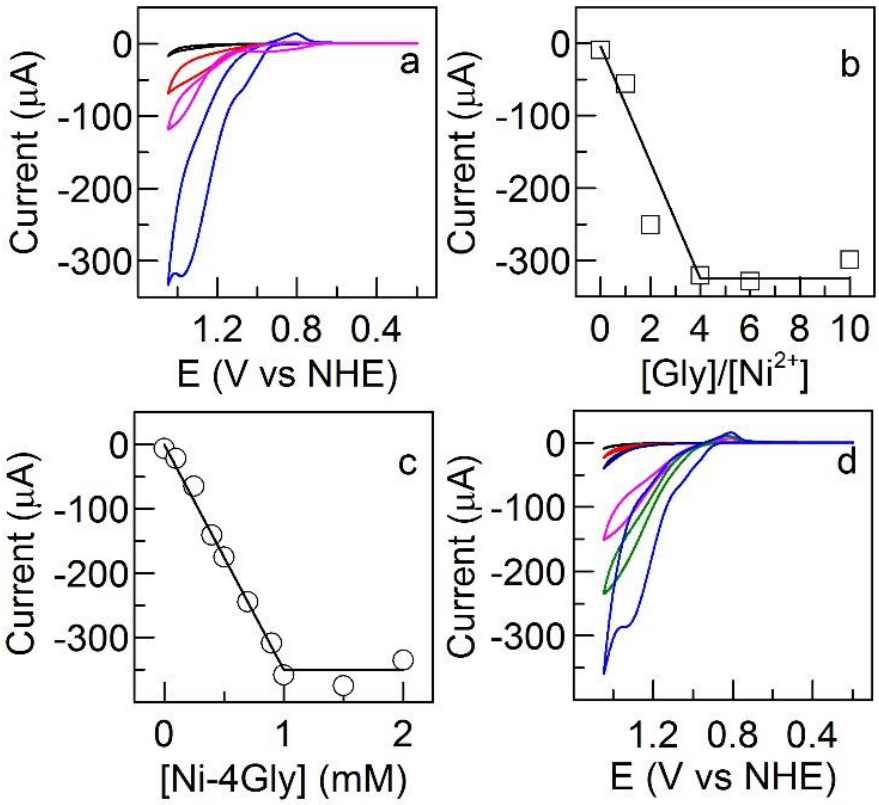

Figure 2.1. Electrochemical measurements of Ni(II) in a phosphate buffer at pH 11. (a) CVs measured using a glassy carbon working electrode with the potential swept from 0.20 to 1.45 V on a normal hydrogen scale (NHE). The CVs are relatively featureless with small currents for 1 mM Ni(II) alone (black), with an increase for 1 mM Gly (red) or 1 mM tetraGly peptide (pink), and a maximal current at a concentration of 4 mM Gly (blue). (b) The current for different amounts of Gly at 1 mM Ni at 1.38 V, showing a maximum at a 4:1 Gly:Ni ratio. (c) The current for different amounts of Ni-4Gly at 1.33 V, showing a maximum at a concentration of 1 mM Ni/4 mM Gly. (d) CVs have large currents for Ni(II) with amino acids, glycine (light blue), alanine (green) and glutamine (pink), and small currents for molecules with different substitutents, including acetate (black), pyridine (red), and N-acetylglycine (dark blue).

The catalytic enhancement of Ni with a tetraGly peptide is consistent with a previous report of water oxidation for Cu with a tetraGly peptide (Zhang *et al.* 2013). For tetraGly peptide, the N-terminal amine has been modeled as coordinating Cu(II) based upon infrared and electron paramagnetic resonance spectroscopies (Kim and Martell 1966, Nagy *et al.* 2003). Coordination by four in-plane nitrogen atoms, from one primary amine nitrogen and three amide nitrogens, and two out-of-plane oxygen atoms, from the carboxyl terminus and a bound water molecule, is found in the three-dimensional structure of Cu(II) bound to a tetraglycine peptide (Zhang *et al.* 2013). Coordination by the amines to Ni is also suggested by the presence of three nitrogen ligands to Ni(II) in the structure of bis(glycylglyconato)nickelate(II) (Freeman and Guss 1978). Thus, for Ni-4Gly, the metal is most likely coordinated by four amines. For catalysis, only one primary amine is required based upon the current enhancement for the tetraGly peptide with Ni (Figure 2.1a).

The evolution of molecular oxygen as a product of the catalytic reaction was monitored by measuring the concentration of dissolved oxygen using a fluorescence-based oxygen sensor under controlled potential electrolysis. For the Ni-4Gly system, the oxygen concentration was constant with no applied potential but the change to a 1.33 V potential resulted in an increase in the oxygen concentration (Figure 2.2). After a short delay, presumably due to the time required for diffusion of oxygen from the electrode to the sensor, the oxygen concentration is observed to undergo a rapid increase. Based upon the initial rate, a Faradaic efficiency of 60 ± 5% is obtained when averaging three independent measurements, assuming the release of one oxygen molecule for every four

electrons. These results demonstrate that the enhanced current at high potentials is associated with the production of molecular oxygen by the catalytic hydrolysis of water.

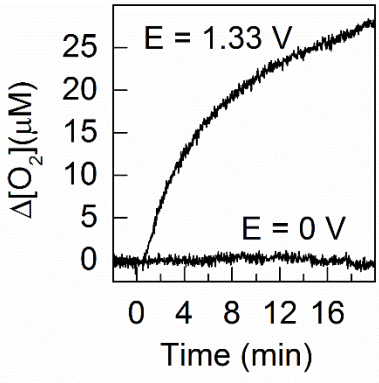

Figure 2.2. Time dependence of O_2 concentration showing oxygen production for a Ni-4Gly solution when the potential is poised at 1.33 V compared to no applied potential. The initial rate of 4 μM/min yields a Faradaic efficiency of 61%. The sample contained 1 mM Ni and 4 mM Gly in phosphate buffer at pH 11.

The voltammograms have both an oxidative and reductive peak (Figure 2.3a). The reductive peak is observed on the cathodic scan as a broad feature at 0.78 V that increases in amplitude upon multiple scans. The oxidative peak is not initially evident but builds during subsequent scans as a sharp prefeature near 0.90 V suggesting the formation of the catalyst on the electrode. To test this possibility, forty-five successive CV sweeps were performed in a solution containing both Ni and Gly (Figure 2.3a). Then, the glassy carbon electrode was removed from the solution, lightly rinsed, and placed into a solution containing only 250 mM sodium phosphate without Ni or Gly. The resulting CV showed nearly the same current response as observed when the electrode was in the Ni-4Gly solution, with an enhanced current at 1.33 V of 170 μA (Figure 2.3b).

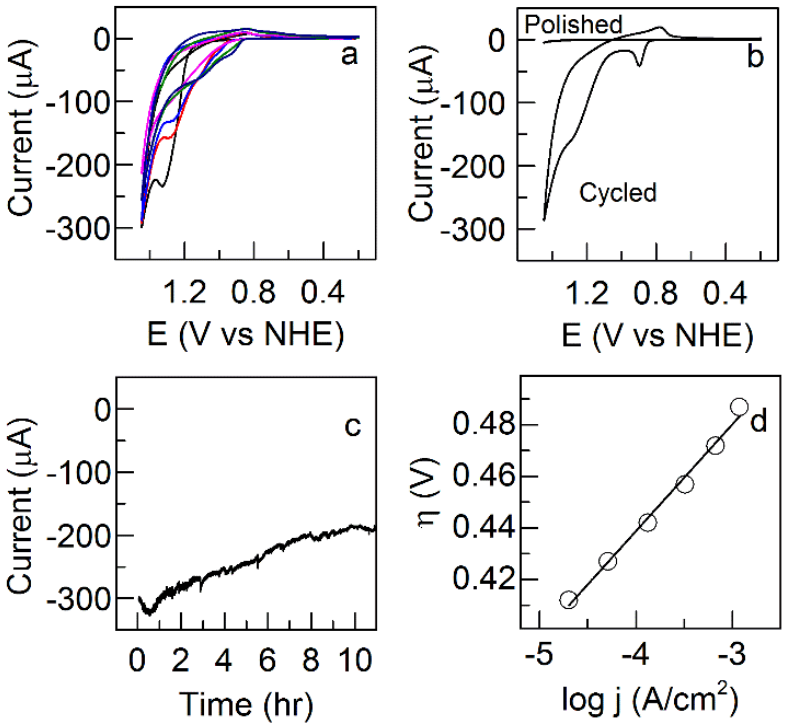

Figure 2.3. Electrochemical response of Ni-4Gly under different experimental conditions. (a) Forty-five consecutive scans were performed of an aqueous 1 mM Ni-4Gly solution in 250 mM phosphate buffer, pH 11, scan rate = 10 mV/s. (Cycle 1 (black), 2 (red), 3 (light blue), 15 (pink), 30 (green) and 45 (dark blue)). (b) After forty-five scans, a rinsed electrode in buffer alone shows the same features as seen in the Ni-4Gly solution; however no signals are present after polishing. (c) The measured current is very stable for 10 hours at a fixed applied potential of 1.33 V. (d) The overpotential, η, which is the applied potential minus the thermodynamic potential of 0.575 V for water at pH 11, has a linear dependence on the current density, *j*, with a fitted slope of 0.041 V/decade and overpotential of 0.480 V at 1 mA/cm^2 current density.

Both the oxidation and reduction peaks at 0.78 and 0.90 V are present in the initial sweep of the rinsed electrodes in contrast to the observation of increases for fresh electrodes in the Ni-4Gly solution. These results show that the CV features arise due to the formation of a Ni film on the carbon electrode. In solutions without Gly a film formed but at a much slower rate. When the electrode was prepared with forty-five sweeps and then placed into a fresh Ni-4Gly solution, the current was very stable upon subsequent sweeps. The catalytic species was electrochemically deposited on the electrode as a film

that is 0.7 μm thick after forty-five sweeps (Figure 2.5c). When the potential was fixed at 1.33 V, the catalytic conditions were found to be very stable for several hours, retaining at least 60% of the maximum value for over 10 hours (Figure 2.3c).

The measurement of a large and stable current indicates that water oxidation proceeds efficiently with a small overpotential, which is the applied potential minus the thermodynamic potential for water oxidation. The overpotential was determined by analysis of a Tafel plot that predicts a linear dependence of the overpotential on the current density. To minimize any contribution of forming the catalytic species, these measurements were performed using an electrode placed into buffer after forty-five sweeps in a Ni-4Gly solution. A linear correlation was observed yielding an overpotential of 0.475 ± 0.005 V at a current density of 10^{-3} A/cm^2 based upon three independent measurements (Figure 2.3d).

The CV scans of the Ni-4Gly film in pH 11 phosphate buffer without Ni or Gly show pronounced changes as the pH was altered (Figure 2.4a). The amplitude of the CV current of 1mM Ni-4Gly at 250 mM phosphate buffer was negligible below pH 9 and significantly increased above pH 9 (Figure 2.4b). The oxidation/reduction peaks near 0.78 and 0.90 V, at pH 11, are typical for Ni-oxide films and assigned to a one-electron, one-proton, oxidation/reduction couple, such as Ni(II)$(OH)_2$/ Ni(III)O(OH) (Doyle *et al.* 2013). The position of the anodic peak was found to systematically shift to higher potentials as the pH decreased (Figure 2.4a, Figure 2.4c). A fit of the pH dependence for three independent measurements yielded a slope of -0.13 ± 0.01 V per pH, corresponding to the involvement of two protons.

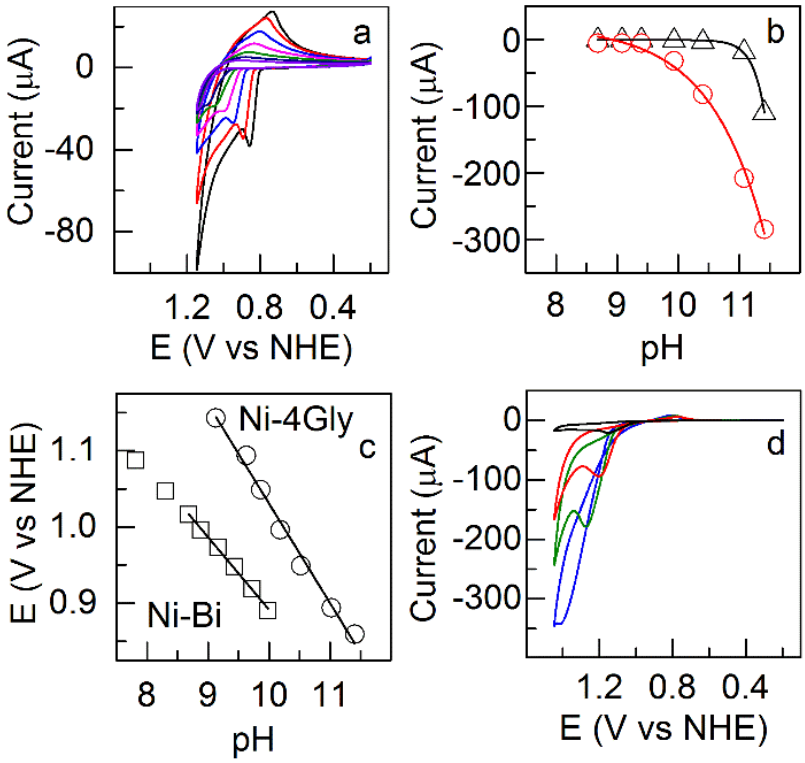

Figure 2.4. The pH dependence of the oxidation/reduction features. (a) The CV features of a Ni-4Gly film in 250 mM phosphate buffer without Ni or Gly shift to higher potentials as the pH is decreased (pH 11.40 (black), 11.02 (red), 10.52 (light blue), 10.18 (pink), 9.86 (green), 9.63 (dark blue), 9.13 (violet)). (b) pH dependence of the amplitude of the CV current of 1mM Ni-4Gly in 250 mM phosphate buffer at an applied voltage of 1.33 V (red circles) and 1.15 V (black triangles); the lines are added for guiding the eye only. (c) The pH dependence of the position of the anodic prefeature (full voltammogram shown in Figure 4a) (open circles) has a linear dependence on pH, with a best fit of -0.13 V/pH, compared to the dependence of -0.096 V/pH observed for Ni-borate (open squares) (Dinca *et al*, 2010). (d) Dependence of the CV on the concentration of phosphate, 0 mM (black), 50 mM (red), 100 mM (green), and 250 mM (blue), at fixed ionic strength for 1 mM Ni and 4 mM Gly.

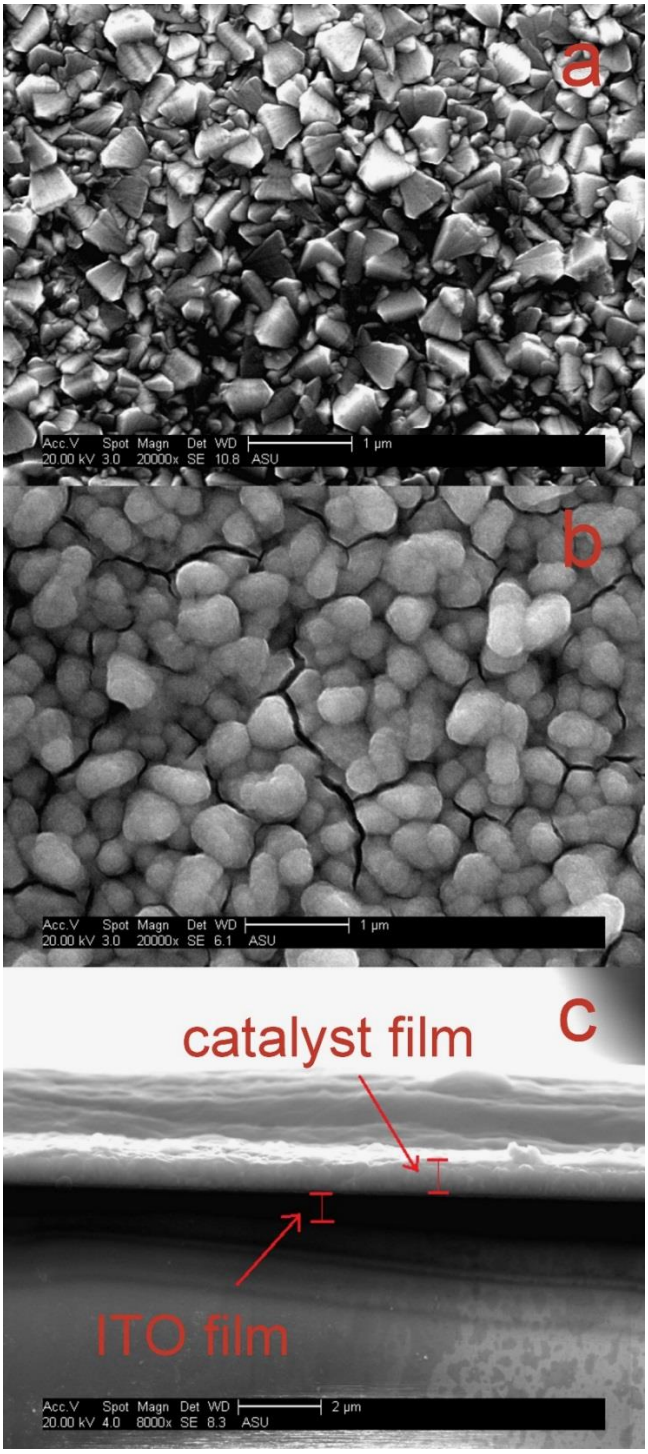

Figure 2.5. Images obtained using scanning electron microscopy. Shown are a) the ITO surface; b) the electrodeposited Ni catalyst film with the size of nanoparticles ranging from 200-700 nm; c) the edge of the catalytic film coated ITO electrode showing the cross section of the catalyst film with a thickness of approximately 700 nm. Image magnification is 20,000 (a and b) and 8,000 (c).

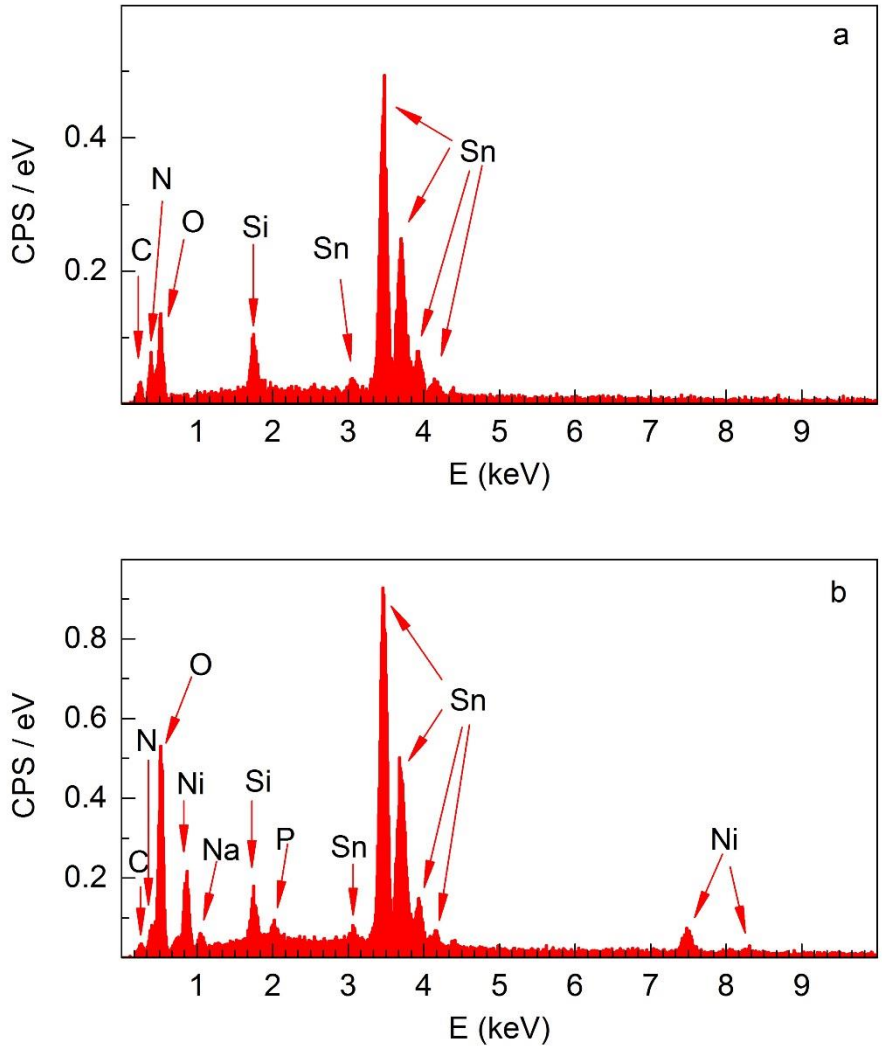

Figure 2.6. Energy-dispersive X-ray spectroscopy histograms. Shown are a) the ITO electrode and b) the catalytic film. The peaks are assigned for the ITO surface as 0.25 keV (C); 0.39 keV (N); 0.52 keV (O); 1.75 keV (Si); 3.03 keV, 3.48 keV, 3.70 keV, 3.92 keV, and 4.17 keV (Sn) and the assigned peaks for the catalytic film are 0.26 keV (C); 0.40 keV (N); 0.52 keV (O); 0.87 keV, 7.48 keV and 8.31 keV (Ni); 1.05 keV (Na); 1.76 keV (Si); 2.01 keV (P); 3.05 keV, 3.46 keV, 3.68 keV, 3.93 keV and 4.17 keV (Sn). The amplitudes are the counts per second (CPS) per eV.

The most likely catalytic mechanism for the Ni-4Gly system involves the generation of metal oxides in higher oxidation states, as has been found for other transition metals that facilitate water oxidation, such as copper, ruthenium, and iridium (Lewis and Nocera 2006, Crabtree 2012, Artero and Fontecave 2013, Doyle *et al.* 2013).

Energy-dispersive X-ray analysis showed the presence of Ni, P, and Na as the elemental components in addition to C, N, and O (Figure 2.6). Using X-ray photoelectron spectroscopy, the film was identified as containing Ni(II)-OH and PO_4^{3-} (Figure 2.7). Based upon the proposed mechanisms for other metal oxides (Lewis and Nocera 2006, Cao *et al.* 2012), a probable scheme includes a Ni(II)- hydroxide species binding a water molecule, being oxidized to Ni(IV), followed by the release of molecular oxygen and recovery to the divalent state of Ni in a proton-coupled process. These proton-coupled mechanisms are consistent with a pH dependence for the catalytic response.

In addition to Gly, the solutions for the CV measurements include 250 mM sodium phosphate. To investigate the contribution of phosphate, the CV measurements were performed for varying concentrations of sodium phosphate while keeping the ionic strength constant with the appropriate substitution of sodium perchlorate (Figure 2.4d). Increasing the sodium phosphate concentration resulted in a current response increase until a maximum was reached for a phosphate concentration of 250 mM. Notably, in the absence of phosphate, no enhancement of the current above 1.3 V was observed, but the voltammogram showed both the oxidation and reduction peaks, indicating that the Ni oxidation and reduction reactions occur despite the lack of water oxidation. Thus, phosphate is required for water oxidation, most likely serving as a proton acceptor during catalysis.

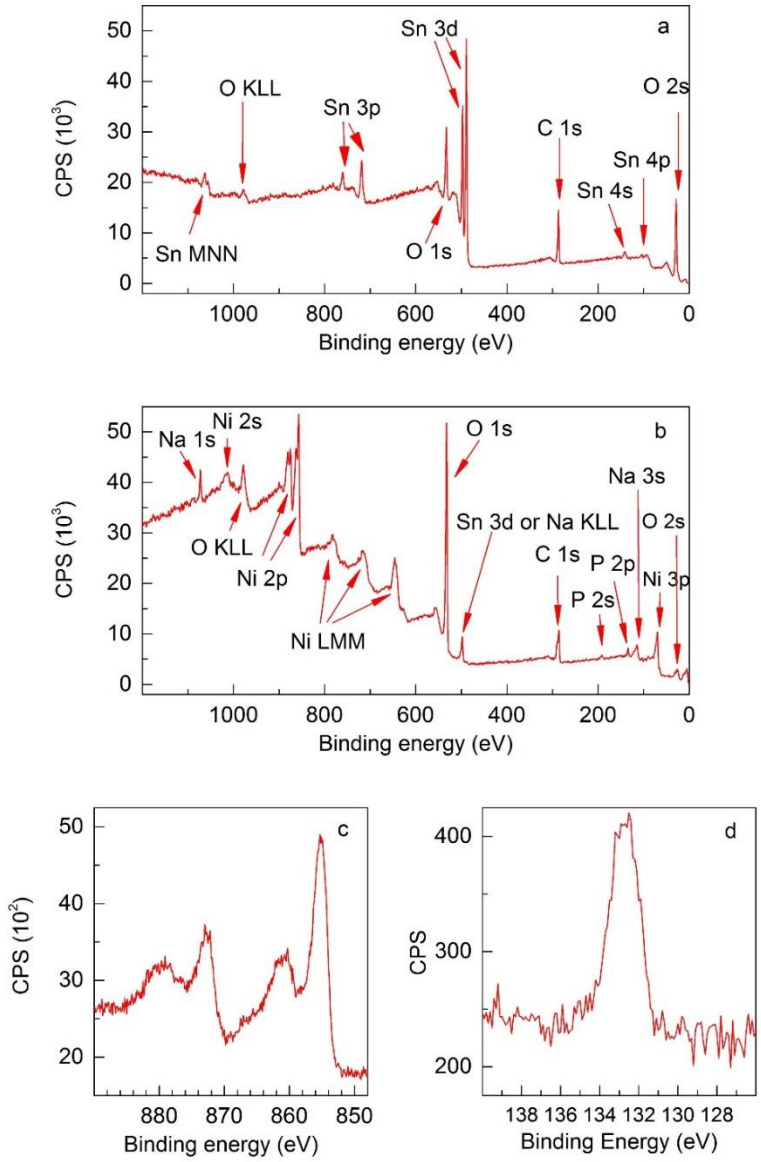

Figure 2.7. Spectra of the electrodeposited film on an ITO electrode measured using X-ray photoelectron spectroscopy. Shown are a) ITO electrode only, b) the Ni-film, c) the Ni-film centered on the Ni 2p peak showing features characteristic of $Ni(OH)_2$ (Biesinger *et al.* 2012), d) the Ni-film centered on the P 2p peak with a peak value characteristic of PO_4^{3-}. The peaks are assigned for the ITO electrode as 1062.0 eV (Sn MMN transition), 979 eV(O KLL), 760 eV and 718 eV (Sn 3p), 533 eV (O 1s), 497 eV and 489 eV (Sn 3d), 287 eV(C 1s), 141 eV (Sn 4s), 104 eV and 94 eV (Sn 4p) and 29 eV (O 2s or Sn 4d); and for the catalytic film as 1073 eV (Na 1s), 1014 eV (Ni 2s), 978 eV (O KLL), 881, 875, 862 and 857 eV (Ni 2p), 782, 715 and 646 eV (Ni LMM), 533 eV (O 1s), 498 eV (Sn 3d or Na KLL), 286 eV (C 1s), 192 eV (P 2s), 134 eV (P 2p), 115 eV (Na 3s), 70 eV (Ni 3p) and 26 eV(O 2s or Sn 4d). The amplitudes are the counts per second (CPS).

Previously, Ni has been shown to serve as a water-oxidation catalyst in the presence of borate (Dinca *et al.* 2010, Bediako *et al.* 2012, Bediako *et al.* 2013). Compared to the Ni-4Gly catalyst, Ni-borate shares some characteristics such as a modest overpotential of 0.425 V compared to 0.475 V for Ni-4Gly, and the evolution of the oxidation/reduction peaks due to the formation of a Ni-oxide film. Also, in both cases a proton acceptor, phosphate or borate, is required. However, Ni-borate has the clear differences of the oxidation/reduction peaks being at lower potentials with a weaker pH dependence of the peak position (Figure 2.4c), which has been interpreted as arising from a mechanism involving the coupled transfer of two electrons and three protons and the reversible dissociation of borate involving a dimer state of Ni (Dinca *et al.* 2010, Risch *et al.* 2011, Bediako *et al.* 2012, Bediako *et al.* 2013, Singh *et al.* 2013).

2.3 Discussion

Catalyst precursor, formation of catalyst and water oxidation

The catalyst reported here is a heterogeneous WOC, which is illustrated in Figure 2.3b and Figure 2.5. This heterogeneous WOC is derived from a homogeneous Ni-4Gly solution. Though it is premature to deny Ni-4Gly acting as a molecular WOC, this Ni-4Gly complex is unstable beyond onset potential of 1.0 V at pH 11 shown in Figure 2.1a. Consequently, a heterogeneous WOC is deposited onto the glassy carbon electrode. Therefore, Ni-4Gly is a catalyst precursor, which gets decomposed into active heterogeneous WOC in the presence of phosphate at pH 11 (Figure 2.4d). The current at the anodic peak region around 1.33 V has contributions from both the decomposition

process and water oxidation. This could at least partially account for the less than unity Faradic efficiency (Figure 2.2).

A primary amine is necessary but not sufficient

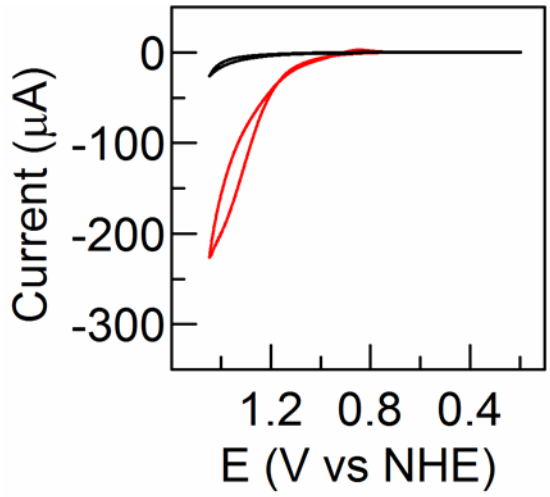

Figure 2.8. Cyclic voltammograms of 1 mM Ni(II) in a phosphate buffer at pH 11, in the presence of 4 mM methylamine (black) or 4 mM Tris (red). CVs measured using a glassy carbon working electrode with the potential swept from 0.20 to 1.45 V at a scan rate of 10 mV/s. All potentials were converted to normal hydrogen scale (NHE).

In Figure 2.1d, the anodic peak current values for additives as acetate, pyridine, and N-acetylglycine are all below 40 uA at 1.33 V, suggesting these additives are unable to produce active Ni-containing WOC. These additives are all lack of primary amine group, however, in the other hand, additives as glycine, alanine, and glutamine, which all have primary amine, are able to generate more than 100 uA current at 1.33 V (Figure 2.1d). Data shown in Figure 2.1d suggests that the primary amine is necessary and the carboxylate group is not sufficient for the formation of Ni-containing WOC. However, data in Figure 2.1d does not prove the sufficiency of primary amine or rule out the

necessity of carboxylate in producing Ni-containing WOC. Indeed, the primary amine itself is not sufficient, because methylamine, a direct analog to glycine that retains the primary amine but has the carboxylate group replaced by a hydrogen atom, proves to be incapable of inducing the formation of Ni-containing WOC (Figure 2.8). Tris(hydroxymethyl)aminomethane (Tris), which has a primary amine group, and does not have any carboxylate group but does contain alcohol groups, turns out to be an effective additive to generate this Ni-containing WOC (Figure 2.8). These information deserves more attention, and more detailed screening can lead to the discovery of the true identity of the pre-catalyst and the formation process of the Ni-containing WOC.

Molar ratio between glycine and Ni^{2+} in a molecular complex

According to the data in Figure 2.1b, the molar ratio between glycine and Ni^{2+} was tentatively assigned 4 : 1. However, this does not necessarily reflect the number of glycine coordinated to Ni^{2+} in a molecular complex. Glycine, Ni^{2+} and Ni-$(Gly)_n$, where n could be natural numbers ranging from 1 to 4, are in equilibrium in solution shown in Equation 2.1.

$$Ni^{2+} + Gly \rightleftarrows Ni\text{-}Gly$$

$$Ni\text{-}Gly + Gly \rightleftarrows Ni\text{-}2Gly$$

$$Ni\text{-}2Gly + Gly \rightleftarrows Ni\text{-}3Gly$$

$$Ni\text{-}3Gly + Gly \rightleftarrows Ni\text{-}4Gly \qquad 2.1$$

Based on different equilibrium constant, the most probably species can be Ni-4Gly, Ni-3Gly, Ni-2Gly or even Ni-Gly. Resolving the three dimension structure using crystals

formed from this Ni-4Gly solution can be the most direct approach to elucidate the true molar ratio between glycine and Ni^{2+} in a molecular complex.

Solubility and WOC formation

Ni^{2+} salt does not dissolve well in 250 mM phosphate buffer at pH 11, indeed 1 mM $NiSO_4$ results in a light green precipitation in the afore mentioned buffer. In contrast, mixing 1 mM $NiSO_4$ and 4 mM glycine or alanine or glutamine or Tris results in clear solutions which do not yield visible precipitation when the mixtures are subjected to centrifugation at 13k rpm, room temperature for 5 mins. These effective additives essentially stabilize the Ni^{2+} in this solution, and this stabilization presumably is realized by formation of molecular complexes between Ni^{2+} and additives. Imidazole, histidine and HHH peptide (a peptide introduced in Chapter 3 of this dissertation) can each form stable solution with 1mM Ni^{2+} in 250 mM phosphate buffer at pH 11. Nevertheless, cyclic voltammetry experiments revealed that none of imidazole, histidine or HHH peptide was able to form Ni-containing WOC. Therefore, the ability to increase the solubility of Ni^{2+} in solution is only necessary but not sufficient to induce the formation of Ni-containing WOC.

Metals other than Ni

In 250 mM phosphate, pH 11 buffer, glycine not only can form effective water oxidation catalyst precursor with Ni^{2+}, it can also form effective water oxidation catalyst precursor with other first-row transition metals. In addition to Ni^{2+}, Cu^{2+} and Co^{2+} also showed enhanced anodic peak current in the presence of glycine, but not Mn^{2+} (Figure

2.9). With or without Gly, Co^{2+} showed anodic peak currents of more than 100 μA, and this is in agreement with previous report of the CoPi catalyst (Kanan and Nocera 2008). For the case of Cu^{2+}, the addition of 4 mM Gly resulted in the increase of anodic peak current to 250 μA from 20 μA in the absence of Gly.

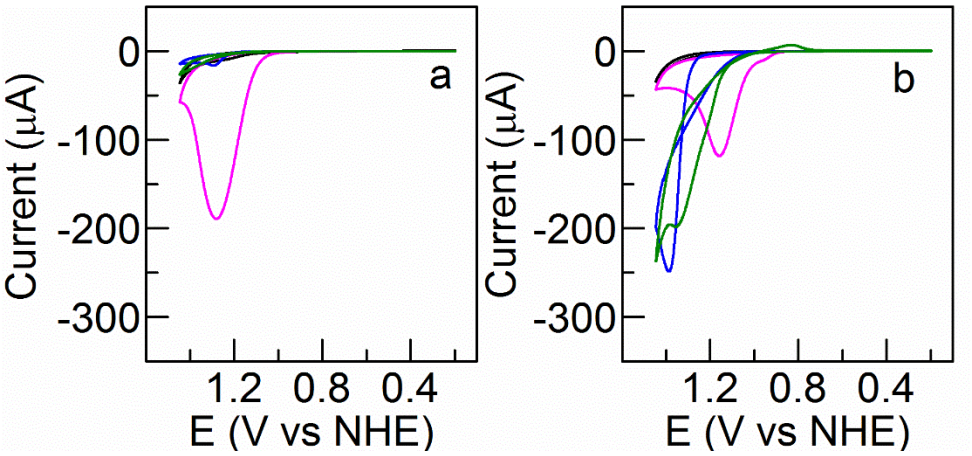

Figure 2.9 Cyclic voltmmograms of metal ions in the absence (a) or presence (b) of 4 mM Gly in a phosphate buffer at pH 11. Mn^{2+} (black), Co^{2+} (pink), Cu^{2+} (blue) and Ni^{2+} (green). The metal ions were all given at 1 mM, and all resulted in precipitation in the absence of Gly, thus supernatants were used. In the presence of 4 mM Gly, Cu^{2+} and Ni^{2+} yielded clear solution respectively, and for Co^{2+} and Mn^{2+}, the supernatants were used. CVs measured using a glassy carbon working electrode with the potential swept from 0.20 to 1.45 V at a scan rate of 10 mV/s. All potentials were converted to normal hydrogen scale (NHE).

2.4 Material and methods

General Electrochemical Procedures

Electrochemical measurements were performed using a CHI600E electrochemical analyzer (CH Instruments), a VC-2 voltammetry cell (BASi) with a built-in Pt wire counter electrode in the Teflon cap, a Ag/AgCl reference electrode (BASi), and a glassy carbon (BASi) working electrode. The measurements were performed using a scanning rate of 10 mV/s. The glassy carbon disc electrode has an effective diameter of 3 mm, and

the surface area of the electrode is 0.071 cm^2. Prior to use, the working electrode was polished with 0.05 μm alumina particles for 60 s, rinsed in water, then sonicated in water for 30 s to remove debris. After sonication, the electrode was rinsed with water and methanol and then dried. And then the electrode was subjected to 30 continuous scans in the potential window used in subsequent CV scans but with a fast scan rate, 500 mV/s in solutions without Ni(II) or glycine. The experiments were performed without iR compensation. Traces shown in Figure 2.1a, 2.1d and 2.4d are the 3rd scan of three consecutive scans. All the potentials have been converted to the normal hydrogen electrode (NHE) scale using a 0.197 V correction.

Film Generation

Films were generated on either carbon or indium tin oxide (ITO) electrodes using a solution of 1 mM $NiSO_4$, 4 mM Gly, or 250 mM sodium phosphate pH 11. The electrode was continuously cycled between 0.20 and 1.45 V at a scan rate of 10 mV/s for 45 cycles. For the polished carbon electrode, a dark greenish-brown film could be seen on the surface of the electrode after the sweeps. For the ITO electrode, an area of 0.7 cm by 0.7 cm of the working electrode was immersed into the solution and a brown-black film could be seen on the surface of the electrode after the sweeps.

O_2 Measurement

The O_2 concentration in solution was monitored at 295 K using a micro-oxygen sensor and a multifrequency phase fluorometer (MFPF-100, Ocean Optics). After the film had been generated, the solution was deoxygenated by bubbling N_2 gas for 15 to 20

minutes until the O_2 partial pressure in the solution reached a steady state. The change in the oxygen concentration was corrected for a slight baseline change during measurement.

Scanning electron microscopy and energy-dispersive X-ray analysis

Images using scanning electron microscopy and spectra using energy-dispersive X-ray analysis were obtained with an FEI XL-30 Environmental microscope equipped with an EDAX Sapphire EDX system operating at 20 kV.

X-ray photoelectron spectroscopy

The X-ray photoelectron spectra were measured using a Kratos Axis Ultra 165 DLD Hybrid Photoelectron Spectrometer equipped with a monochromatized Al Kα X-ray anode, magnetic immersion lens, and a delay line electron detector. The base pressure of the vacuum system was maintained at 2×10^{-9} torr. Spectra were collected in constant analyzer energy mode using an X-ray power of 300 W, a 20 mA emission current, and a 15 kV acceleration voltage. Low resolution (survey) spectra were measured with a pass energy of 160 eV and localized Ni 2p and P 2p regions were measured at high resolution using a 20 eV pass energy.

Turnover frequency (TOF) and turnover number (TON)

The TOF and TON were calculated based upon the measured oxygen release, number of electrons, and estimated number of catalytic centers. The rate of oxygen production is 5×10^{-10} mole/s (Figure 2.2) in the 10 ml solution. Based upon the surface

area of 0.071 cm^2, the measured thickness of 0.7 microns (Figure 2.5c), and an estimated Ni-Ni distance of 2.8 x 10^{-10} m (Bediako *et al.* 2013), the number of catalytic centers is estimated to be 5 x 10^{-7} moles. Assuming that all centers are active, the TOF is estimated to be 10^{-3} s^{-1} and the TON has a value of 40 during the 11-hour time span (Figure 2.3c). A significantly larger TOF of 2.5 s^{-1} is estimated if the active centers are confined to the surface of the film.

2.5 Conclusion

In summary, our results demonstrate the utility of a Ni-4Gly catalyst for the oxidation of water. This system has a modest overpotential of 0.475 V, is stable for prolonged periods of at least 10 hours, and can achieve an activity of 4 mA/cm^2. This activity occurs under benign conditions in an aqueous solution using inexpensive materials. The catalysis of water oxidation is observed not only for Gly but also other amino acids and the tetraGly peptide providing the possibility of incorporating the catalyst into a peptide design that is attached to an electrode as part of a bio-inspired solar cell. The presence of primary amines and phosphate is key to the formation of the heterogeneous, catalytically-active Ni-hydroxide species, suggesting a new avenue for the development of water oxidation catalysis.

CHAPTER 3

FACTORS DETERMINING THE BINDING OF COPPER AND OTHER METALS TO PEPTIDES

3.1 Introduction

Metal-containing proteins are commonly found in nature because metal cofactors are versatile in facilitating oxidation/reduction (redox) reactions, such as photosynthesis, respiration, nitrogen fixation, and oxygen metabolism. Many different transition metals are present in proteins as redox active cofactors, e.g. copper, manganese, and iron. These metals are typically coordinated in the protein by amino acid side chains, such as His, Met, Cys, Glu, and Asp, although in some cases the coordinating ligands include backbone atoms, bound water, or non-protein components, as found for example with the cyanide ligands of hydrogenase (Holm *et al.* 1996, Waldron *et al.* 2009).

Despite a detailed understanding of the properties of metalloproteins containing copper and other divalent metal ions, the design of novel metal-binding sites in proteins or peptides has proven to be challenging (DeGrado *et al.* 1999, Koder and Dutton 2006, Mullins and Pecoraro 2008, Lu *et al.* 2009). Some designs have made use of unstructured peptides that become more ordered after binding metal cofactors (Kohn *et al.* 1998, Farrer and Pecoraro 2003, Touw *et al.* 2007). Another approach has been the use of four-helix bundles, as the interface between the helices provides a well-defined pocket for cofactor binding (Lombardi *et al.* 2000, Calhoun *et al.* 2005). These designs have been successful in the incorporation of iron, zinc, and manganese as dinuclear cofactors, and in some cases the metal cofactors were capable of catalyzing redox

reactions (Kaplan and DeGrado 2004, Faiella *et al.* 2009, Reig *et al.* 2012, Roy *et al.* 2012, Yu *et al.* 2013, Yu *et al.* 2014, Zastrow and Pecoraro 2014).

To help elucidate the principles required for building novel metal-binding sites in peptides and proteins, we have designed and characterized a series of peptides for which the possible coordinating amino acid residues were systematically altered. The starting point for the design was a published peptide that contained two metal-coordinating sites, with each site having three His residues that could serve as metal ligands (Rockcliffe *et al.* 2006). For two peptides, the three His residues were altered with carboxylates in each binding site, as Asp-His-Asp and His-Asp-His. For a third peptide, all three His residues were changed to Asn, whose side chains would not be expected to coordinate a metal ion. The ability of these peptides to bind different divalent metals throughout a range of pH values was characterized using circular dichroism (CD) spectroscopy. The redox activity of the bound metal ions was investigated using cyclic voltammetry (CV) and the electronic structure was probed using electron paramagnetic resonance (EPR) spectroscopy. The implications for the binding of metals to peptides and proteins are then discussed in terms of the Irving-Williams series, which is used to relate the observed metal binding parameters to the stability constants for different transition metals (Irving and Williams 1948, Johnson and Nelson 1995).

3.2 Results

Binding of Cu(II) to the peptides measured using CD

The binding of metals to the peptides was characterized using CD in the ultraviolet region from 200 to 260 nm and the visible region from 300 to 700 nm. The UV region signal is indicative of the secondary structure of the peptide and was used to detect structural changes of the peptide due to metal binding. Depending upon the metal coordination, peptides with bound transition metals may have features in the visible region of CD spectra due to transitions between orbitals associated with charge transfer between the metal and peptide ligands or metal d-d transitions. Thus, both the UV and visible regions of the CD spectrum can be used to monitor metal binding.

In the absence of Cu(II), the CD spectrum of the DHD peptide showed features typical of a random coil, namely a minimum at 200 nm and a broad positive band at 224 nm (Figure 3.1). At low pH, no changes to the spectrum were observed upon the addition of Cu(II). At high pH in the presence of Cu(II), the CD spectrum gained new distinctive features with the appearance of a positive band centered at 215 nm in the UV region and two broad bands centered at 327 and 589 nm in the visible region with the intensity increasing as the pH increased.

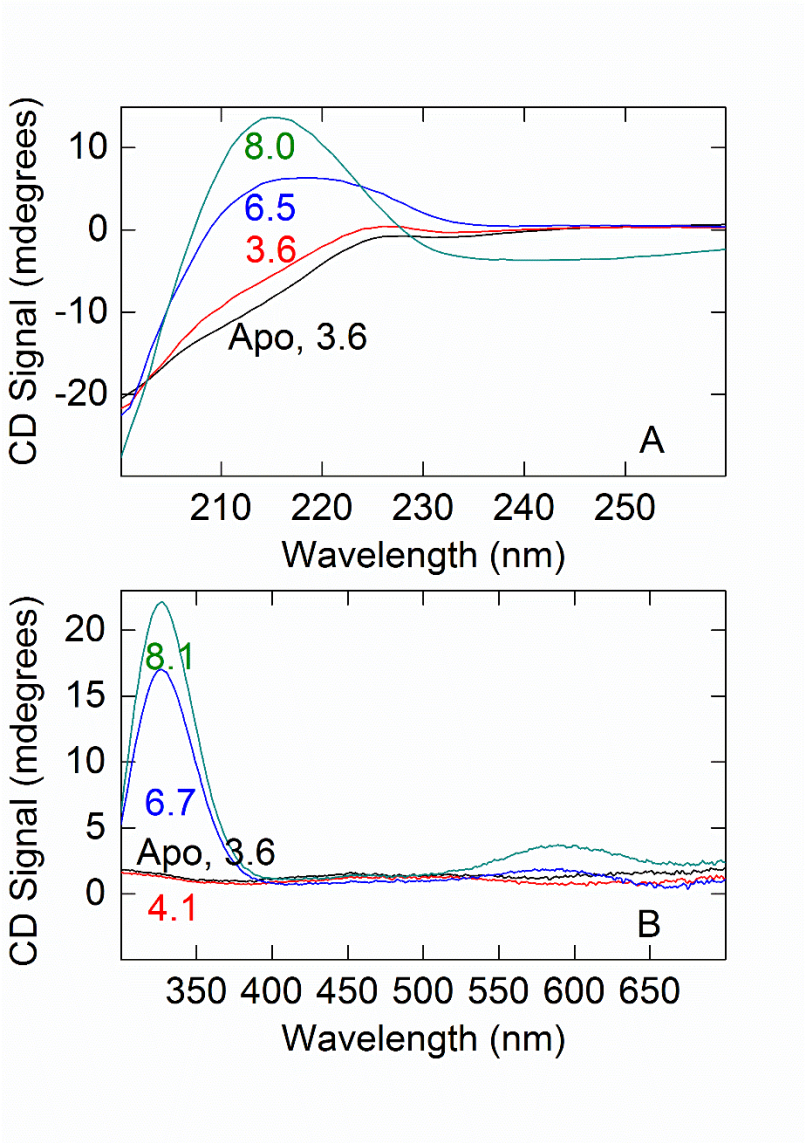

Figure 3.1 Binding of Cu(II) to the DHD peptide measured using CD spectroscopy. A) CD spectra were measured in the 200 to 260 nm region for the peptide in the absence of Cu(II) (black) and using a 2:1 Cu:peptide molar ratio for pH values of 3.6 (red), 6.5 (blue), and 8.0 (green). B) CD spectra were measured in the 300 to 700 nm region for the peptide in the absence of Cu(II) (black) and using a 2:1 Cu:peptide molar ratio for pH values of 4.1 (red), 6.7 (blue), and 8.1 (green).

In the presence of Cu(II), the CD spectra of the different peptides was measured at pH 8.0. For the HDH peptide at pH 8, the presence of Cu(II) resulted in a spectral profile similar to that of the DHD peptide, with a negative band below 205 nm and positive band

at 214 nm in the UV region, and positive bands at 325 and 564 nm in the visible region (Figure 3.2). The CD spectrum for the HHH peptide is similar to that previously published (Rockcliffe *et al.* 2006). When the Cu(II) concentration was systematically increased, the amplitude of the CD spectra reached a maximum value for two Cu(II) per peptide for the HHH, HDH and DHD peptides (data not shown). Below pH 8, the amplitudes of these spectra decreased, with no significant features observed below pH 4.0 (Figure 3.3). Increasing the pH above pH 5 resulted in larger amplitudes until the pH value was above 8. Fitting of these data to the Henderson-Hasselbalch equation (Equation 3.1, Page 95 of this dissertation) yielded pK_a values of 6.5, 6.6, and 6.8 for the HDH, DHD, and HHH peptides, respectively, indicating the involvement of His as one of the ligands.

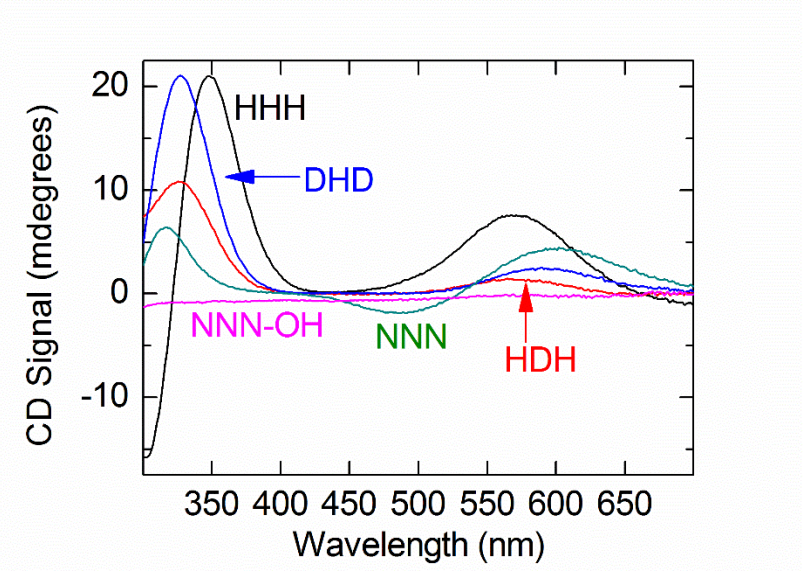

Figure 3.2. Binding of Cu(II) to different peptides measured using CD spectroscopy. CD spectra were measured in the 300 to 700 nm region for the peptides HHH (black), HDH (red), DHD (blue), and NNN (green) using a 2:1 metal:peptide molar ratio at pH 8.5.

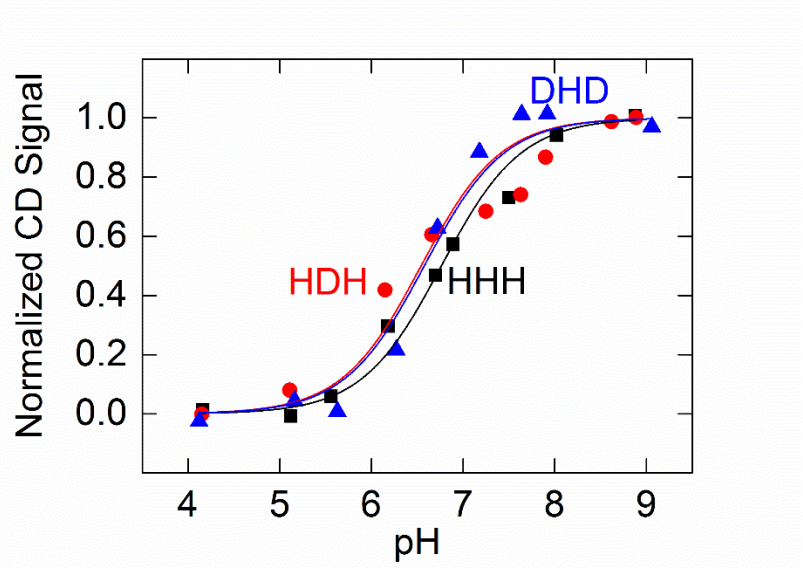

Figure 3.3. The pH dependence of the amplitude of the CD spectrum for the HHH (black), HDH (red), and DHD (blue) peptides. Shown are the changes in the amplitude of the CD spectra at each pH value, with the amplitude at low pH set to zero and at high pH normalized to one. The lines are best fits using the Henderson-Hasselbalch equation (Equation 3.1) with pK_a values of 6.5, 6.6, and 6.8 for the HDH, DHD, and HHH peptides, respectively. The CD amplitudes were measured at wavelengths of 325, 327 and 349 nm for the HDH, DHD, and HHH peptides, respectively.

Although the NNN peptide has Asn, instead of His or Asp residues that can coordinate metal ions, the CD spectrum showed Cu(II)-induced changes at pH values above 8, with positive peaks at 316 and 603 nm and a negative peak at 486 nm (Figure. 2). Given the lack of side chains that could coordinate the metal, a likely possibility was the involvement of the C-terminus region in the metal binding. To investigate the possible involvement of the C-terminus, a peptide was synthesized with a terminal carboxylate group instead of the amidated C-terminus, and is named NNN-OH. The CD spectrum of the NNN-OH peptide did not change in response to Cu(II) binding (Figure 3.2). Therefore, Cu(II) binding to the NNN peptide is primarily determined by interactions with the presence of the amidated C-terminus at pH 8.5.

Binding of different metals to the peptides

The ability of the peptides to bind the divalent metals Fe(II), Mn(II), Mg(II), Ca(II), Ni(II), Co(II), in addition to Cu(II), was investigated by measuring the CD spectra between 300 and 700 nm in the presence of the metal titrated up to a four-fold excess compared to the peptide concentration (Figure 3.4). Below pH 6.5, the CD spectra of the peptides in the presence of these metal was unchanged relative to the CD spectra of the peptides in the absence of added metal. Above pH 6.5, spectral differences were observed for Cu(II), Ni(II), and Co(II) but not for Fe(II), Mn(II), Mg(II), or Ca(II). At pH 9 in the presence of Ni(II), distinctive spectra were evident for the HHH, DHD, and HDH peptides with features that were very similar to each other with a positive maximum at 498 nm and a negative minimum at 423 nm. Similar features were observed for the NNN peptide but not the NNN-OH peptide, showing the involvement of the amidated C-terminus in the metal binding. In the presence of Co(II) at pH 9, a spectrum with positive features at 353 and 544 nm and a negative peak at 460 nm was seen only for the HHH peptide.

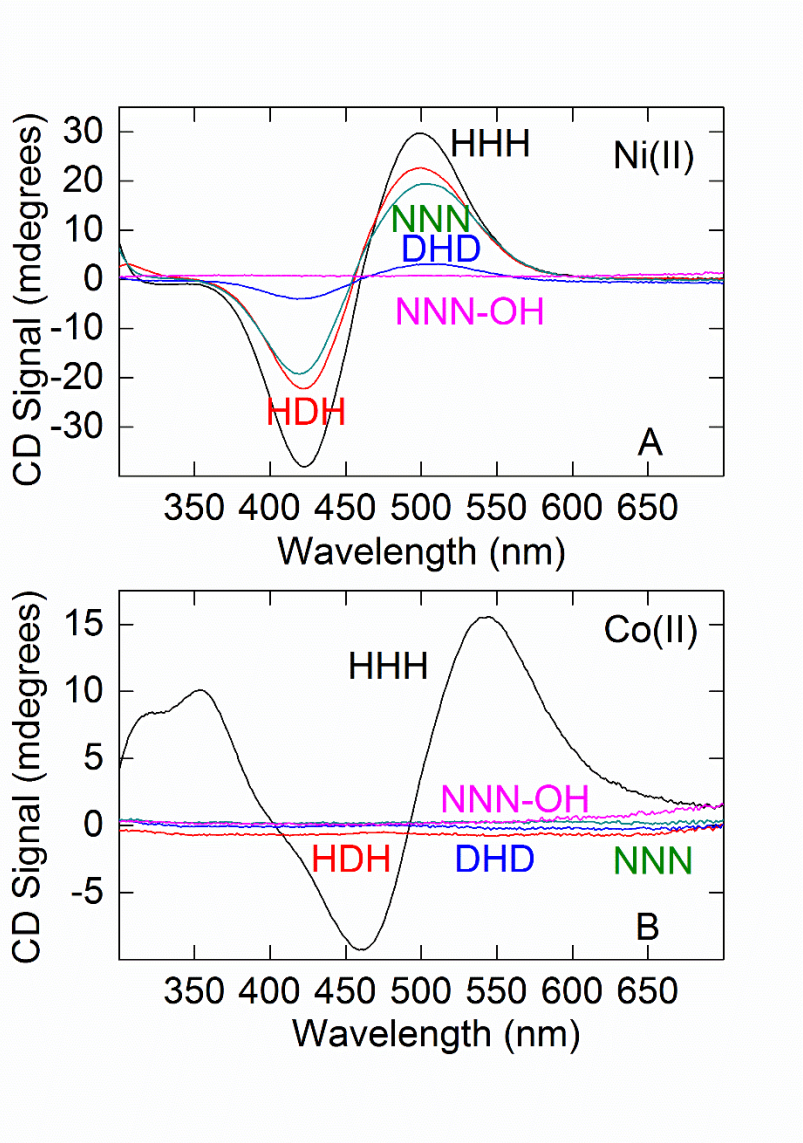

Figure 3.4. CD spectra for the peptides in the presence of A) Ni(II) and B) Co(II). The spectra were measured in the 300 to 700 nm region at pH 9 using a 4:1 metal:peptide molar ratio for the HHH (black), HDH (red), DHD (blue), NNN (green), and NNN-OH (violet) peptides.

To qualitatively determine the relative binding affinities of the metals to the peptides, a competition assay was performed in which two different metals were added to a solution containing one of the peptides. The CD spectrum of the peptide in the presence of a two-fold excess of both metals was compared to the spectrum of the peptide

with only the individual metals present. Assuming that the metal binding sites were always fully occupied, the spectrum of the peptide with both metals should represent a linear combination of the two individual spectra that are weighted by the relative occupancy. For example, the CD spectrum of the HHH peptide with both Cu(II) and Ni(II) could be described with a 65% contribution from Cu(II) and 35% from Ni(II), corresponding to a stronger binding affinity for Cu(II) compared to Ni(II) (data not shown). The results were consistent with the relative binding affinities following the order of Co(II) < Ni(II) < Cu(II) for the HHH peptide, and Ni(II) < Cu(II) for the HDH peptide.

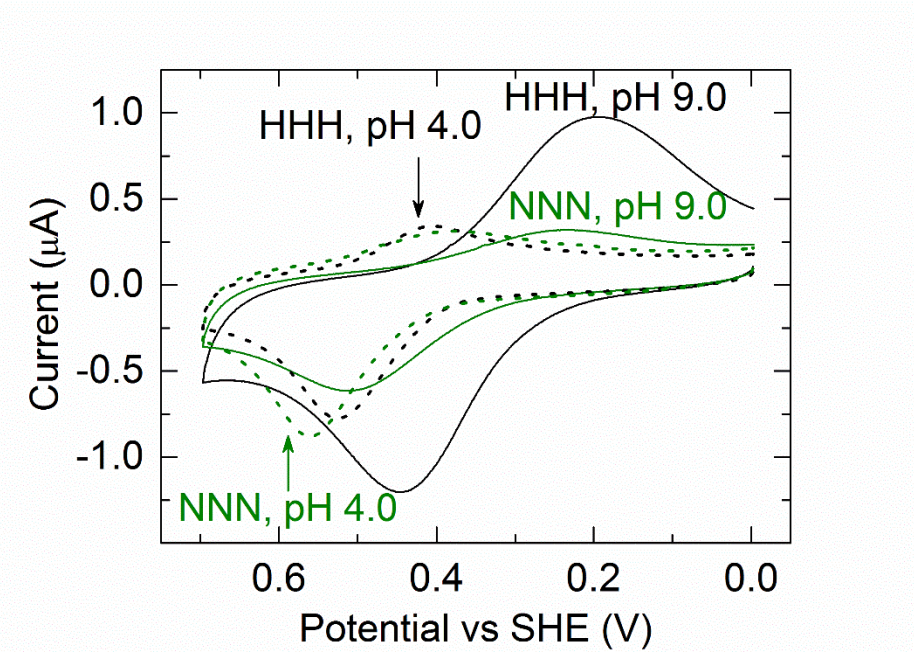

Figure 3.5. CV measurements of Cu(II) bound to the HHH (black) and NNN (green) peptides. The peptides were bound to a gold electrode by introduction of Cys at the C-terminus position. Measurements were initially performed at pH 9 (solid lines). After the electrode with the bound peptide was washed, the measurements were performed on the same sample at pH 4 (dashed lines). Potential values are relative to a standard hydrogen electrode. Scan rate, 50 mV/s.

Oxidation/reduction titrations of the bound copper

Cyclic voltammetry experiments were performed to investigate the oxidation/reduction properties of the copper bound to the HHH and NNN peptides that were modified to have C-terminal Cys residues for binding to a gold electrode. In the absence of any added metal, only baseline signals were observed. After binding of Cu(II) at pH 9, measurement of the HHH peptide showed peaks with comparable amplitude at 0.20 V and 0.45 V (Figure 3.5). These contributions most likely represent a Cu(I)/Cu(II) oxidation/reduction transition of the copper bound to the His side chains, and yields a midpoint potential of 0.32 V. The two Cu(II) bound to the HHH peptide may have different midpoint potentials with the individual peaks not being resolved but resulting in the single broad peaks.

At pH 4, the peaks at 0.20 V and 0.45 V are not present, which is consistent with the pH dependence of Cu(II) binding for this peptide. However, small peaks are observed at 0.40 V and 0.52 V (Figure 3.5). To investigate the source of these peaks, measurements were performed on the NNN peptide. At pH 4, the NNN peptide shows peak positions similar to those seen for the HHH peptide. Increasing the pH resulted in shifts of the peak positions to 0.24 V and 0.51 V with little change in amplitude. Most likely, the contributions seen for the HHH peptide at pH 4 and the NNN peptide arise from a second independent contribution due to either direct electrochemical interactions with Cu(II) or possibly mediated through the Cys linkage.

The peak separation of 0.25 V observed for the Cu(I)/Cu(II) oxidation/reduction transition is larger than the 0.06 V separation expected for a well-equilibrated system or 0 mV expected for a completely immobilized system with a one-electron

oxidation/reduction process (Sawyer *et al.* 1995, Bard and Faulkner 2000). Such restrictions on the peak separation assume a complete reversibility of the system, but the observation of a 0.25 V separation indicates that the observed oxidation/reduction changes are only quasi-reversible. In general, CV measurements of Cu(II)-binding peptides have been found to be quasi-reversible with the measured peak separations of ~0.2 V being dependent upon factors such as rearrangements of the coordination to the metal as it undergoes the oxidation/reduction change (Youngblood and Margerum 1981, Zhou and Millhauser 2012). Due to these factors, the measured midpoint potential of 0.32 V should be regarded as only an empirical tendency for the electron transfer reaction and not a true oxidation/reduction midpoint potential.

Electronic structure of the bound copper determined using EPR

The electronic structure of copper bound to the different peptides was characterized using EPR spectroscopy. This technique is well suited for probing the electronic structure of paramagnetic species bound to proteins and peptides, in particular, transition metals such as Cu(II) (d^9, S = 1/2, I = 3/2). In a magnetic field, the energy of the unpaired electron of Cu(II) is determined by two factors. One factor is the Zeeman effect, which is a measure of the energetic changes due to the interaction of the unpaired electron with an applied magnetic field $\mathbf{B_0}$. The other is hyperfine coupling (hfc) due to the interaction of the unpaired electron with the nuclear spin of Cu(II). The spin Hamiltonian, $\boldsymbol{H}$, summarizes the energetic changes of the electronic states due to these interactions:

$$\boldsymbol{H} = \beta_e \mathbf{S} \cdot \boldsymbol{g} \cdot \mathbf{B_0} + h \mathbf{S} \cdot \boldsymbol{A} \cdot \mathbf{I} \qquad 3.2$$

where $\boldsymbol{g}$ is the electronic g tensor, β_e is the electron Bohr magneton, **S** is the electron spin operator, $\boldsymbol{A}$ is the hfc tensor, h is Planck's constant, and $\boldsymbol{I}$ is the nuclear spin operator of ^{63}Cu, which has a value of 3/2 for the most common isotope. Copper is typically coordinated in a distorted octahedral geometry, with four in-plane ligands that strongly bind the metal and one or two axial ligands that weakly bind the metal (Solomon *et al.* 1992). Due to the axial symmetry, the electronic structure of the unpaired electron can be characterized with a g-tensor having an axial pattern, i.e. $g_x = g_y = g_\perp$, and $g_z = g_\parallel$ with $g_\parallel > g_\perp$. For the nuclear spin of 3/2, the EPR spectrum shows the presence of a 4-line splitting due to the electron-nuclear hfc interaction that is usually anisotropic and also characterized by an axial tensor with components, $A_\parallel$ and $A_\perp$. Usually for Cu(II), $A_\parallel$ is much larger than $A_\perp$, thus it is often the case that hyperfine splitting at $g_\perp$ is not resolved whereas the hyperfine splitting at $g_\parallel$ is shown in EPR spectra (Peisach and Blumberg 1974).

The peptides have two independent, mononuclear Cu(II) binding sites. Mononuclear copper centers are common in proteins serving in biological electron transfer and enzymatic reactions (Ryden 1984). According to their distinct spectroscopic features, mononuclear copper cofactors are divided into type I and II centers (Boas 1984, Solomon *et al.* 1992). Type I centers are formed by trigonal ligation to two His, one Cys, and usually a fourth ligand such as Met and exhibit an optical absorption signal near 600 nm due to a charge-transfer transition. Type II centers are colorless with tetragonal coordination to His, Tyr, Asp, or H_2O. Typically, type I centers have a small $A_\parallel$ (< 90 $\times 10^{-4}$ cm^{-1}) while type II centers typically have a large $A_\parallel$ (> 140 $\times 10^{-4}$ cm^{-1}) (Sakaguchi and Addison 1979, Solomon *et al.* 1992).

The samples were prepared at pH 9.2 and EPR measurements were performed at a temperature of 30 K using an X-band spectrometer. For each peptide, the spectra of the bound Cu(II) has a derivative peak centered at a *g*-value near 2.0 with four peaks at higher *g*-values due to hfc interactions (Figure 3.6). The EPR spectra corresponding to the three peptide/Cu(II) samples showed features that are distinct from those present in the spectrum of Cu(II) in solution demonstrating that such spectral differences are due to the interactions between the peptide and Cu(II). To understand the nature of these changes, the observed EPR spectra were simulated using a spin Hamiltonian (Equation 3.2) for a single type II, high-spin Cu(II) (d^9, S = 1/2, I = 3/2) system (Table 3.1).

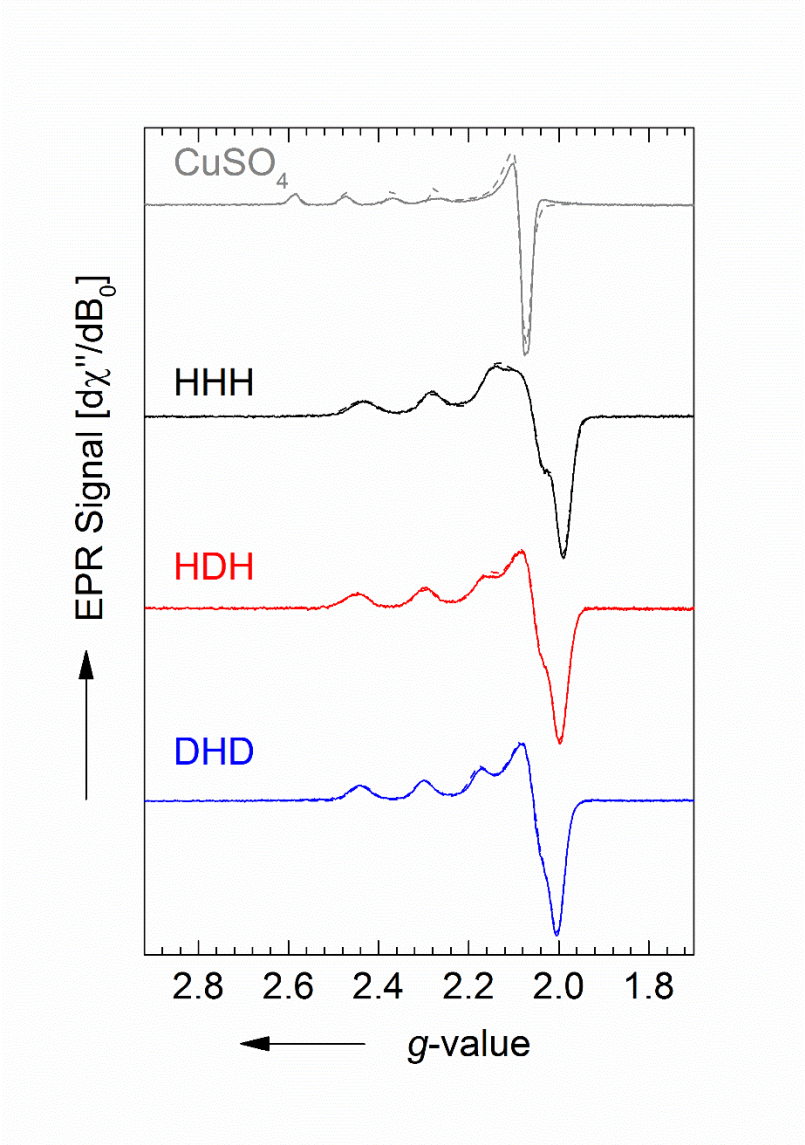

Figure 3.6. EPR spectra of Cu(II) in solution (grey) and bound to the HHH (black), HDH (red), and DHD (blue) peptides measured at X-band (9.4 GHz) and a temperature of 30 K. Also shown are best fits of the data (dashed lines) using Equation 3.2 with parameters summarized in Table 3.1.

Table 3.1. Summary of parameters obtained from the fits of X-band EPR spectra of Cu(II) in solution and bound to the peptides.

Parameters[a]	H_2O	HHH	HDH	DHD
g_x	2.084 ±0.001	2.045 ±0.001	2.049 ±0.001	2.043 ±0.001
g_y	2.090 ±0.001	2.076 ±0.001	2.065 ±0.001	2.071 ±0.001
g_z	2.421 ±0.001	2.213 ±0.001	2.227 ±0.001	2.236 ±0.001
$g_{\parallel}$[b]	2.421 ±0.001	2.213 ±0.001	2.227 ±0.001	2.236 ±0.001
$g_{\perp}$[c]	2.087 ±0.001	2.061 ±0.001	2.057 ±0.001	2.057 ±0.001
Axial distortion[d] (%)	16.0	7.4	8.3	8.7
ΔB_x (MHz)	65.9	132.2	157.6	134.3
ΔB_y (MHz)	208.5	338.1	314.1	367.4
ΔB_z (MHz)	83.3.	278.2	245.8	200.4
A_x(Cu) (10^{-4} cm^{-1})	0.0	3.0	3.2	6.9
A_y(Cu) (10^{-4} cm^{-1})	13.1	8.6	20.3	22.9
A_z(Cu) (10^{-4} cm^{-1})	134.1	191.6	190.0	172.7
$A_{\parallel}$[e](Cu) (10^{-4} cm^{-1})	134.1	191.6	190.0	172.7

[a] The fitting parameters were the three g values: g_x, g_y, g_z, the three line widths, ΔB_x, ΔB_y, ΔB_z, the three hyperfine splitting constants, A_x, A_y, A_z

[b] g_z was used as $g_{\parallel}$

[c] $g_{\perp}$ was calculated as $[(g_x^2 + g_y^2) / 2]^{1/2}$

[d] The axial distortion parameter is defined as $[(g_{\parallel} - g_{\perp})/g_{\perp}] \times 100\%$

[e] A_z was used as $A_{\parallel}$

3.3 Discussion

Peptides with different combinations of carboxylate and imidazole ligands were tested for their ability to bind transition metal ions. The metal binding was found to be dependent upon both the peptide sequence and the chemical nature of the metal (Figure 3.7), with Cu(II) binding to the HHH, HDH, and DHD peptides (Figure 3.2), Ni(II) binding to the HHH and HDH peptides, and Co(II) binding only to the HHH peptide (Figure 3.4). No binding was observed for Mn(II), Fe(II), Mg(II), or Ca(II) to any of these peptides. For Cu(II), the binding to the HHH, HDH, and DHD peptides was strongly pH dependent, with the apparent pK_a values of 6.5-6.8 being consistent with the

involvement of His in the metal binding (Figure 3.3). The bound metal was in the divalent state (Figure 3.6) but could be electrochemically oxidized (Figure 3.5). Thus, the metal binding was found to be dependent upon both the choice of metal and the peptide sequence. The dependence of metal binding upon the peptide sequence is consistent with the observation that the binding of metal ions to proteins is determined primarily by the structural arrangement of side chains that serve as coordinating ligands, with other factors, such as protein flexibility, electrostatic interactions, and steric considerations, having secondary contributions (Holm *et al.* 1996, Dudev and Lim 2008, Waldron *et al.* 2009).

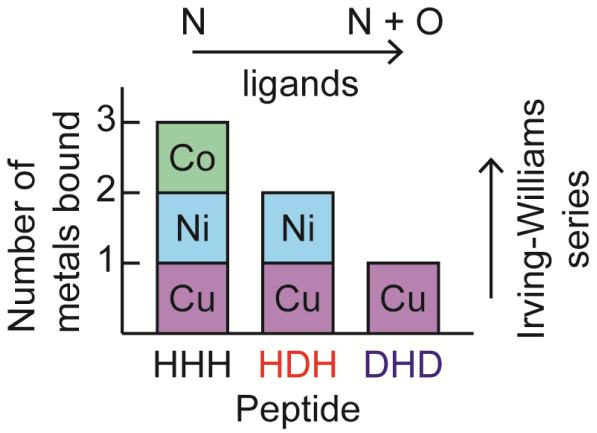

Figure 3.7 Summary of the binding of different metals to the HHH, HDH, and DHD peptides. Shown are the number of different metals bound to the three peptides and the relationship to the type of ligands found in each peptide, progressing from imidazole nitrogen ligands to mixed nitrogen and oxygen ligands, and to the increasing ligand field stabilization energies for divalent metals progressing from Cu(II) > Ni(II) > Co(II) in the Irving-Williams series.

Comparison of the relative binding affinities of the metals for each peptide revealed a consistent order. For the HHH peptide, the largest binding affinity was measured for Cu(II), followed by Ni(II), and then Co(II), with the relative binding affinities of Mn(II) and Fe(II) being smaller than could be measured. For the HDH

peptide, the highest relative binding affinity was for Cu(II), followed by Ni(II), with no measurable binding for Co(II), Fe(II), or Mn(II). The DHD peptide could only bind Cu(II), with no measurable binding for the other divalent metals. Thus, the relative binding affinities overall followed the order of [Fe(II) and Mn(II)] < Co(II) < Ni(II) < Cu(II).

This order of the relative binding affinity of each divalent metal is consistent with the Irving-Williams series. For divalent transition metals, the Irving-Williams series provides a relationship between the relative stability of divalent metals for a given set of ligands and the properties of the metals themselves, notably the ligand field stabilization energies (Irving and Williams 1948, Johnson and Nelson 1995). According to this series, the order of increasing stability is Mn(II)< Fe(II) < Co(II) < Ni(II) < Cu(II), thus, Cu(II) would be expected to form the most stable complex and Mn(II) the least stable. Assuming that the binding affinity is primarily determined by the ligand energy of each metal for a given set of ligands, then the relative binding affinity of the metals for each peptide should follow the same order as the ligand stabilization energy. Thus, the observed correlation between the order of the metal binding and the Irving-Williams series arises due to the metal binding being primarily determined by the ligand field stabilization energy.

A relationship between the binding characteristics and the chemical nature of the ligands is evident in a comparison of the electronic structure of Cu(II) bound to each peptide. The *g*-tensor represents a measure of the integral properties of Cu(II) and its ligands. The *g*-tensor obtained for Cu(II) in solution, as expected, has axial symmetry with *g*-values that are typical for Cu(II) in an octahedral geometry (Table 3.1). In

addition, the electron-nuclear hfc interaction provides information about local properties of the Cu(II) complex, i.e. the electron spin density distribution. In particular, $A_{\|}$ represents an indirect measure of the electron spin density at the Cu(II) nucleus. The values of $g_{\|}$ and $A_{\|}$ obtained for Cu(II) in solution indicate that the metal is coordinated to six ligands with at least four being oxygen atoms (Table 3.1) (Peisach and Blumberg 1974). When Cu(II) was bound to the peptide, the *g*-values and the value of $A_{\|}$ changed. For the *g*-values, this is most clearly seen from the axial distortion parameter, which had values of 16.0% for Cu(II) in H_2O and 7.4%, 8.3% and 8.7% for Cu(II) bound to the HHH, HDH and DHD peptides, respectively. The decrease of the axial distortion parameter upon peptide binding is in line with a change in the coordination geometry of Cu(II). Furthermore, the increase of the value of $A_{\|}$ from 134.1×10^{-4} cm^{-1} (H_2O) to 191.6×10^{-4} cm^{-1}, 190.0×10^{-4} cm^{-1} and 172.7×10^{-4} cm^{-1} for the HHH, HDH and DHD peptides, respectively, indicates a decrease in the number of ligands upon peptide binding. Both the *g*-tensor and hfc parameters suggest that Cu(II) binds to the peptides in a distorted square planar configuration with less than six ligands.

For the peptides, the bound Cu(II) could be coordinated to nitrogen or oxygen atoms from the side chains, backbone, or bound water molecules. Interestingly, the EPR results also reflected the differences among the peptides. The HHH peptide, in which three imidazole nitrogen atoms and one amide nitrogen are present, showed the smallest $g_{\|}$ (2.213) and the largest $A_{\|}$ ($191. 6 \times 10^{-4}$ cm^{-1}). These findings further indicate that Cu(II) is coordinated to the HHH peptide via the four nitrogens mentioned above in a close square planar geometry as previously reported (Rockcliffe *et al.* 2006). For the HDH peptide, in which the central His ligand (nitrogen donor) of each metal-binding site

was substituted with Asp (oxygen donor), the value of $g_{\|}$ increased to 2.227 and the value of $A_{\|}$ decreased to 190.0 × 10^{-4} cm^{-1}. When two of the His residues in each metal-binding region were substituted with Asp in the DHD peptide, the impact on $g_{\|}$ (2.236) and $A_{\|}$ (172.7 × 10^{-4} cm^{-1}) was even larger. This trend indicates a change in the nature of the ligands of Cu(II), i.e. a change from purely nitrogen ligands towards mixed nitrogen and oxygen ligands. According to the phenomenological model proposed by Peisach and Blumberg (1974), the values of $g_{\|}$ and $A_{\|}$ determined for the HDH and DHD peptides suggest that Cu(II) is bound to either one oxygen and three nitrogen ligands or two nitrogen and two oxygen ligands.

These differences in the ligands and electronic structure of the bound metal are correlated with the differences in the relative binding affinities. The HHH peptide, with three nitrogen ligands, has the strongest binding affinity, followed by the HDH peptide, with one oxygen and two nitrogen ligands, and the DHD peptide, with one nitrogen and two oxygen ligands. This order of the peptides for Cu(II) binding, from the HHH to HDH and DHD peptides, with increasing values of $g_{\|}$ and decreasing values for $A_{\|}$, reflects decreases in the electron spin density at the Cu(II) nucleus which would be expected for decreased metal binding affinity for the three peptides.

The correlation between the metal binding to the peptides and the Irving-Williams series is consistent with previous measurements of other peptides and proteins. For a short peptide with four His ligands, with the sequence PHGHGHGHGP, isothermal titration calorimetry showed that the Gibbs energy difference associated with metal binding increased in the order of Mn(II) < Co(II) < Ni(II) < Cu(II) (Grossoehme *et al.* 2006). The Gibbs energy difference provides another measure of metal binding and

hence these results are consistent with the prediction that the order of metal binding is correlated with the Irving-Williams stability ranking. A comparison of the binding of different divalent metals to the metallochaperones Cu(II)-cupin A and Mn(II)-cupin A demonstrated the usefulness of the Irving-Williams series for predicting metal binding in proteins (Tottey *et al.* 2008).

The results for the peptides suggest that metal binding to designed protein sequences can be preferentially biased if the design of the coordination of the metal includes consideration of the energetics for different metals as provided by the Irving-Williams series. Due to the highest stability ranking for Cu(II), the binding of Cu(II) to designed protein sequences should be more easily accomplished than designing sites for other divalent metals. The results also suggest that protein sequences containing possible metal ligands would in general be more likely to bind Cu(II). Such a preference may be reflected in the observation that Cu(II) binds to prion proteins, which are associated with a number of transmissible spongiform encephalopathies, and may play a role in neurodegenerative diseases (Millhauser 2004, Hureau 2012, Kozlowski *et al.* 2012, Viles 2012). These results and the observed correlation with the Irving-Williams series also provide a predictive basis for the design of peptides that can bind specific divalent metals for incorporation into electrochemical applications, such as bio-inspired solar cells.

3.4 Material and methods

Peptide design

A series of peptides were designed to bind divalent metal ions. All designs contained a total of 15 amino acid residues. Two identical regions containing amino acid residues for metal binding were symmetrically placed with a central Gly-Pro pair of residues to provide a potential beta-turn between the two metal-binding regions. Each peptide also contained an N-terminus Trp residue allowing monitoring of the peptide concentration using optical spectroscopy. The designs were based upon a published peptide, identified here as the HHH peptide, that has the sequence WGHGHGHGPGHGHGH (Rockcliffe *et al.* 2006). For the HHH peptide, each metal-binding region has three His residues serving as potential ligands with Gly residues as spacers.

Two peptides were designed with substitutions of different combinations of Asp and His residues. The HDH peptide has the sequence WGHGDGHGPGHGDGH in which the central His ligand of each metal-binding site is substituted with Asp. The DHD peptide has the sequence WGDGHGDGPGDGHGD in which two of the His residues in each metal-binding region are substituted with Asp. Thus, HHH, HDH and DHD all had two potential metal-binding regions consisting of different combinations of imidazole and carboxylate side chains. Finally, the NNN peptide has the sequence WGNGNGNGPGNGNGN in which all of the His residues are replaced with Asn. Each peptide has an N-terminal acetylation and C-terminal amidation except as noted for specific experiments.

Peptide preparation and purification

Peptides were synthesized using an automated peptide synthesizer (Liberty, CEM, North Carolina, USA) on an H-Rink amide Chemmatrix resin (PCAS BioMatrix, Québec, Canada), which after cleavage gave a C-terminal amide. The peptides were acetylated at the N-terminus. Racemization of the histidine side chain during coupling was reduced by having the microwave turned off and increasing the reaction time during coupling of histidine (Palasek *et al.* 2007). For the synthesis of the HDH and DHD peptides, piperazine was utilized instead of piperidine to limit aspartimide formation (Palasek *et al.* 2007). For all peptides, after cleavage from the resin and simultaneous side-chain deprotection by trifluoroacetic acid, the sample was purified through reverse phase high performance liquid chromatography on a Waters 1525 HPLC system (Waters, Massachusetts, USA) using a C18 semi preparative column (Vydac from Grace Davison Discovery Sciences, Illinois, USA) or a C18 analytical column (Aapptec, Kentucky, USA). For each peptide, the molecular weight was verified by matrix-assisted laser desorption and ionization: time of flight mass spectrometry using an Applied Biosystems DE-STR mass spectrometer (AB, Framingham, USA). The instrument was operated under positive ion mode with an α-cyano-4-hydroxycinnamic acid matrix. Mass spectra were measured in triplicate. The purity of the peptides was verified by C18 analytical HPLC. After purification, the peptides were lyophilized and stored at 4 °C.

To investigate the involvement of the C-terminal amidation, the NNN peptide was modified to have a C-terminal carboxylate group using a Fmoc-Asn(Trt)-Wang resin (Novabiochem, EMD Chemicals, New Jersey, USA) (Wang 1973). The HHH and NNN peptides were modified with a C-terminal GGC sequence for binding to a gold electrode

in electrochemical measurements and obtained from GenScript (New Jersey, USA) with purity greater than 98% as measured by HPLC analysis.

CD spectroscopy

The CD spectra were recorded on a Jasco J-710 spectropolarimeter (JASCO, Tokyo, Japan) at room temperature with the samples under the flow of nitrogen gas. The peptide concentration was adjusted to 0.2 mM and the metal was added immediately prior to measurement according to the specified metal to peptide molar ratio. Metals were added to solutions containing the peptides using 100 mM stock solutions of $MgSO_4$, $MnSO_4$, $FeSO_4$, $CoCl_2$, $NiSO_4$ and $CuSO_4$. For samples with Fe(II), tris(2-carboxyethyl) phosphine was added to keep the metal reduced. The pH was measured both before and after the CD measurement and found not to change within ± 0.05. Typically, a 50 mM buffer concentration was used for measurements in the 210-260 nm and 300-700 nm ranges although an 8 mM buffer concentration was used to extend the spectral range to 200-260 nm. The samples were placed in 1 mm and 1 cm path-length quartz cuvettes for measurements in the 200-260 nm and 300-700 nm range, respectively. The following buffers were used: H_3PO_4 from pH 1.5-2.9, formic acid from pH 2.9-4.5, acetic acid from pH 4.0-5.5, 2-(N-morpholino)ethanesulfonic acid (MES) from pH 5.5-6.8, 3-(N-morpholino)propanesulfonic acid (MOPS) from pH 6.5-8.0, 3-[[1,3-dihydroxy-2-(hydroxymethyl)propan-2-yl]amino]propane-1-sulfonic acid (TAPS) from pH 7.8-9.0, and N-Cyclohexyl-2-aminoethanesulfonic acid (CHES) from pH 8.8-10.3, with the pH values adjusted as needed using potassium hydroxide. The pH dependence of the CD amplitude, A, was analyzed using the Henderson-Hasselbalch equation according to:

$$A = 1/\{1 + 10^{pK_a - pH}\} \quad 3.1$$

where pK_a is the acid dissociation constant. For the competition assay, the measurements were performed using a 0.2 mM peptide concentration and two divalent metals, at a concentration of 0.4 mM each, in 50 mM TAPS pH 8.5.

EPR spectroscopy

Samples with a peptide concentration of 1 mM were prepared in 50 mM CHES buffer at pH 9.2 with 15% ethylene glycol as a cryoprotectant. Metals were added to solutions containing the peptides using 100 mM stock solutions of $CuSO_4$. To minimize the effect of free Cu(II), a 2:1 molar ratio of metal to peptide was used for the HHH and DHD peptides, and a 1:1 molar ratio was used for the HDH and NNN peptides. 1 mM $CuSO_4$ in 50 mM pH 9.2 CHES buffer resulted in precipitation, and the suspended sample were EPR silent, and thus 1 mM $CuSO_4$ in water was used as the solution Cu(II) sample. This solution had a pH value of 5.0. Studies were performed at the EPR Facility of Arizona State University. Continuous wave EPR spectra were recorded at a temperature of 30 K using a Bruker ELEXSYS E580 continuous wave X-band spectrometer (Bruker, Rheinstetten, Germany) equipped with an Oxford Model 900 EPL liquid helium cryostat (Oxford Instruments, Oxfordshire, UK). The magnetic field modulation frequency was 100 kHz; the amplitude was 1 mT; the microwave power was 16 mW and the microwave frequency was 9.43 GHz; the sweep time was 84 s. The EPR spectra were simulated using EasySpin (v 4.0.0), a computational package developed by Stoll and Schweiger (Stoll and Schweiger 2006) and based on Matlab (The MathWorks, Natick, MA, USA). The model used for the EPR simulations considered a single Cu(II)

ion (S = 1/2, I = 3/2). The fitting parameters were the g values (g_x, g_y and g_z), the line widths (ΔB_x, ΔB_y and ΔB_z), and the hyperfine coupling splittings (A_x, A_y and A_z). The fitting procedure was similar to the one previously described (Flores *et al.* 2007).

Electrochemical measurements

Electrochemical measurements were performed using a CHI1200A potentiostat (CH Instruments), a VC-2 voltammetry cell (BASi) with a built-in Pt counter electrode, a Ag/AgCl reference electrode (BASi), and a gold (BASi) working electrode. The reported potential was converted to values vs standard hydrogen electrode (SHE) by adding 0.197 V. The CV was performed using a 50 mV/s scan rate, with the potential cycled between -0.2 V and 0.5 V against the Ag/AgCl reference electrode. No peak position shifts were observed upon changes of the scan rate. The anodic current was defined as positive. Measurements were performed in 100 mM KCl and either 50 mM CHES, pH 9.0 or 50 mM formic acid, pH 4.0.

For the CV experiments, the HHH and NNN peptides were modified with a C-terminal Cys for attachment to the gold electrode. The peptide at a 0.2 mM concentration together with 5mM tris(2-carboxyethyl)phosphine (TCEP) in 5 mM $CuSO_4$ and 50 mM CHES pH 9.0 was incubated on the gold electrode overnight to form a thiol self-assembled monolayer (Ashur *et al.* 2012). TCEP was used to protect the thiol group from being oxidized by air. After rinsing with distilled water, the CV measurement was performed in 50 mM pH 9 CHES buffer at a scan rate of 50 mV/s. The gold electrode with the attached peptide was then washed using buffers. The pH values of the buffers decreased stepwise down to pH 4.0, after which a second CV measurement was

performed. When the electrode with the attached peptide was washed in 50 mM CHES pH 9.0 instead of the decreasing pH solutions, the CV amplitudes did not change within error.

CHAPTER 4

OUTLOOK

Finding a clean and renewable replacement for fossil fuels to meet the ever-increasing human energy demand is one of the grand challenges for human society in the 21st century. Solar energy is an attractive candidate to answer the call. To date, the best solar photovoltaic cell could convert 44.7 % of the energy from the solar spectrum into electricity (Fraunhofer-Gesellschaft 2013). Despite the good efficiencies achieved in solar photovoltaic cells, one cannot depend on photovoltaic cells during the nighttime when there is no sunlight. The diurnal cycle could be overcome by turning solar-generated electricity into chemical fuels (Figure 1.4.a), which could be converted into electrical or mechanical power around the clock. Cells that convert solar energy into chemical fuels such as hydrogen are usually termed photoelectrochemical cells (PECs).

To develop a PEC with high efficiency, catalysts are required. For PEC that splits water into oxygen and hydrogen, both water oxidation catalysts (WOC) and proton reduction catalysts (PRC) are needed. Cheap and abundant materials must be used for these catalysts. The metals Pt and Ru can be used for versatile catalysts; however, they are too rare on earth and too expensive to be used in large scale. For this sake, first-row transition metals such as Mn, Fe, Ni and Co are ideal candidates. In photosynthesis, water is oxidized using a Mn-based catalyst stabilized within a protein environment. However, the harsh oxidizing conditions readily damage the protein environment forcing the living organism to repair the proteins every 30 mins to 8 h (Melis 1999). This remediation rate is not ideal for a sustainable man-made system. In practice, a robust catalyst that can last for years is needed. So far, no artificial WOC could meet this requirement. Among the

various reported WOCs, metal oxides are the most promising to serve as robust catalysts for oxygen evolution. In addition, the cell design must achieve optimal solar-to-fuel energy conversion efficiency.

The heterogeneous Ni-hydroxide water oxidation catalyst reported in this dissertation was generated by electrochemical deposition and the driving force of splitting water was also provided by electricity. In short, this system converts electricity into chemical energy. For this water oxidation catalyst to directly turn solar energy into chemical fuels, this Ni-Gly system has to be put into test in the presence of photosensitizer and light. In this scenario, the catalyst will be generated by photochemical process, and the later water oxidation process shall also be fueled solely under the driving force of light.

The future of sustainable solar fuel is bright. Imagine a human society using solar energy by converting seawater into hydrogen and oxygen during the daytime and turning it into electricity in fuel-cell power plants. During the whole process, the only by-product generated would be water. Though this is a dream for now, it could be a reality in the near future.

REFERENCES

Adman, E. T. and L. H. Jensen. 1981. Structural features of azurin at 2.7 Å resolution. *Israel Journal of Chemistry* **21**(1): 8-12.

Amblard, M., J. A. Fehrentz, J. Martinez and G. Subra. 2006. Methods and protocols of modern solid phase peptide synthesis. *Molecular Biotechnology* **33**(3): 239-254.

Artero, V. and M. Fontecave. 2013. Solar fuels generation and molecular systems: Is it homogeneous or heterogeneous catalysis? *Chemical Society Reviews* **42**(6): 2338-2356.

Ashur, I., O. Schulz, C. L. McIntosh, I. Pinkas, R. Ros and A. K. Jones. 2012. Transparent gold as a platform for adsorbed protein spectroelectrochemistry: Investigation of cytochrome c and azurin. *Langmuir* **28**(13): 5861-5871.

Bard, A. J. and L. R. Faulkner. 2001. *Electrochemical methods: Fundamentals and applications*. New York: Wiley.

Barnett, S. M., K. I. Goldberg and J. M. Mayer. 2012. A soluble copper-bipyridine water-oxidation electrocatalyst. *Nature Chemistry* **4**(6): 498-502.

Barrette, W. C., Jr., D. T. Sawyer, J. A. Fee and K. Asada. 1983. Potentiometric titrations and oxidation/reduction potentials of several iron superoxide dismutases. *Biochemistry* **22**(3): 624-627.

Bediako, D. K., B. Lassalle-Kaiser, Y. Surendranath, J. Yano, V. K. Yachandra and D. G. Nocera. 2012. Structure-activity correlations in a nickel-borate oxygen evolution catalyst. *Journal of the American Chemical Society* **134**(15): 6801-6809.

Bediako, D. K., Y. Surendranath and D. G. Nocera. 2013. Mechanistic studies of the oxygen evolution reaction mediated by a nickel-borate thin film electrocatalyst. *Journal of the American Chemical Society* **135**(9): 3662-3674.

Bertini, I. 2007. *Biological inorganic chemistry: Structure and reactivity*. Sausalito, California: University Science Books.

Biesinger, M. C., L. W. M. Lau, A. R. Gerson and R. S. C. Smart. 2012. The role of the Auger parameter in XPS studies of nickel metal, halides and oxides. *Physical Chemistry Chemical Physics* 14(7): 2434-2442.

Birss, V. I., A. Damjanovic and P. G. Hudson. 1986. Oxygen evolution at platinum-electrodes in alkaline-solutions .2. Mechanism of the reaction. *Journal of the Electrochemical Society* **133**(8): 1621-1625.

Blankenship, R. E. 2014. *Molecular mechanisms of photosynthesis*. New York: Wiley.

Boas, J. F. 1984. Electron paramagnetic resonance of copper proteins. *Copper proteins copper enzymes*. R. Lontie. Boca Raton, Florida: CRC Press. **I:** 5-62.

Bockris, J. O. and A. Huq. 1956. The mechanism of the electrolytic evolution of oxygen on platinum. *Proceedings of the Royal Society of London Series A: Mathematical and Physical Sciences* **237**(1209): 277-296.

Brown, W., B. Iverson, E. Anslyn and C. Foote. 2013. *Organic chemistry*. Independence, Kentucky: Cengage Learning.

Cady, C. W., K. E. Shinopoulos, R. H. Crabtree and G. W. Brudvig. 2010. $[(H_2O)(terpy)Mn(\mu\text{-}O)_2Mn(terpy)(OH_2)](NO_3)_3$ (terpy = 2,2':6,2"-terpyridine) and its relevance to the oxygen-evolving complex of photosystem II examined through pH dependent cyclic voltammetry. *Dalton Trans* **39**(16): 3985-3989.

Calhoun, J. R., F. Nastri, O. Maglio, V. Pavone, A. Lombardi and W. F. DeGrado. 2005. Artificial diiron proteins: From structure to function. *Biopolymers* **80**(2-3): 264-278.

Cao, R., W. Lai and P. Du. 2012. Catalytic water oxidation at single metal sites. *Energy & Environmental Science* **5**(8): 8134.

Cheniae, G. M. and I. F. Martin. 1969. Photoreaction of manganese catalyst in photosynthetic oxygen evolution. *Plant Physiology* **44**(3): 351-360.

Cheniae, G. M. and I. F. Martin. 1970. Sites of function of manganese within photosystem II. Roles in O_2 evolution and system II. *Biochimica et Biophysica Acta (BBA) - Bioenergetics* **197**(2): 219-239.

Concepcion, J. J., J. W. Jurss, J. L. Templeton and T. J. Meyer. 2008. One site is enough. Catalytic water oxidation by $[Ru(tpy)(bpm)(OH_2)]^{2+}$ and $[Ru(tpy)(bpz)(OH_2)]^{2+}$. *Journal of the American Chemical Society* **130**(49): 16462-16463.

Conway, B. E. and T. C. Liu. 1990. Characterization of electrocatalysis in the oxygen evolution reaction at platinum by evaluation of behavior of surface intermediate states at the oxide film. *Langmuir* **6**(1): 268-276.

Cook, T. R., D. K. Dogutan, S. Y. Reece, Y. Surendranath, T. S. Teets and D. G. Nocera. 2010. Solar energy supply and storage for the legacy and nonlegacy worlds. *Chemical Reviews* **110**(11): 6474-6502.

Cotton, F. A., G. Wilkinson and P. L. Gaus. 1995. *Basic inorganic chemistry*. New York: Wiley.

Crabtree, R. H. 2012. Resolving heterogeneity problems and impurity artifacts in operationally homogeneous transition metal catalysts. *Chemical Reviews* **112**(3): 1536-1554.

Dau, H. and M. Haumann. 2008. The manganese complex of photosystem II in its reaction cycle: basic framework and possible realization at the atomic level. *Coordination Chemistry Reviews* **252**(3-4): 273-295.

Dau, H., I. Zaharieva and M. Haumann. 2012. Recent developments in research on water oxidation by photosystem II. *Current Opinion in Chemical Biology* **16**(1–2): 3-10.

DeGrado, W. F., C. M. Summa, V. Pavone, F. Nastri and A. Lombardi. 1999. *De novo* design and structural characterization of proteins and metalloproteins. *Annual Review of Biochemistry* **68**: 779-819.

Di Costanzo, L., H. Wade, S. Geremia, L. Randaccio, V. Pavone, W. F. DeGrado and A. Lombardi. 2001. Toward the *de novo* design of a catalytically active helix bundle: A substrate-accessible carboxylate-bridged dinuclear metal center. *Journal of the American Chemical Society* **123**(51): 12749-12757.

Dinca, M., Y. Surendranath and D. G. Nocera. 2010. Nickel-borate oxygen-evolving catalyst that functions under benign conditions. *Proceedings of the National Academy of Sciences of the United States of America* **107**(23): 10337-10341.

Doyle, R. L., I. J. Godwin, M. P. Brandon and M. E. Lyons. 2013. Redox and electrochemical water splitting catalytic properties of hydrated metal oxide modified electrodes. *Physical Chemistry Chemical Physics* **15**(33): 13737-13783.

Duan, L., F. Bozoglian, S. Mandal, B. Stewart, T. Privalov, A. Llobet and L. Sun. 2012. A molecular ruthenium catalyst with water-oxidation activity comparable to that of photosystem II. *Nature Chemistry* **4**(5): 418-423.

Dudev, T. and C. Lim. 2008. Metal binding affinity and selectivity in metalloproteins: Insights from computational studies. *Annual Review of Biophysics* **37**: 97-116.

Edwards, R. A., H. M. Baker, M. M. Whittaker, J. W. Whittaker, G. B. Jameson and E. N. Baker. 1998. Crystal structure of escherichia coli manganese superoxide dismutase at 2.1 Å resolution. *Journal of Biological Inorganic Chemistry* **3**(2): 161-171.

Ellis, W. C., N. D. McDaniel, S. Bernhard and T. J. Collins. 2010. Fast water oxidation using iron. *Journal of the American Chemical Society* **132**(32): 10990-10991.

Faiella, M., C. Andreozzi, R. T. de Rosales, V. Pavone, O. Maglio, F. Nastri, W. F. DeGrado and A. Lombardi. 2009. An artificial di-iron oxo-protein with phenol oxidase activity. *Nature Chemical Biology* **5**(12): 882-884.

Farrer, B. T. and V. L. Pecoraro. 2003. Hg(ii) binding to a weakly associated coiled coil nucleates an encoded metalloprotein fold: A kinetic analysis. *Proceedings of the National Academy of Sciences of the United States of America* **100**(7): 3760-3765.

Fee, J. A. and P. E. DiCorleto. 1973. Observations on the oxidation-reduction properties of bovine erythrocyte superoxide dismutase. *Biochemistry* **12**(24): 4893-4899.

Ferguson, J. D. 2003. Focused™ microwave instrumentation from CEM corporation. *Molecular Diversity* **7**(2-4): 281-286.

Flores, M., R. Isaacson, E. Abresch, R. Calvo, W. Lubitz and G. Feher. 2007. Protein-cofactor interactions in bacterial reaction centers from rhodobacter sphaeroides r-26: II. Geometry of the hydrogen bonds to the primary quinone Q_A^{-} by ^{1}H and ^{2}H ENDOR spectroscopy. *Biophysical Journal* **92**(2): 671-682.

Fraunhofer-Gesellschaft. (2013, 9-24-2013). "http://phys.Org/news/2013-09-world-solar-cell-efficiency.html." Retrieved 5-12-2014, 2014, from http://phys.org/news/2013-09-world-solar-cell-efficiency.html.

Freeman, H. C. and J. M. Guss. 1978. Crystallographic studies of metal-peptide complexes. IX. Disodium bis(glycylglycinato)nickelate(ii) octahydrate and disodium bis(glycylglycinato)nickelate(ii) nonahydrate. *Acta Crystallographica Section B* **34**(8): 2451-2458.

Fry, A. J. 1989. *Synthetic organic electrochemistry*. New York: Wiley.

Fukuzumi, S. and D. Hong. 2014. Homogeneous *versus* heterogeneous catalysts in water oxidation. *European Journal of Inorganic Chemistry* **2014**(4): 645-659.

Gersten, S. W., G. J. Samuels and T. J. Meyer. 1982. Catalytic oxidation of water by an oxo-bridged ruthenium dimer. *Journal of the American Chemical Society* **104**(14): 4029-4030.

Gray, H. B., B. G. Malmstrom and R. J. Williams. 2000. Copper coordination in blue proteins. *Journal of Biological Inorganic Chemistry* **5**(5): 551-559.

Greenfield, N. J. 1996. Methods to estimate the conformation of proteins and polypeptides from circular dichroism data. *Analytical Biochemistry* **235**(1): 1-10.

Greenfield, N. J. 2006. Using circular dichroism spectra to estimate protein secondary structure. *Nature Protocols* **1**(6): 2876-2890.

Grossoehme, N. E., S. Akilesh, M. L. Guerinot and D. E. Wilcox. 2006. Metal-binding thermodynamics of the histidine-rich sequence from the metal-transport protein IRT1 of *Arabidopsis thaliana*. *Inorganic Chemistry* **45**(21): 8500-8508.

Grundmeier, A. and H. Dau. 2012. Structural models of the manganese complex of photosystem II and mechanistic implications. *Biochimica Et Biophysica Acta-Bioenergetics* **1817**(1): 88-105.

Gust, D., T. A. Moore and A. L. Moore. 2009. Solar fuels via artificial photosynthesis. *Accounts of Chemical Research* **42**(12): 1890-1898.

Gust, D., T. A. Moore and A. L. Moore. 2012. Realizing artificial photosynthesis. *Faraday Discussions* **155**: 9-26.

Hart, P. J., M. M. Balbirnie, N. L. Ogihara, A. M. Nersissian, M. S. Weiss, J. S. Valentine and D. Eisenberg. 1999. A structure-based mechanism for copper-zinc superoxide dismutase. *Biochemistry* **38**(7): 2167-2178.

Hart, P. J., A. M. Nersissian, R. G. Herrmann, R. M. Nalbandyan, J. S. Valentine and D. Eisenberg. 1996. A missing link in cupredoxins: Crystal structure of cucumber stellacyanin at 1.6 Å resolution. *Protein Science* **5**(11): 2175-2183.

Heinze, J. 1984. Cyclic voltammetry—"electrochemical spectroscopy". New analytical methods (25). *Angewandte Chemie International Edition in English* **23**(11): 831-847.

Herbst, R. W., A. Guce, P. A. Bryngelson, K. A. Higgins, K. C. Ryan, D. E. Cabelli, S. C. Garman and M. J. Maroney. 2009. Role of conserved tyrosine residues in NiSOD catalysis: A case of convergent evolution. *Biochemistry* **48**(15): 3354-3369.

Holm, R. H., P. Kennepohl and E. I. Solomon. 1996. Structural and functional aspects of metal sites in biology. *Chemical Reviews* **96**(7): 2239-2314.

Hong, D., Y. Yamada, T. Nagatomi, Y. Takai and S. Fukuzumi. 2012. Catalysis of nickel ferrite for photocatalytic water oxidation using $[Ru(bpy)_3]^{2+}$ and $S_2O_8^{2-}$. *Journal of the American Chemical Society* 134(48): 19572-19575.

Hureau, C. 2012. Coordination of redox active metal ions to the amyloid precursor protein and to amyloid-β peptides involved in alzheimer disease. Part 1: An overview. *Coordination Chemistry Reviews* **256**(19–20): 2164-2174.

Inoue, T., H. Sugawara, S. Hamanaka, H. Tsukui, E. Suzuki, T. Kohzuma and Y. Kai. 1999. Crystal structure determinations of oxidized and reduced plastocyanin from the cyanobacterium S*ynechococcus* sp. PCC 7942. *Biochemistry* **38**(19): 6063-6069.

Irving, H. and R. J. P. Williams. 1948. Order of stability of metal complexes. *Nature* **162**(4123): 746-747.

Johnson, D. A. and P. G. Nelson. 1995. Factors determining the ligand field stabilization energies of the hexaaqua 2+ complexes of the first transition series and the Irving-Williams order. *Inorganic Chemistry* **34**(22): 5666-5671.

Joliot, P. 2005. Period-four oscillations of the flash-induced oxygen formation in photosynthesis. *Discoveries in photosynthesis*. Govindjee, J. T. Beatty, H. Gest and J. Allen: Springer Netherlands. **20:** 371-378.

Joliot, P., G. Barbieri and R. Chabaud. 1969. Un nouveau modele des centres photochimiques du systeme II. *Photochemistry and Photobiology* **10**(5): 309-329.

Kanan, M. W. and D. G. Nocera. 2008. In situ formation of an oxygen-evolving catalyst in neutral water containing phosphate and Co^{2+}. *Science* **321**(5892): 1072-1075.

Kanan, M. W., J. Yano, Y. Surendranath, M. Dinca, V. K. Yachandra and D. G. Nocera. 2010. Structure and valency of a cobalt-phosphate water oxidation catalyst determined by *in situ* X-ray spectroscopy. *Journal of the American Chemical Society* **132**(39): 13692-13701.

Kaplan, J. and W. F. DeGrado. 2004. *De novo* design of catalytic proteins. *Proceedings of the National Academy of Sciences of the United States of America* **101**(32): 11566-11570.

Kharenko, O. A. and M. Y. Ogawa. 2004. Metal-induced folding of a designed metalloprotein. *Journal of Inorganic Biochemistry* **98**(11): 1971-1974.

Kim, M. K. and A. E. Martell. 1966. Copper (ii) complexes of triglycine and tetraglycine. *Journal of the American Chemical Society* **88**(5): 914-918.

Kletzin, A. and M. W. Adams. 1996. Tungsten in biological systems. *FEMS Microbiology Reviews* **18**(1): 5-63.

Koder, R. L. and P. L. Dutton. 2006. Intelligent design: The *de novo* engineering of proteins with specified functions. *Dalton Trans*(25): 3045-3051.

Kohn, W. D., C. M. Kay, B. D. Sykes and R. S. Hodges. 1998. Metal ion induced folding of a *de novo* designed coiled-coil peptide. *Journal of the American Chemical Society* **120**(6): 1124-1132.

Kok, B., B. Forbush and M. McGloin. 1970. Cooperation of charges in photosynthetic O_2 evolution-I. A linear four step mechanism. *Photochemistry and Photobiology* **11**(6): 457-475.

Kozlowski, H., M. Luczkowski, M. Remelli and D. Valensin. 2012. Copper, zinc and iron in neurodegenerative diseases (alzheimer's, parkinson's and prion diseases). *Coordination Chemistry Reviews* **256**(19–20): 2129-2141.

Lawrence, G. D. and D. T. Sawyer. 1979. Potentiometric titrations and oxidation-reduction potentials of manganese and copper-zinc superoxide dismutases. *Biochemistry* **18**(14): 3045-3050.

Lewis, N. S. and D. G. Nocera. 2006. Powering the planet: Chemical challenges in solar energy utilization. *Proceedings of the National Academy of Sciences of the United States of America* **103**(43): 15729-15735.

Li, X., K. Suzuki, K. Kanaori, K. Tajima, A. Kashiwada, H. Hiroaki, D. Kohda and T. Tanaka. 2000. Soft metal ions, Cd(ii) and Hg(ii), induce triple-stranded alpha-helical assembly and folding of a *de novo* designed peptide in their trigonal geometries. *Protein Science* **9**(7): 1327-1333.

Liu, F., J. J. Concepcion, J. W. Jurss, T. Cardolaccia, J. L. Templeton and T. J. Meyer. 2008. Mechanisms of water oxidation from the blue dimer to photosystem II. *Inorganic Chemistry* **47**(6): 1727-1752.

Lloyd-Williams, P., F. Albericio and E. Giralt. 1993. Convergent solid-phase peptide synthesis. *Tetrahedron* **49**(48): 11065-11133.

Lombardi, A., C. M. Summa, S. Geremia, L. Randaccio, V. Pavone and W. F. DeGrado. 2000. Retrostructural analysis of metalloproteins: Application to the design of a minimal model for diiron proteins. *Proceedings of the National Academy of Sciences of the United States of America* **97**(12): 6298-6305.

Lu, Y., N. Yeung, N. Sieracki and N. M. Marshall. 2009. Design of functional metalloproteins. *Nature* **460**(7257): 855-862.

Martinez, J. and M. Bodanszky. 1978. Side reactions in peptide synthesis. *International Journal of Peptide and Protein Research* **12**(5): 277-283.

McAlpin, J. G., Y. Surendranath, M. Dincă, T. A. Stich, S. A. Stoian, W. H. Casey, D. G. Nocera and R. D. Britt. 2010. EPR evidence for Co(iv) species produced during water oxidation at neutral pH. *Journal of the American Chemical Society* **132**(20): 6882-6883.

McDaniel, N. D., F. J. Coughlin, L. L. Tinker and S. Bernhard. 2008. Cyclometalated iridium(iii) aquo complexes: Efficient and tunable catalysts for the homogeneous oxidation of water. *Journal of the American Chemical Society* **130**(1): 210-217.

McEvoy, J. P. and G. W. Brudvig. 2006. Water-splitting chemistry of photosystem II. *Chemical Reviews* **106**(11): 4455-4483.

Melis, A. 1999. Photosystem-ii damage and repair cycle in chloroplasts: What modulates the rate of photodamage *in vivo*? *Trends in Plant Science* **4**(4): 130-135.

Merlino, A., I. Russo Krauss, I. Castellano, M. R. Ruocco, A. Capasso, E. De Vendittis, B. Rossi and F. Sica. 2014. Structural and denaturation studies of two mutants of a cold adapted superoxide dismutase point to the importance of electrostatic interactions in protein stability. *Biochimica et Biophysica Acta* **1844**(3): 632-640.

Merrifield, R. B. 1963. Solid phase peptide synthesis. I. The synthesis of a tetrapeptide. *Journal of the American Chemical Society* **85**(14): 2149-2154.

Millhauser, G. L. 2004. Copper binding in the prion protein. *Accounts of Chemical Research* **37**(2): 79-85.

Mullins, C. S. and V. L. Pecoraro. 2008. Reflections on small molecule manganese models that seek to mimic photosynthetic water oxidation chemistry. *Coordination Chemistry Reviews* **252**(3-4): 416-443.

Nagy, N. V., T. Szabó-Planka, A. Rockenbauer, G. Peintler, I. Nagypál and L. Korecz. 2003. Great structural variety of complexes in copper(ii)−oligoglycine systems: Microspeciation and coordination modes as studied by the two-dimensional simulation of electron paramagnetic resonance spectra. *Journal of the American Chemical Society* **125**(17): 5227-5235.

Najafpour, M. M., A. N. Moghaddam, S. I. Allakhverdiev and Govindjee. 2012. Biological water oxidation: Lessons from nature. *Biochimica Biophysica Acta-Bioenergetics* **1817**(8): 1110-1121.

Nakagawa, T., N. S. Bjorge and R. W. Murray. 2009. Electrogenerated IrO_x nanoparticles as dissolved redox catalysts for water oxidation. *Journal of the American Chemical Society* **131**(43): 15578-15579.

Nalwa, H. S. 2001. *Handbook of surfaces and interfaces of materials, five-volume set*. Waltham, Massachusetts: Academic Press.

Nanda, V., M. M. Rosenblatt, A. Osyczka, H. Kono, Z. Getahun, P. L. Dutton, J. G. Saven and W. F. Degrado. 2005. *De novo* design of a redox-active minimal rubredoxin mimic. *Journal of the American Chemical Society* **127**(16): 5804-5805.

Nicol ás, E., E. Pedroso and E. Girald. 1989. Formation of aspartimide peptides in Asp-Gly sequences. *Tetrahedron Letters* **30**(4): 497-500.

Orr, L. and Govindjee. 2010. Photosynthesis online. *Photosynthesis Research* **105**(2): 167-200.

Ose, D. E. and I. Fridovich. 1979. Manganese-containing superoxide dismutase from *Escherichia Coli*: Reversible resolution and metal replacements. *Archives of Biochemistry and Biophysics* **194**(2): 360-364.

Palasek, S. A., Z. J. Cox and J. M. Collins. 2007. Limiting racemization and aspartimide formation in microwave-enhanced fmoc solid phase peptide synthesis. *Journal of Peptide Science* **13**(3): 143-148.

Peisach, J. and W. E. Blumberg. 1974. Structural implications derived from the analysis of electron paramagnetic resonance spectra of natural and artificial copper proteins. *Archives of Biochemistry and Biophysics* **165**(2): 691-708.

Pettersen, E. F., T. D. Goddard, C. C. Huang, G. S. Couch, D. M. Greenblatt, E. C. Meng and T. E. Ferrin. 2004. UCSF chimera: a visualization system for exploratory research and analysis. *Journal of Computational Chemistry* **25**(13): 1605-1612.

Reig, A. J., M. M. Pires, R. A. Snyder, Y. Wu, H. Jo, D. W. Kulp, S. E. Butch, J. R. Calhoun, T. Szyperski, E. I. Solomon and W. F. DeGrado. 2012. Alteration of the oxygen-dependent reactivity of *de novo* due ferri proteins. *Nature Chemistry* **4**(11): 900-906.

Risch, M., K. Klingan, J. Heidkamp, D. Ehrenberg, P. Chernev, I. Zaharieva and H. Dau. 2011. Nickel-oxido structure of a water-oxidizing catalyst film. *Chemical Communications (Cambridge, England)* **47**(43): 11912-11914.

Rockcliffe, D. A., A. Cammers, A. Murali, W. K. Russell and V. J. DeRose. 2006. *De novo* design and spectroscopic characterization of a dinucleating copper-binding pentadecapeptide. *Inorganic Chemistry* **45**(2): 472-474.

Roy, A., C. Madden and G. Ghirlanda. 2012. Photo-induced hydrogen production in a helical peptide incorporating a [FeFe] hydrogenase active site mimic. *Chemical Communications* 48(79): 9816-9818.

Ryden, L. 1984. Structure and evolution of the small blue proteins. *Copper proteins and copper enzymes*. R. Lontie. Boca Raton, Florida: CRC Press. **I:** 157-182.

Sakaguchi, U. and A. W. Addison. 1979. Spectroscopic and redox studies of some copper(ii) complexes with biomimetic donor atoms: Implications for protein copper centres. *Journal of the Chemical Society, Dalton Transactions*(4): 600-608.

Sawyer, D. T., A. Sobkowiak and J. L. Roberts. 1995. *Electrochemistry for chemists*. New York: Wiley.

Sharpe, A. G. 1992. *Inorganic chemistry*. Burnt Mill, Harlow, Essex, England: Longman Scientific & Technical.

Shaw, W. J., M. L. Helm and D. L. DuBois. 2013. A modular, energy-based approach to the development of nickel containing molecular electrocatalysts for hydrogen production and oxidation. *Biochimica et Biophysica Acta* **1827**(8-9): 1123-1139.

Sheng, Y., I. A. Abreu, D. E. Cabelli, M. J. Maroney, A. F. Miller, M. Teixeira and J. S. Valentine. 2014. Superoxide dismutases and superoxide reductases. *Chemical Reviews* **114**(7): 3854-3918.

Singh, A., S. L. Y. Chang, R. K. Hocking, U. Bach and L. Spiccia. 2013. Highly active nickel oxide water oxidation catalysts deposited from molecular complexes. *Energy & Environmental Science* **6**(2): 579.

Sivasankar, N., W. W. Weare and H. Frei. 2011. Direct observation of a hydroperoxide surface intermediate upon visible light-driven water oxidation at an Ir oxide nanocluster catalyst by rapid-scan FT-IR spectroscopy. *Journal of the American Chemical Society* **133**(33): 12976-12979.

Smil, V. 2004. *Enriching the earth: Fritz haber, carl bosch, and the transformation of world food production*. Cambridge, Massachusetts: MIT Press.

Solomon, E. I., M. J. Baldwin and M. D. Lowery. 1992. Electronic-structures of active-sites in copper proteins: contributions to reactivity. *Chemical Reviews* **92**(4): 521-542.

Speight, J. and N. A. Lange. 2005. *Lange's handbook of chemistry, 70th anniversary edition*. New York: McGraw-Hill Education.

Stoll, S. and A. Schweiger. 2006. Easyspin, a comprehensive software package for spectral simulation and analysis in EPR. *Journal of Magnetic Resonance* **178**(1): 42-55.

Stracke, J. J. and R. G. Finke. 2011. Electrocatalytic water oxidation beginning with the cobalt polyoxometalate $[Co_4(H_2O)_2(PW_9O_{34})_2]^{10-}$: Identification of heterogeneous CoO_x as the dominant catalyst. *Journal of the American Chemical Society* **133**(38): 14872-14875.

Surendranath, Y., M. Dinca and D. G. Nocera. 2009. Electrolyte-dependent electrosynthesis and activity of cobalt-based water oxidation catalysts. *Journal of the American Chemical Society* **131**(7): 2615-2620.

Surendranath, Y., M. W. Kanan and D. G. Nocera. 2010. Mechanistic studies of the oxygen evolution reaction by a cobalt-phosphate catalyst at neutral pH. *Journal of the American Chemical Society* **132**(46): 16501-16509.

Suzuki, K., H. Hiroaki, D. Kohda, H. Nakamura and T. Tanaka. 1998. Metal ion induced self-assembly of a designed peptide into a triple-stranded α-helical bundle: A novel metal binding site in the hydrophobic core. *Journal of the American Chemical Society* **120**(50): 13008-13015.

Tafel, J. 1905. The polarisation of cathodic hydrogen development. *Zeitschrift Fur Physikalische Chemie: Stochiometrie Und Verwandtschaftslehre* **50**(6): 641-712.

Tottey, S., K. J. Waldron, S. J. Firbank, B. Reale, C. Bessant, K. Sato, T. R. Cheek, J. Gray, M. J. Banfield, C. Dennison and N. J. Robinson. 2008. Protein-folding location can regulate manganese-binding versus copper- or zinc-binding. *Nature* **455**(7216): 1138-1142.

Touw, D. S., C. E. Nordman, J. A. Stuckey and V. L. Pecoraro. 2007. Identifying important structural characteristics of arsenic resistance proteins by using designed three-stranded coiled coils. *Proceedings of the National Academy of Sciences of the United States of America* **104**(29): 11969-11974.

Tsuji, E., A. Imanishi, K.-i. Fukui and Y. Nakato. 2011. Electrocatalytic activity of amorphous RuO_2 electrode for oxygen evolution in an aqueous solution. *Electrochimica Acta* **56**(5): 2009-2016.

Umena, Y., K. Kawakami, J.-R. Shen and N. Kamiya. 2011. Crystal structure of oxygen-evolving photosystem II at a resolution of 1.9 Å. *Nature* **473**(7345): 55-60.

Vance, C. K. and A. F. Miller. 1998. A simple proposal that can explain the inactivity of metal-substituted superoxide dismutases. *Journal of the American Chemical Society* **120**(3): 461-467.

Viles, J. H. 2012. Metal ions and amyloid fiber formation in neurodegenerative diseases. Copper, zinc and iron in alzheimer's, parkinson's and prion diseases. *Coordination Chemistry Reviews* **256**(19–20): 2271-2284.

Vinyard, D. J., G. M. Ananyev and G. C. Dismukes. 2013. Photosystem II: The reaction center of oxygenic photosynthesis. *Annual Review of Biochemistry, Vol 82* **82**: 577-606.

Vitousek, P. M. 1994. Beyond global warming: ecology and global change. *Ecology* **75**(7): 1861-1876.

Waldron, K. J., J. C. Rutherford, D. Ford and N. J. Robinson. 2009. Metalloproteins and metal sensing. *Nature* **460**(7257): 823-830.

Walter, M. G., E. L. Warren, J. R. McKone, S. W. Boettcher, Q. Mi, E. A. Santori and N. S. Lewis. 2010. Solar water splitting cells. *Chemical Reviews* **110**(11): 6446-6473.

Wang, S.-S. 1973. P-alkoxybenzyl alcohol resin and p-alkoxybenzyloxycarbonylhydrazide resin for solid phase synthesis of protected peptide fragments. *Journal of the American Chemical Society* **95**(4): 1328-1333.

Wasylenko, D. J., R. D. Palmer and C. P. Berlinguette. 2013. Homogeneous water oxidation catalysts containing a single metal site. *Chemical Communications (Cambridge, England)* **49**(3): 218-227.

Wuerges, J., J. W. Lee, Y. I. Yim, H. S. Yim, S. O. Kang and K. Djinovic Carugo. 2004. Crystal structure of nickel-containing superoxide dismutase reveals another type of active site. *Proceedings of the National Academy of Sciences of the United States of America* **101**(23): 8569-8574.

Wydrzynski, T. J. and K. Satoh. 2005. *Photosystem II: The light-driven water:Plastoquinone oxidoreductase*: Springer.

Yamakura, F. 1978. Study on reconstitution of iron superoxide dismutase from *Pseudomonas ovalis*. *Journal of Biochemistry* **83**(3): 849-857.

Yang, J. T., C. S. C. Wu and H. M. Martinez. 1986. Calculation of protein conformation from circular-dichroism. *Methods in Enzymology* **130**: 208-269.

Yin, Q., J. M. Tan, C. Besson, Y. V. Geletii, D. G. Musaev, A. E. Kuznetsov, Z. Luo, K. I. Hardcastle and C. L. Hill. 2010. A fast soluble carbon-free molecular water oxidation catalyst based on abundant metals. *Science* **328**(5976): 342-345.

Youngblood, M. P. and D. W. Margerum. 1981. Cyclic voltammetric studies of the reduction of copper(ii)-peptide complexes. *Journal of Coordination Chemistry* **11**(2): 103-110.

Youngblood, W. J., S.-H. A. Lee, Y. Kobayashi, E. A. Hernandez-Pagan, P. G. Hoertz, T. A. Moore, A. L. Moore, D. Gust and T. E. Mallouk. 2009. Photoassisted overall water splitting in a visible light-absorbing dye-sensitized photoelectrochemical cell. *Journal of the American Chemical Society* **131**(3): 926-927.

Youngblood, W. J., S. H. Lee, K. Maeda and T. E. Mallouk. 2009. Visible light water splitting using dye-sensitized oxide semiconductors. *Accounts of Chemical Research* **42**(12): 1966-1973.

Yu, F., V. M. Cangelosi, M. L. Zastrow, M. Tegoni, J. S. Plegaria, A. G. Tebo, C. S. Mocny, L. Ruckthong, H. Qayyum and V. L. Pecoraro. 2014. Protein design: Toward functional metalloenzymes. *Chemical Reviews* **114**(7): 3495-3578.

Yu, F., J. E. Penner-Hahn and V. L. Pecoraro. 2013. *De novo*-designed metallopeptides with type 2 copper centers: Modulation of reduction potentials and nitrite reductase activities. *Journal of the American Chemical Society* **135**(48): 18096-18107.

Yu, H. M., S. T. Chen and K. T. Wang. 1992. Enhanced coupling efficiency in solid-phase peptide synthesis by microwave irradiation. *The Journal of Organic Chemistry* **57**(18): 4781-4784.

Zastrow, M. L. and V. L. Pecoraro. 2014. Designing hydrolytic zinc metalloenzymes. *Biochemistry* **53**(6): 957-978.

Zhang, M. T., Z. Chen, P. Kang and T. J. Meyer. 2013. Electrocatalytic water oxidation with a copper(ii) polypeptide complex. *Journal of the American Chemical Society* **135**(6): 2048-2051.

Zhou, F. and G. L. Millhauser. 2012. The rich electrochemistry and redox reactions of the copper sites in the cellular prion protein. *Coordination Chemistry Reviews* **256**(19–20): 2285-2296.

Zong, R. and R. P. Thummel. 2005. A new family of Ru complexes for water oxidation. *Journal of the American Chemical Society* **127**(37): 12802-12803.